

NASA Contractor Report 195390

1N-07
33859
P-216

Three Dimensional Compressible Turbulent Flow Computations for a Diffusing S-Duct With/Without Vortex Generators

Soo-Yong Cho and Isaac Greber
Case Western Reserve University
Cleveland, Ohio

December 1994

Prepared for
Lewis Research Center
Under Cooperative Agreement NCC3-181



National Aeronautics and
Space Administration

(NASA-CR-195390) THREE DIMENSIONAL
COMPRESSIBLE TURBULENT FLOW
COMPUTATIONS FOR A DIFFUSING S-DUCT
WITH/WITHOUT VORTEX GENERATORS
Final Report (Case Western Reserve
Univ.) 216 p

N95-17402

Unclass

G3/07 0033859

**THREE DIMENSIONAL COMPRESSIBLE TURBULENT FLOW COMPUTATIONS
FOR A DIFFUSING S-DUCT WITH/WITHOUT VORTEX GENERATORS**

by

**Soo-Yong Cho and Isaac Greber
Department of Mechanical and Aerospace Engineering
Case Western Reserve University**

**Submitted as NASA Contractor's Report to NASA Lewis
Research Center Grant NCC 3-181**

ABSTRACT

Numerical investigations on a diffusing S-duct with/without vortex generators and a straight duct with vortex generators are presented. The investigation consists of solving the full three-dimensional unsteady compressible mass averaged Navier-Stokes equations. An implicit finite volume lower-upper time marching code (RPLUS3D) has been employed and modified. A three-dimensional Baldwin-Lomax turbulence model has been modified in conjunction with the flow physics.

A model for the analysis of vortex generators in a fully viscous subsonic internal flow is evaluated. A vortical structure for modelling the shed vortex is used as a source term in the computation domain. The injected vortex paths in the straight duct are compared with the analysis by two kinds of prediction models. The flow structure by the vortex generators are investigated along the duct.

Computed results of the flow in a circular diffusing S-duct provide an understanding of the flow structure within a typical engine inlet system. These are compared with the experimental wall static-pressure, static- and total-pressure field, and secondary velocity profiles. Additionally, boundary layer thickness, skin friction values, and velocity profiles in wall coordinates are presented. In order to investigate the effect of vortex generators, various vortex strengths are examined in this study. The total-pressure recovery and distortion coefficients are obtained at the exit of the S-duct. The numerical results clearly depict the interaction between the low velocity flow by the flow separation and the injected vortices.

TABLE OF CONTENTS

	page
ABSTRACT	ii
ACKNOWLEDGEMENTS	iv
TABLE OF CONTENTS	v
LIST OF FIGURES	vii
NOMENCLATURE	xii
CHAPTER 1 : INTRODUCTION AND BACKGROUND	1
1.1 S-duct Without Vortex Generators	1
1.2 S-duct With Vortex Generators	8
CHAPTER 2 : GOVERNING EQUATIONS AND BOUNDARY	
CONDITIONS	17
2.1 Governing Equations	19
2.2 Coordinate Transformation	23
2.3 Boundary Conditions	28
2.4 Turbulence Model	31
2.5 Turbulence Model Implementation	34
CHAPTER 3 : NUMERICAL METHOD	39
3.1 LU Scheme	42
3.2 Artificial Dissipation	48
3.3 Eigenvalues of Jacobian Matrices	50
CHAPTER 4 : DIFFUSING S-DUCT WITHOUT VORTEX GENERATORS	54

4.1 Geometry and Grid	54
4.2 Results and Discussion	56
CHAPTER 5 : STRAIGHT DUCT WITH VORTEX GENERATORS	91
5.1 Vortex Generator Model	93
5.2 Results and Discussion	98
CHAPTER 6 : DIFFUSING S-DUCT WITH VORTEX GENERATORS	133
6.1 Vortex Generator Model	133
6.2 Results and Discussion	135
CHAPTER 7 : CONCLUSION AND RECOMMENDATION	178
REFERENCES	181
APPENDIX A : The Element of Jacobian Matrices	186
APPENDIX B : Vortex Trajectory In a Tube Using the Image Vortex System	188
APPENDIX C : Vortex Trajectory In a Tube Using the Vortex Interaction Model	195

LIST OF FIGURES

Figure	page
1.1 A typical vortex generator.	15
1.2 Typical vortex generator configurations.	16
2.1 Behavior of $F(y) = y \bar{\omega} [(1 - \exp(-y^+/A^*))]$ through the flow field	38
4.1 The geometry of the diffusing S-duct.	69
4.2(a) Axial surface static-pressure coefficient.	70
4.2(b) Axial surface static-pressure coefficient.	71
4.3 Streamwise velocity profiles in the vertical plane of symmetry on the S-duct.	72
4.4 Circumferential surface static-pressure coefficient.	73
4.5 Static-pressure coefficient contours without vortex generators.	74
4.6 Total-pressure coefficient contours without vortex generators.	77
4.7 Total-pressure coefficient contours without vortex generators. At $S/D_i = 5.73$	80
4.8 Axial Mach number contours without vortex generators. At $S/D_i = 5.73$	81
4.9 Secondary velocity profiles without vortex generators.	82
4.10 Secondary velocity profiles without vortex generators. At $S/D_i = 5.73$	85
4.11 Boundary layer thickness.	86

4.12(a) Boundary layer wall coordinates plots at $S/D_i = -1.5$	87
4.12(b) Boundary layer wall coordinates plots at $S/D_i = 2.62$	87
4.12(c) Boundary layer wall coordinates plots at $S/D_i = 5.24$	88
4.12(d) Boundary layer wall coordinates plots at $S/D_i = 5.73$	88
4.13 Skin friction coefficient.	89
4.14 Streamline along the S-duct centerline	90
5.1(a) Computational grid for the vortex interaction studies within a cylindrical duct, $L/D = 20.0$	107
5.1(b) Measurement stations along the circular straight duct.	107
5.2 Total-pressure coefficient contours of the single embedded vortex.	108
5.3 Secondary velocity profiles of the single embedded vortex.	111
5.4(a) Radial trajectory of the single embedded vortex.	114
5.4(b) Angular trajectory of the single embedded vortex.	114
5.5 Total-pressure coefficient contours and secondary velocity profiles of the counter rotating vortices of the same strength that rotate toward each other.	115
5.6(a) Radial trajectory of the counter rotating vortices of the same strength that rotate toward each other.	118
5.6(b) Angular trajectory of the counter rotating vortices of the same strength that rotate toward each other.	118

5.7 Total-pressure coefficient contours and secondary velocity profiles of the counter rotating vortices of the same strength that rotate away from each other.	119
5.8 Static-pressure coefficient contours of the counter rotating vortices of the same strength that rotate away from each other.	122
5.9(a) Radial trajectory of the counter rotating vortices of the same strength that rotate away from each other.	124
5.9(b) Angular trajectory of the counter rotating vortices of the same strength that rotate away from each other.	124
5.10 Total-pressure coefficient contours when the co-rotating vortices are embedded. Vortex(A) has double the strength of vortex (B).	125
5.11 Secondary velocity profiles when the co-rotating vortices are embedded. Vortex(A) has double the strength of vortex (B).	128
5.12(a) Radial trajectory of the vortex(A) which has double the strength of the vortex(B) in the co-rotating vortices.	131
5.12(b) Angular trajectory of the vortex(A) which has double the strength of the vortex(B) in the co-rotating vortices.	131
5.13(a) Radial trajectory of the vortex(B) which has half the strength of the vortex(A) in the co-rotating vortices.	132
5.13(b) Angular trajectory of the vortex(B) which has half the strength of the vortex(A) in the co-rotating vortices.	132
6.1(a) Secondary flow structure from vortex generator model at $S/D_i = 0.17$	145.
6.1(b) Location of injected vortices at $S/D_i = 0.17$	145
6.2(a) Axial surface static-pressure coefficient with $\Gamma/D_i U_\infty = 0.020$	146

6.2(b) Axial surface static-pressure coefficient with $\Gamma/D_i U_\infty = 0.025$	147
6.2(c) Axial surface static-pressure coefficient with $\Gamma/D_i U_\infty = 0.030$	148
6.3(a) Comparison of axial surface static-pressure coefficient with/without vortex generators $\Gamma/D_i U_\infty = 0.005$	149
6.3(b) Comparison of axial surface static-pressure coefficient with/without vortex generators $\Gamma/D_i U_\infty = 0.015$	150
6.3(c) Comparison of axial surface static-pressure coefficient with/without vortex generators $\Gamma/D_i U_\infty = 0.025$	151
6.4 Secondary velocity profiles with vortex generators. $\Gamma/D_i U_\infty = 0.025$	152
6.5 Total-pressure coefficient contours with vortex generators. $\Gamma/D_i U_\infty = 0.025$	154
6.6 Static-pressure coefficient contours with vortex generators. $\Gamma/D_i U_\infty = 0.025$	156
6.7 Boundary layer thickness.	158
6.8 Comparison of the total-pressure coefficient contours with/without vortex generators. $\Gamma/D_i U_\infty = 0.025$	159
6.9 Comparison of the secondary velocity profiles with/without vortex generators. $\Gamma/D_i U_\infty = 0.025$	162
6.10 Comparison of the static-pressure coefficient contours with/without vortex generators. $\Gamma/D_i U_\infty = 0.025$	165
6.11 Total- and static-pressure coefficient contours with vortex generators. $\Gamma/D_i U_\infty = 0.015$	168

6.12 Secondary velocity profiles with vortex generators. $\Gamma/D_1 U_\infty = 0.015$	171
6.13 Total-pressure coefficient contours at the exit of S-duct for variation of vortex strengths.	174
6.14 Effect of vortex strength on the total-pressure recovery at the exit of S-duct	176
6.15 Effect of vortex strength on the distortion coefficient at the exit of S-duct	177
B.1 Location of the image vortex when a single vortex of strength Γ is located inside the circular cylinder.	194
C.1 The secondary flow field generated by vortex i gives rise to a local circumferential component of wall shear stress	199
C.2 Two neighbor vortices in a circular duct for evaluating proximity circulation losses.	200

NOMENCLATURE

\hat{A}	: Jacobians of ξ -direction flux vector
\hat{B}	: Jacobians of η -direction flux vector
\hat{C}	: Jacobians of ζ -direction flux vector
A^+	: Van Driest damping constant
c	: Speed of sound
C_L, C_D	: Lift and drag coefficient
C_p	: Specific heat at constant pressure
C_f	: Wall skin friction coefficient
C_{p0}	: Total-pressure coefficient $(p_{o,local} - p_{ref})/q_{ref}$
C_{p1}	: Surface static-pressure coefficient $(p_{local} - p_{ref})/q_{ref}$
C_{p2}	: Surface static-pressure coefficient $(p_{local} - p_{wall}) / (p_{o,cl} - p_{wall})$
\bar{C}_{p0}	: Total-pressure recovery coefficient $(\int C_{p0} dA) / A$
D	: Spatial finite difference operator
D^+	: Forward difference operator
D^-	: Backward difference operator
D_i, D_e	: Inlet and exit diameter of S-duct
D_o	: Profile drag of vortex generator
$DC(\varphi)$: Distortion coefficient $(\bar{C}_{p\infty} - \bar{C}_{p0}(\varphi))$
e	: Total energy per unit mass

E, \hat{E}	: x, ξ -direction flux
F, \hat{F}	: y, η -direction flux
G, \hat{G}	: z, ζ -direction flux
H_i	: Angular momentum of vortex i
J	: Jacobian of coordinate transformation
k	: Thermal conductivity
M	: Similarity matrix
Ma	: Mach number (U_∞/c)
M_i	: Moment of vortex i
p	: Static-pressure
$P_{o,cl}$: Total-pressure at the center of the duct
$P_{o,local}$: Total-pressure at the local point
P_{ref}	: Static-pressure at the reference point
Pr	: Prandtl number ($c_p\mu/k$)
Pr_t	: Turbulent Prandtl number
q_x, q_y, q_z	: Heat flux in x, y and z -direction
q_{ref}	: Dynamic-pressure at the reference plane
r, θ, x	: Cylindrical coordinates
r_c	: Radius of vortex core
Re_d	: Reynolds number based on the diameter ($\rho D_i u / \mu$)
S	: Distance along the duct centerline
t	: Time
T	: Temperature
T_w	: Wall temperature

u, v, w	: Velocity in cartesian coordinates
u_d	: Streamwise velocity deficit ($U_\infty - u_x$)
u_r, u_θ, u_x	: Velocity in cylindrical coordinates
u_τ	: Friction velocity $(\tau_w/\rho_w)^{(1/2)}$
U	: Dependent variable in cartesian coordinates
\hat{U}	: Dependent variable in generalized coordinates
U_∞	: Free-stream velocity in x-direction
x, y, z	: Cartesian coordinates
y^+	: Normalized distance in wall coordinates (yu_r/ν)
α	: Incident angle of vortex generator
β	: Intersectional angle
γ	: Ratio of specific heat (c_p/c_v)
$\gamma_A, \gamma_B, \gamma_C$: Upper bounds of the eigenvalues of Jacobians
Γ	: Vortex strength
δ	: Boundary layer thickness
Δ	: Difference
$\varepsilon^{(2)}$: Coefficient of second order artificial dissipation
$\varepsilon^{(4)}$: Coefficient of fourth order artificial dissipation
θ	: Arc angle of S-duct
κ	: Von Karman constant (= 0.4)

λ	: Nondimensional radial location of the vortex (r/R)
μ	: Dynamic viscosity or laminar viscosity
μ_t	: Eddy viscosity or turbulent viscosity
ν	: Kinematic viscosity
ξ, η, ζ	: Generalized coordinates
ρ	: Density
$\tau_{xx}, \tau_{yy}, \tau_{zz}$: Normal stress
$\tau_{xy}, \tau_{yz}, \tau_{zx}$: Shear stress
ω	: Angular velocity
$\vec{\omega}$: Vorticity
φ	: Polar angle in S-duct

Subscripts

i, j, k	: Tensor notation
local	: Local value condition
max	: Maximum value condition
o	: Stagnation condition
t	: Turbulent condition
v	: Viscous term
w	: Wall condition
∞	: Free stream condition

CHAPTER 1

INTRODUCTION AND BACKGROUND

1.1 S-duct Without Vortex Generators

The subsonic duct is a feature of the air intake propulsion systems for modern aircraft whether the speed of the aircraft is subsonic or supersonic. Depending on the integration of the engine inlet with the airframe, various shaped ducts are employed. The intention of duct design is to produce high pressure recovery in order to maintain high thrust levels, and low flow distortion consistent with stable engine operation. It is common to design ducts to be as short as possible because of size and weight restrictions. Many aircraft employ curved rectangular, or circular shaped ducts with constant or varying cross-sectional area in the engine intake systems. For example, the Boeing 727, Lockheed Tristar(L-1011), General dynamics F-16, and McDonnell-Douglas F-18, etc., use the S-shaped duct in their engine intake systems. Usually, the diffusing duct is employed in the inlet of the propulsion system of the aircraft in order to decelerate the flow and achieve high pressure recovery at the engine compressor.

The S-shaped duct produces complex cross flow patterns and nonuniform velocity profiles at the exit because of its

curvature and centerline offset. These deteriorate the performance of the engine inlet system. The nonuniform flow at the exit results from the expulsion of low velocity fluid by a pair of counter-rotating vortices, which are produced near the inflection point of the duct and stretched toward the exit.

The experimental results obtained by Bansod and Bradshaw(1972) show the expulsion of low velocity fluid at the exit. The authors conducted experiments using three different kinds of constant-area S-shaped ducts in incompressible flow. The S-shaped ducts were assembled with different radii of curvature(R) of the duct centerline. One had the same $R/D = 2.25$ in the first and second half bend. Others had $R/D = 2.25$ or $R/D = 3.5$ in the first and second half bend, respectively. The S-shaped duct with large radius in the second half bend was more efficient because the thick boundary layer in the second half bend was less rapidly deflected.

McMillan(1982) conducted experiments using a 40° curved rectangular diffusing duct. The flow was incompressible. The results show a pair of counter-rotating vortices at the exit. The secondary velocity profiles show that the high velocity fluid at the central portion of the channel moves toward the concave wall, driven by centrifugal force. Correspondingly, the low velocity fluid

in the boundary layers moves toward the convex wall. The mean velocity in the diffusing duct is dominated by this secondary flow.

Guo and Seddon(1982) tested a S-shaped rectangular duct of constant cross-sectional area with several different angles of attack. The results show that the flow separation, turbulent intensity, and flow distortion at the exit increase with increasing the angle of attack.

Vakili et al.(1987) tested a diffusing 30° - 30° S-duct with circular cross section. The duct area ratio between inlet and exit was 1.51. The offset of the duct resulting from the centerline curvature was 1.34 times the inlet diameter. Two straight circular pipes were attached upstream and downstream of the S-duct to provide the desired boundary layer thickness flow at the inlet of S-duct and minimize the exit flow effect. The entrance Mach number was 0.6 and the Reynolds number based on the inlet diameter was 1.76×10^6 . The secondary velocity profiles, static- and total-pressure contours, and surface static-pressure were measured at the several streamwise locations. The experimental results show that a pair of counter-rotating vortices created by the flow separation cause the flow distortion at the exit of the S-duct.

Jenkins and Loeffler(1991) conducted experiments on a

compact diffusing S-duct. The offset of the duct centerline was 1.5 times inlet diameter. The duct area ratio between inlet and exit was 2.25. The entrance Mach number and Reynolds number were 0.34 and 5.75×10^5 , respectively. The authors measured the secondary velocity profiles, streamwise velocity contours, and surface static-pressure. The results were similar to the experimental results obtained by Vakili et al.(1987).

Wellborn et al.(1992) conducted experiments on a diffusing S-duct, which was larger than, but geometrically similar to the duct studied by Vakili et al.(1987). The duct inlet Mach number was 0.6 and the Reynolds number based on inlet diameter was 2.6×10^6 . Two straight pipes of 3.75 times inlet diameter were attached upstream and downstream of the S-duct to provide a uniform inflow and minimize the exit flow effect. The authors measured the surface static-pressure along the streamwise and circumferential direction. Streamlines near the wall, observed by oil flow visualization, showed the formation of the counter-rotating vortices in the flow separation region. The results showed that the flow at the exit was strongly affected by these vortices, and the mean velocity profiles were very similar to the total-pressure field.

Early numerical work on the curved pipe is shown in

Rowe(1970)'s work. The author computed the secondary flow on a 45° - 45° S-shaped and a 180° pipe by the step by step application of the Squire and Winter's(1951) inviscid secondary flow theory. The computation based on the inviscid theory predicts roughly the flow pattern in a curved pipe, if the mean flow does not have large local variations associated with the secondary flow.

Pratrap and Patankar(1975) calculated mean velocity and secondary flow in a 90° curved constant-area rectangular duct for incompressible flow. The authors used the fully parabolized Navier-Stokes(PNS) equations and partially PNS equations, with a k - ϵ turbulence model. The partially PNS equations for subsonic flow are obtained from the full Navier-Stokes(FNS) equations by assuming that the streamwise viscous diffusion terms are negligible compared to the normal and transverse viscous diffusion terms. The fully PNS equations have one more restriction, that the pressure in the streamwise momentum equation is assumed to vary only in the streamwise direction. More detail information about PNS equations is described by Anderson et al.(1984). The computational results show that predictions using the partially PNS equations are more accurate than those using the fully PNS equations.

Levy et al.(1980) conducted computations in a constant-area S-shaped duct using PNS equations. The offset

and length of the duct was one and five times the inlet diameter, respectively. The inflow Mach number was 0.2. The results show that the total-pressure contours at the region of near the bottom wall are almost the same shape as the streamwise velocity contours. More detailed results of the total-pressure contours and secondary velocity profiles were obtained by Towne and Anderson(1981). The authors also conducted a numerical study with a PNS computer program with an algebraic turbulence model. The flow was laminar with an entrance Mach number of 0.2 and a Reynolds number based on duct diameter of 2000.

Levy et al.(1983) analyzed a 22.5° - 22.5° S-shaped duct in laminar and turbulent flow at Reynolds numbers of 790 and 4.8×10^4 , respectively, using a PNS computer code with an algebraic turbulence model. The streamwise velocity contours agreed well with the experimental data. The analysis shows that the streamwise velocity in turbulent flow is similar to the laminar flow field, but the streamwise velocity distortion in the turbulent flow is less than that in the laminar flow.

Vakili et al.(1983,1984) performed numerical analysis and experiments on a 30° - 30° non-diffusing S-duct. The inlet Mach number was 0.6 and the Reynolds number was 1.76×10^6 . The PNS computer code was used to predict the

static- and total-pressure contours and secondary velocity profiles. The computational results showed that the secondary velocity profiles agreed well with the experimental results. The extent of the flow distortion was underestimated due to simplifications made in the pressure field calculations. The pressure in the streamwise direction was used a sum of the pressure obtained from a three-dimensional potential flow analysis and one-dimensional correction. Harloff et al.(1992a) used the three-dimensional FNS equations to analyze the 30° - 30° nondiffusing S-duct, which had the same geometry and flow conditions tested by Vakili et al.(1984). The authors used two kinds of grid, H- and O-grid. An H-grid conforms well to the rectangular shape. An O-grid, which has a pole boundary condition at the center of the grid, conforms well to a circular cross-section. The results obtained using the O-grid were better than those by H-grid because the H-grid had a large amount of grid skewness in the corner region. The authors concluded that the computational results were in qualitative agreement with the experimental results, and more advanced turbulence model and grid refinement could improve the agreement with the experimental results.

Jenkins and Loeffler(1991) conducted computations on a compact diffusing S-duct, and compared their results with experimental data. Results were obtained using the Baldwin-

Lomax and "one-half" equation turbulence model which accounts for some of the history effects in computing the turbulence length scale. The results showed that the thin layer Navier-Stokes equations code provided a reasonably good representation of the flow at the exit, but the code could not accurately predict the separated flow region.

Harloff et al.(1992b) conducted a numerical study in the diffusing 30°-30° S-duct using the three-dimensional FNS equations. The authors used the algebraic and k- ϵ turbulence model. The wall static-pressure distribution and total-pressure profiles calculated with the k- ϵ turbulence model were better than those with the algebraic turbulence model. However, the computational results showed that both turbulence models could not adequately account for strong secondary flows with flow separation.

1.2 S-duct With Vortex Generators

From the review of the S-shaped duct without vortex generators, one sees that the strong secondary flow due to adverse pressure gradient may have deteriorating effects on the performance of the engine inlet system. To alleviate this problem, a vortex generator can be used as a flow control device because it can transport energy into the boundary layer from the outer flow. The vortex generator

has been used mainly for the prevention of separation on wings, diffusers, or bends, or at least for decreasing the extent of separated region. There are many kinds of vortex generators, such as simple plow, shielded plow, triangular plow, scoop, twist interchanger, ramp, tapered fin, dome, shielded sink, etc.,. Schubauer and Spangenberg(1960) experimentally investigated the mixing rate of the turbulent boundary layers with many different vortex generators in a region of adverse pressure gradient. Most vortex generators in use today are small wing sections, which are mounted upstream of the problem flow area. The vortex generators are inclined to the oncoming flow to generate shed vortices. The vortex generators are usually sized to local boundary layer height to obtain the best interaction between the shed vortex and the boundary layer. The vortex generators are usually placed in groups of two or more upstream of the problem flow area. Fig. 1.1 shows a wing type vortex generator.

Boundary layer control by vortex generators relies on induced mixing between the external or core stream and the low energy flow region. The mixing is promoted by longitudinally trailing vortices over the duct surface adjacent to the edge of the boundary layer. Fluid particles with high momentum in the streamwise direction are swept along helical paths toward the duct surface to mix with

and, to some extent, replace the low momentum boundary layer flow. This is a continuous process that provides a source of re-energization to counter the natural boundary layer growth caused by surface friction, adverse pressure gradients, and low energy secondary flow accumulation.

There are two basic configurations. In one configuration, all of the vortex generators are inclined at the same angle with respect to the oncoming flow direction, as shown in Fig. 1.2(a). These are called co-rotating configurations because the shed vortices rotate in the same direction. In the other configuration, the vortex generators are grouped in pairs inclined in the opposite direction to the oncoming flow, as shown in Fig 1.2(b). These are termed the counter-rotating configurations because the shed vortices in pairs rotate in opposite directions to each other.

What kind of configuration is chosen depends on the location of the flow separation for a given geometry. Co-rotating vortex generators are very competitive with counter-rotating vortices in reducing the flow separation if the generators are properly selected and located. This type of vortex generator has the following characteristics when it is used within the duct. (1) Two induced vortices move along the duct surface, (2) the first vortex moves away from the duct surface, (3) the other vortex remains

close to the duct surface, and (4) the distance between them decreases because they counteract each other.

Counter-rotating vortex generators are very effective in reducing the flow separation if the vortex generators are placed slightly upstream of the region of separation. If the induced vortices are rotating away from each other, the induced secondary flow between two vortex generators moves toward the center of the duct. The vortices are attracted to each other for a short time, and then they proceed to march away from the wall. Since the two vortices are moving toward the center of the duct, the duct surface is not much affected by the induced vortices. If the induced vortices are rotating toward each other, the induced secondary flow between two vortex generators moves toward the duct surface. Two vortices move away from each other, but they remain close to the duct surface because the induced secondary velocities push each other toward the surface. The induced vortex strength is dissipated significantly as it moves downstream due to viscous diffusion.

Early studies with vortex generators have focused on improving the diffuser performance. Brown et al.(1968) conducted experiments with pairs of vane type vortex generators in a short diffuser. The results show that high pressure recovery and flow uniformity can be achieved by

the vortex generators, but the incorrect arrangement of vortex generators can lead to significance performance losses.

Vakili et al.(1986) experimentally investigated the performance of the vortex generators in a diffusing 30° - 30° S-shaped duct with circular cross-section. The entrance Mach number was 0.6 and the Reynolds number based on the diameter was 1.76×10^6 . To eliminate the total-pressure distortion at the exit and flow separation in the duct, arc wing type, rail type and vane type vortex generators were installed at the upstream of the separation region. Using a flow control device, the flow distortion at the exit was significantly improved. The results showed that the flow field at the exit depended on the types of vortex generators.

Reichert and Wendt(1992) conducted experiments to examine three parameters of vortex generators array, i.e., the height of vortex generator, the location of the vortex generators array, and the vortex generators spacing. The test was performed on the same geometry and flow conditions as studied by Wellborn et al.(1992). The Wheeler wishbone generators, which produced a pair of counter-rotating vortices, were used. The results show that the efficiency of vortex generators is much dependent on the parameters of

vortex generators.

A numerical study of a fully viscous subsonic internal flow with vortex generators was reported by Kunik(1986). The shed vortex is modeled by introducing a vorticity source term into a modified form of the PNS equations. That vortex model resembles the one proposed by Squire(1965) except that it neglects the variation of viscosity in the cross plane. Quantitative comparisons with the experimental data by Vakili et al.(1986) show that the vortex model can predict the global flow field in the S-duct.

Anderson(1991) conducted the analysis of the flow physics associated with vortex injection in the S-shaped duct and F/A-18 inlet duct. The author used the PNS equations with the algebraic turbulence model. Predicted total-pressure profiles were in good agreement with experiment results, but the transverse velocities at the exit were overestimated.

The PNS equations were derived from the FNS equations using a series expansion technique. These equations can be solved using a space-marching technique because the streamwise diffusion term in the FNS equations is neglected and a pressure in the streamwise momentum equation is assumed to vary only in the streamwise direction for subsonic flow. Naturally, a substantial reduction in computation time and storage is achieved, but the space

marching method is not well posed if the streamwise pressure gradient is included everywhere in the flow field. If the streamwise velocity deficit in the vortex core is quickly recovered along the duct, the role of the streamwise diffusion term in the FNS equations is important. In that case, the FNS equations should be solved.

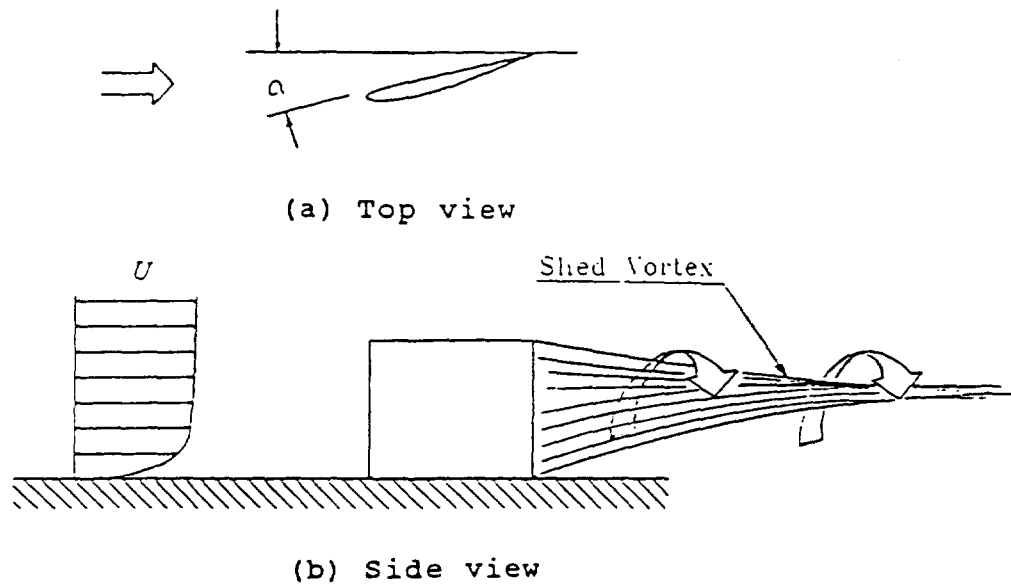
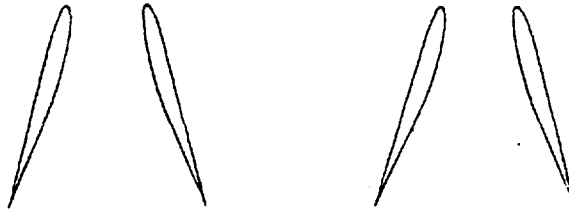


Fig. 1.1 A typical vortex generator.



(a) Co-rotating.



(b) Counter-rotating.

Fig. 1.2 Typical vortex generator configurations.

CHAPTER 2

GOVERNING EQUATIONS AND BOUNDARY CONDITIONS

From the reviews of the S-duct without vortex generators, we can conclude that computational fluid dynamics(CFD) studies have generally used the PNS computer code to predict the flow fields in the curved ducts, and simple turbulence modelling without modifications cannot predict correctly the flow fields which have strong secondary flows with flow separation. The PNS solutions usually rely on an input inviscid static-pressure field, which is generally from an Euler or potential analysis. In the present study, the three-dimensional FNS equations with a modified algebraic turbulence model are solved to predict the flow fields in the diffusing 30° - 30° S-duct. The inlet Mach number is 0.6 and the Reynolds number based on the inlet diameter is 1.76×10^6 . Several aspects of the flow fields are examined. The computed static- and total-pressure fields, secondary velocity profiles and boundary thickness are compared with experimental results obtained by Vakili et al.(1986,1987) and Wellborn et al.(1992) for CFD validation. Additionally, skin friction values and velocity profiles in wall coordinates are investigated.

From the reviews of the S-duct with vortex generators,

we know that most of predictions of flow fields with vortex generators are conducted using PNS equations. In order to apply space-marching method of PNS equations, the vortical structures, modelled from the shed vortex, are set up at the inlet plane of a computational domain with the approximately calculated inlet flow conditions. In contrast to the previously published work, a new vortex model is developed and it is applied inside the computational domain like a source term. The inlet boundary conditions are not affected by the added vortical structures. Numerical analysis is conducted using the three-dimensional FNS equations, with an algebraic turbulence model, because FNS equations are able to deal with the streamwise diffusion terms, which are important in the region of the shed vortex core. In order to confirm the developed vortex model, four-different types of vortex generators are examined in a straight duct. In the straight duct computations, the inlet Mach number is 0.6 and the Reynolds number based on the diameter is 1.0×10^6 . The computational results are compared with the analytic results obtained by the two prediction models.

In order to investigate the flow structure in the diffusing 30° - 30° S-duct with vortex generators, the above mentioned vortex model is applied inside the computational

domain. The three-dimensional FNS equations with a modified algebraic turbulence model are solved. The inlet Mach number is 0.6 and the Reynolds number based on the inlet diameter is 1.76×10^6 . The interaction between the injected vortices and separated flow is investigated. The static- and total-pressure fields and secondary velocity profiles are compared with the experimental results obtained by Vakili et al. (1986). In order to investigate the effects of the injected vortices, the computed results are compared with those without vortex generators, and the total-pressure recovery and distortion coefficients are investigated at the exit of S-duct.

2.1 Governing Equations

The three-dimensional and compressible Navier-Stokes equations in Cartesian coordinates without body forces are written in a conservation form as follows:

$$\frac{\partial U}{\partial t} + \frac{\partial (E - E_v)}{\partial x} + \frac{\partial (F - F_v)}{\partial y} + \frac{\partial (G - G_v)}{\partial z} = 0 \quad (2.1)$$

U is the independent variable, E , F and G are the convective flux vectors

$$U = \begin{pmatrix} \rho \\ \rho u \\ \rho v \\ \rho w \\ \rho e \end{pmatrix} \quad (2.2)$$

$$E = \begin{pmatrix} \rho u \\ \rho u^2 + p \\ \rho uv \\ \rho uw \\ u(\rho e + p) \end{pmatrix} \quad (2.3)$$

$$F = \begin{pmatrix} \rho v \\ \rho uv \\ \rho v^2 + p \\ \rho vw \\ v(\rho e + p) \end{pmatrix} \quad (2.4)$$

$$G = \begin{pmatrix} \rho w \\ \rho uw \\ \rho vw \\ \rho w^2 + p \\ w(\rho e + p) \end{pmatrix} \quad (2.5)$$

E_v , F_v , and G_v are the viscous flux vectors:

$$E_v = \begin{pmatrix} 0 \\ \tau_{xx} \\ \tau_{xy} \\ \tau_{xz} \\ U\tau_{xx} + V\tau_{xy} + W\tau_{xz} - Q_x \end{pmatrix} \quad (2.6)$$

$$F_v = \begin{pmatrix} 0 \\ \tau_{yx} \\ \tau_{yy} \\ \tau_{yz} \\ U\tau_{yx} + V\tau_{yy} + W\tau_{yz} - Q_y \end{pmatrix} \quad (2.7)$$

$$G_v = \begin{pmatrix} 0 \\ \tau_{zx} \\ \tau_{zy} \\ \tau_{zz} \\ U\tau_{zx} + V\tau_{zy} + W\tau_{zz} - Q_z \end{pmatrix} \quad (2.8)$$

The first row of the vector Eq. (2.1) corresponds to the continuity equation, the second, third and fourth rows are the momentum equations, the fifth row is the energy equation; e in the energy equation is the summation of internal energy and kinetic energy per unit mass. The shear and normal stresses can be expressed using Stokes hypothesis, i.e., the second viscous factor $\lambda = -2\mu/3$

$$\tau_{xx} = 2\mu \frac{\partial u}{\partial x} - \frac{2}{3}\mu \left(\frac{\partial u}{\partial x} + \frac{\partial v}{\partial y} + \frac{\partial w}{\partial z} \right)$$

$$\tau_{yy} = 2\mu \frac{\partial v}{\partial y} - \frac{2}{3}\mu \left(\frac{\partial u}{\partial x} + \frac{\partial v}{\partial y} + \frac{\partial w}{\partial z} \right)$$

$$\tau_{zz} = 2\mu \frac{\partial w}{\partial z} - \frac{2}{3}\mu \left(\frac{\partial u}{\partial x} + \frac{\partial v}{\partial y} + \frac{\partial w}{\partial z} \right)$$

$$\tau_{zx} = \tau_{xz} = \mu \left(\frac{\partial u}{\partial z} + \frac{\partial w}{\partial x} \right) \quad (2.9)$$

$$\tau_{yz} = \tau_{zy} = \mu \left(\frac{\partial v}{\partial z} + \frac{\partial w}{\partial y} \right)$$

$$\tau_{xy} = \tau_{yx} = \mu \left(\frac{\partial u}{\partial y} + \frac{\partial v}{\partial x} \right)$$

In the energy equation, heat flux q_x , q_y and q_z are expressed as;

$$q_x = -k \frac{\partial T}{\partial x}$$

$$q_y = -k \frac{\partial T}{\partial y} \quad (2.10)$$

$$q_z = -k \frac{\partial T}{\partial z}$$

To close this system, the state equation with an assumption of a perfect gas is employed.

$$p = \rho R T \quad (2.11)$$

The viscosity, heat conductivity coefficients and

specific heats of air are evaluated using fifth order polynomials in temperature, using properties presented in the National Bureau of Standards tables(1955).

For turbulent flow, it is convenient to use a conservation form of the mass-averaged Navier-Stokes equation. This form takes all turbulence effects into account by adding the eddy viscosity to the equations. These equations can be obtained by replacing the molecular coefficient of viscosity μ with $\mu + \mu_t$ and also the coefficient of thermal conductivity k with $k + k_t$. μ_t is the eddy viscosity and k_t is the turbulent thermal conductivity. The turbulent thermal conductivity can be expressed in terms of the eddy viscosity and turbulent Prandtl number Pr_t , i.e., $k_t = c_p \mu_t / Pr_t$. In the present study, the turbulent Prandtl number is assigned $Pr_t = 0.9$ for air, and the eddy viscosity will be discussed in the section on turbulence model.

2.2 Coordinate Transformation

The computation of flow-fields in and around complex shapes such as ducts, engine intakes or aircraft, etc., involves computational boundaries that do not coincide with

coordinate lines in physical space. For numerical methods, the imposition of boundary conditions for such problems has required a complicated interpolation of the data on local grid lines, and typically a local loss of accuracy in the computational solution. Such difficulties motivate the introduction of a mapping or transformation from physical (x, y, z) space to a generalized curvilinear coordinates (ξ, η, ζ) space. The generalized coordinate domain is constructed so that a computational boundary in physical space coincides with a coordinate line in generalized coordinate space. It makes it possible to solve the governing equations on an uniformly spaced computational grid. In order to use an uniform grid, consider a general transformation of the governing equations.

$$\xi = \xi (x, y, z)$$

$$\eta = \eta (x, y, z) \tag{2.12}$$

$$\zeta = \zeta (x, y, z)$$

Using the chain rule of partial differentiation, the partial derivatives become

$$\begin{aligned}
\frac{\partial}{\partial x} &= \xi_x \frac{\partial}{\partial \xi} + \eta_x \frac{\partial}{\partial \eta} + \zeta_x \frac{\partial}{\partial \zeta} \\
\frac{\partial}{\partial y} &= \xi_y \frac{\partial}{\partial \xi} + \eta_y \frac{\partial}{\partial \eta} + \zeta_y \frac{\partial}{\partial \zeta} \\
\frac{\partial}{\partial z} &= \xi_z \frac{\partial}{\partial \xi} + \eta_z \frac{\partial}{\partial \eta} + \zeta_z \frac{\partial}{\partial \zeta}
\end{aligned} \tag{2.13}$$

The Jacobians of the coordinate transformation are as follows:

$$J = \det \begin{pmatrix} x_\xi & x_\eta & x_\zeta \\ y_\xi & y_\eta & y_\zeta \\ z_\xi & z_\eta & z_\zeta \end{pmatrix} \tag{2.14}$$

The vector Eq. (2.1) can be written in terms of a generalized nonorthogonal curvilinear system (ξ, η, ζ) using the change rule of partial differentiation and the Jacobian of the transformation. The resulting equations can be written:

$$\frac{\partial \hat{U}}{\partial t} + \frac{\partial (\hat{E} - \hat{E}_v)}{\partial \xi} + \frac{\partial (\hat{F} - \hat{F}_v)}{\partial \eta} + \frac{\partial (\hat{G} - \hat{G}_v)}{\partial \zeta} = 0 \tag{2.15}$$

$$\hat{\sigma} = \begin{pmatrix} \rho J \\ \rho Ju \\ \rho Jv \\ \rho Jw \\ \rho Je \end{pmatrix} \quad (2.16)$$

$$\hat{E} = \begin{pmatrix} \rho J (u\xi_x + v\xi_y + w\xi_z) \\ \rho Ju (u\xi_x + v\xi_y + w\xi_z) + pJ\xi_x \\ \rho Jv (u\xi_x + v\xi_y + w\xi_z) + pJ\xi_y \\ \rho Jw (u\xi_x + v\xi_y + w\xi_z) + pJ\xi_z \\ (\rho e + p) J (u\xi_x + v\xi_y + w\xi_z) \end{pmatrix} \quad (2.17)$$

$$\hat{F} = \begin{pmatrix} \rho J (u\eta_x + v\eta_y + w\eta_z) \\ \rho Ju (u\eta_x + v\eta_y + w\eta_z) + pJ\eta_x \\ \rho Jv (u\eta_x + v\eta_y + w\eta_z) + pJ\eta_y \\ \rho Jw (u\eta_x + v\eta_y + w\eta_z) + pJ\eta_z \\ (\rho e + p) J (u\eta_x + v\eta_y + w\eta_z) \end{pmatrix} \quad (2.18)$$

$$\hat{G} = \begin{pmatrix} \rho J (u\zeta_x + v\zeta_y + w\zeta_z) \\ \rho Ju (u\zeta_x + v\zeta_y + w\zeta_z) + pJ\zeta_x \\ \rho Jv (u\zeta_x + v\zeta_y + w\zeta_z) + pJ\zeta_y \\ \rho Jw (u\zeta_x + v\zeta_y + w\zeta_z) + pJ\zeta_z \\ (\rho e + p) J (u\zeta_x + v\zeta_y + w\zeta_z) \end{pmatrix} \quad (2.19)$$

$$\hat{E}_v = \begin{pmatrix} e_{v1} \\ e_{v2} \\ e_{v3} \\ e_{v4} \\ e_{v5} \end{pmatrix} = \begin{pmatrix} 0 \\ \tau_{xx}J\xi_x + \tau_{xy}J\xi_y + \tau_{xz}J\xi_z \\ \tau_{xy}J\xi_x + \tau_{yy}J\xi_y + \tau_{yz}J\xi_z \\ \tau_{xz}J\xi_x + \tau_{yz}J\xi_y + \tau_{zz}J\xi_z \\ ue_{v2} + ve_{v3} + we_{v4} + \frac{C_p\mu}{Pr} \left(c_1 \frac{\partial T}{\partial \xi} + c_2 \frac{\partial T}{\partial \eta} + c_3 \frac{\partial T}{\partial \zeta} \right) \end{pmatrix} \quad (2.20)$$

$$\hat{F}_v = \begin{pmatrix} f_{v1} \\ f_{v2} \\ f_{v3} \\ f_{v4} \\ f_{v5} \end{pmatrix} = \begin{pmatrix} 0 \\ \tau_{xx}J\eta_x + \tau_{xy}J\eta_y + \tau_{xz}J\eta_z \\ \tau_{xy}J\eta_x + \tau_{yy}J\eta_y + \tau_{yz}J\eta_z \\ \tau_{xz}J\eta_x + \tau_{yz}J\eta_y + \tau_{zz}J\eta_z \\ uf_{v2} + vf_{v3} + wf_{v4} + \frac{C_p\mu}{Pr} \left(c_2 \frac{\partial T}{\partial \xi} + c_4 \frac{\partial T}{\partial \eta} + c_5 \frac{\partial T}{\partial \zeta} \right) \end{pmatrix} \quad (2.21)$$

$$\hat{G}_v = \begin{pmatrix} g_{v1} \\ g_{v2} \\ g_{v3} \\ g_{v4} \\ g_{v5} \end{pmatrix} = \begin{pmatrix} 0 \\ \tau_{xx}J\zeta_x + \tau_{xy}J\zeta_y + \tau_{xz}J\zeta_z \\ \tau_{xy}J\zeta_x + \tau_{yy}J\zeta_y + \tau_{yz}J\zeta_z \\ \tau_{xz}J\zeta_x + \tau_{yz}J\zeta_y + \tau_{zz}J\zeta_z \\ ug_{v2} + vg_{v3} + wg_{v4} + \frac{C_p\mu}{Pr} \left(c_3 \frac{\partial T}{\partial \xi} + c_5 \frac{\partial T}{\partial \eta} + c_6 \frac{\partial T}{\partial \zeta} \right) \end{pmatrix} \quad (2.22)$$

where

$$\begin{aligned} c_1 &= J(\xi_x^2 + \xi_y^2 + \xi_z^2) \\ c_2 &= J(\xi_x\eta_x + \xi_y\eta_y + \xi_z\eta_z) \\ c_3 &= J(\xi_x\zeta_x + \xi_y\zeta_y + \xi_z\zeta_z) \\ c_4 &= J(\eta_x^2 + \eta_y^2 + \eta_z^2) \end{aligned} \quad (2.23)$$

$$C_5 = J (\eta_x \zeta_x + \eta_y \zeta_y + \eta_z \zeta_z)$$

$$C_6 = J (\zeta_x^2 + \zeta_y^2 + \zeta_z^2)$$

Note that all the stress terms in \hat{E}_v , \hat{F}_v and \hat{G}_v should be transformed. For example, the shear stress term τ_{xy} would be transformed to;

$$\tau_{xy} = \mu \left(\xi_y \frac{\partial u}{\partial \xi} + \eta_y \frac{\partial u}{\partial \eta} + \zeta_y \frac{\partial u}{\partial \zeta} + \xi_x \frac{\partial v}{\partial \xi} + \eta_x \frac{\partial v}{\partial \eta} + \zeta_x \frac{\partial v}{\partial \zeta} \right) \quad (2.24)$$

2.3 Boundary Conditions

The numerical solution of any partial differential equation requires the application of appropriate number of properly posed boundary conditions. The important aspects of boundary condition development are that the physical definition of the flow problem must be satisfied and the numerical algorithm with the developed boundary conditions must be stable. The theory of characteristics suggests how to decide the conditions required at a boundary. The concept of characteristic theory is most easily developed for the one-dimensional Euler equations. Extending the concepts to three-dimensions, we can obtain three U_∞ , $U_\infty + c$ and $U_\infty - c$ characteristics in this system, using the fact

that the incoming flow at the inlet plane is uniform. At the inlet plane, only four pieces of information enter the domain along the incoming characteristics and one piece leaves along the outgoing characteristics because the flow speed in the whole computational domain is subsonic. Therefore, four boundary conditions must be specified, and one relation has to be extracted from the characteristic equation.

It is not necessary to fix values in terms of the actual characteristic variables as long as the alternative choice leads to a well posed problem. A particular good choice on physical grounds is to specify the stagnation enthalpy and the entropy of the incoming flow. For a perfect gas, this corresponds to specifying the stagnation temperature and pressure. These conditions are same as the flow conditions through a duct or nozzle fed from a large reservoir in which conditions remain constant. Constant stagnation temperature T_o and pressure p_o are specified at the inlet plane.

$$T_o = T + \frac{u^2}{2 c_p} \quad (2.25)$$

$$p_o = p \left(\frac{T}{T_o} \right)^{\frac{\gamma}{\gamma-1}} \quad (2.26)$$

The transverse velocities are assumed to be zero. The relation which corresponds to the negative characteristic can be derived along the characteristics Eq. (2.27).

$$\frac{dp}{d\xi_-} - \rho c \frac{du}{d\xi_-} = 0 \quad (2.27)$$

This becomes

$$p - \rho c u = (p - \rho c u)_{interior} \quad (2.28)$$

Substituting the inflow boundary condition Eqs. (2.25) and (2.28) into Eq. (2.26), we can obtain the inlet temperature, static-pressure and axial velocity. The axial velocity near the duct edge approaches zero in order to satisfy the no-slip condition on the wall during iterations because the finite volume method is employed. The density at the inlet is calculated from the equation of state. The total initial energy at the entry plane can be obtained from the calculated values.

At the exit, one negative characteristic enters through the boundary into the computational domain. One boundary condition must be specified at this plane. In this study, constant static-pressure is specified at the exit plane. Physically this condition corresponds to a duct with an unobstructed exit into a large constant pressure reservoir. Linear extrapolation is adopted for evaluating the exit velocity and exit density. The exit

temperature is calculated from the equation of state. The total internal energy at the exit plane can be obtained from the calculated values.

The no-slip condition is specified on the wall of the duct and an adiabatic wall condition is imposed by setting the normal derivative of temperature equal to zero. The boundary values at the center, which is needed when using the O-grid, are evaluated by averaging the surrounding flow properties.

2.4 Turbulence Model

The Baldwin-Lomax turbulence model(1978) is applied along the normal direction from the wall. This model has been used extensively for attached or slightly separated flows because it leads to low computational time requirements and it appears to be comparable to more complex turbulence models. The Baldwin-Lomax model is an algebraic two-layer eddy viscosity model based on the Cebeci-Smith(1974) method with modifications that avoid the necessity for finding the edge of the boundary layer. Near the wall, the Baldwin-Lomax model uses the well-known Prandtl-Van Driest formulation for the turbulent viscosity.

$$(\mu_t)_{inner} = \rho l^2 |\bar{\omega}| \quad (2.29)$$

where

$$l = \kappa y \left[1 - \exp \left(-\frac{y^+}{A^+} \right) \right] \quad (2.30)$$

$|\bar{\omega}|$ is the magnitude of the local vorticity vector.

$$|\bar{\omega}| = \sqrt{\left(\frac{\partial u}{\partial y} - \frac{\partial v}{\partial x} \right)^2 + \left(\frac{\partial v}{\partial z} - \frac{\partial w}{\partial y} \right)^2 + \left(\frac{\partial w}{\partial x} - \frac{\partial u}{\partial z} \right)^2} \quad (2.31)$$

and

$$y^+ = \frac{\rho_w u_\tau y}{\mu_w} = \frac{\sqrt{\rho_w \tau_w} y}{\mu_w} \quad (2.32)$$

Since the damping constant A^+ is a function of the pressure gradient, an empirical equation by Kays and Crawford(1980) is employed for A^+ .

$$A^+ = \frac{25.0}{7.1 b p^+ + 1.0} \quad (2.33)$$

$$\text{If } p^+ > 0.0, \quad b = 2.9$$

$$\text{If } p^+ < 0.0, \quad b = 4.25$$

where

$$p^+ = \frac{\mu \left(\frac{\partial p}{\partial x} \right)}{\rho^{(1/2)} \tau_w^{(3/2)}} \quad (2.34)$$

In this study, τ_w is evaluated as the absolute value; the value of p^+ in the computation is less than $O(10^2)$.

In the outer region, a Clauser formulation with a Klebanoff intermittency function is used.

$$(\mu)_{outer} = 0.02688 \rho F_{wake} F_{kleb}(y) \quad (2.35)$$

where

$$F_{wake} = \min(y_{max} F_{max}, 0.25 y_{max} q_{dif}^2 / F_{max}) \quad (2.36)$$

and Klebanoff intermittency factor is given by

$$F_{kleb}(y) = [1 + 5.5 (0.3 \frac{y}{y_{max}})^6]^{-1} \quad (2.37)$$

where y_{max} and F_{max} are determined from the equation

$$F(y) = y |\bar{\omega}| [1 - \exp(-\frac{y^*}{A^*})] \quad (2.38)$$

The quantity q_{dif} is the difference between the maximum and minimum total velocity in the profile. The parameter F_{max} is the maximum value of $F(y)$ that occurs in a profile, and y_{max} is the value of y at which it occurs. The length y is the normal distance from the wall and y_c is the smallest value of y at which values from the inner and outer formula are equal.

$$\mu_t = \begin{cases} (\mu_t)_{inner} & y \leq y_c \\ (\mu_t)_{outer} & y > y_c \end{cases} \quad (2.39)$$

The turbulent Prandtl number is assumed to be $Pr_t = 0.9$ in the present study.

2.5 Turbulence Model Implementation

Eddy viscosity turbulence models are usually derived and validated for two-dimensional boundary layer flows. Further, the eddy viscosity coefficient determined by these models depends on the local flow profiles along the normal direction from the wall. The Baldwin-Lomax turbulence model performs adequately for fully attached or mildly separated flows over simple geometry. However, for the flows over more complex configurations, where the boundary layers and wakes may interact or flow separation may occur, the major difficulty encountered in applying the Baldwin-Lomax turbulence model is that of properly evaluating the scale length y_{max} and in turn, of determining $(\mu_t)_{outer}$ for boundary layer profiles.

The turbulence length scales are determined by l of Eq. (2.30) in the inner layer, and y_{max} in the outer layer. The eddy viscosity in the outer layer depends on the F_{wake} and the Klebanoff intermittency factor. F_{wake} is a function

of y_{max} and F_{max} . F_{Kleb} is a function of (y/y_{max}) . The y_{max} is the distance at which the maximum value of $F(y)$ occurs along the normal direction from the wall, where $F(y)$ is proportional to the moment of vorticity. For simple turbulence flows, a single well defined peak exists in the function $F(y)$ along a given streamwise station. When the flows are complex, the function $F(y)$ may exhibit multiple local maxima. Selection of inappropriate length scales leads to inaccurate flow structure. Various methods for determining the appropriate length scale have been proposed.

Horstman(1987) modified the Baldwin-Lomax turbulence model for the problem of shock-wave and turbulent boundary layer interaction flows. The y_{max} occurred outside the boundary layer thickness upstream and downstream of the shock induced separated region. The first maximum value of $F(y)$ away from the wall was used to insure y_{max} is less than the boundary layer thickness.

Degani et al.(1986, 1991) proposed modification of the Baldwin-Lomax turbulence model in computing the three-dimensional separated flow around a prolate spheroid at high incidence in the supersonic and subsonic flow. To eliminate the selection of large F_{max} due to the presence of the vortex sheet, it was chosen at the first peak value of

$F(y)$ from the wall. In case of showing a nonsmooth behavior in $F(y)$, a maximum value of $F(y)$ was chosen at the 90% of the local maximum value. Another modification was that a cut-off distance was specified in terms of y_{max} from the previous ray. If no peak of $F(y)$ is found in that range, the value of F_{max} and y_{max} were taken as those found on the previous rays.

As mentioned in introduction, the three-dimensional flow separation occurs in the S-duct by the pressure force due to the duct geometry change rather than by shear force. The vortical structure, which results from the flow separation, is stretched to the second half of the duct by the streamwise velocity. It causes y_{max} to be located outside the boundary layer thickness as shown in Fig. 2.1(b); therefore, it is not necessary to consider the whole normal direction from the wall to pick the correct y_{max} .

In this study, in order to avoid choosing an inappropriate length scale(y_{max}), the cut-off distances are evaluated in every crossplane. They are obtained by averaging the local boundary layer thicknesses within $\varphi = 45^\circ$. The effect of strong secondary flow due to flow separation can be neglected in this region. The length scale search is restricted to within the cut-off distance. If the local boundary layer thickness is less than 110% of

the cut-off distance, F_{max} and y_{max} are chosen at the maximum peak point within that distance. Otherwise, the first peak value of $F(y)$ from the wall is chosen as F_{max} .

If one employs the same method to decide a cut-off distance in the case of the flow with vortex generators, the cut-off distance is less than that of the flow without vortex generators. This is because the local boundary layer thickness within $\varphi = 45^\circ$ is thinner than with without vortex generators because the shed vortex from the vortex generator has a streamwise velocity deficit at the region of the vortex core. The cut-off distance of the flow with vortex generators is adjusted to be greater than the average boundary layer thickness which is obtained by averaging the local boundary layer thicknesses within $\varphi = 45^\circ$.

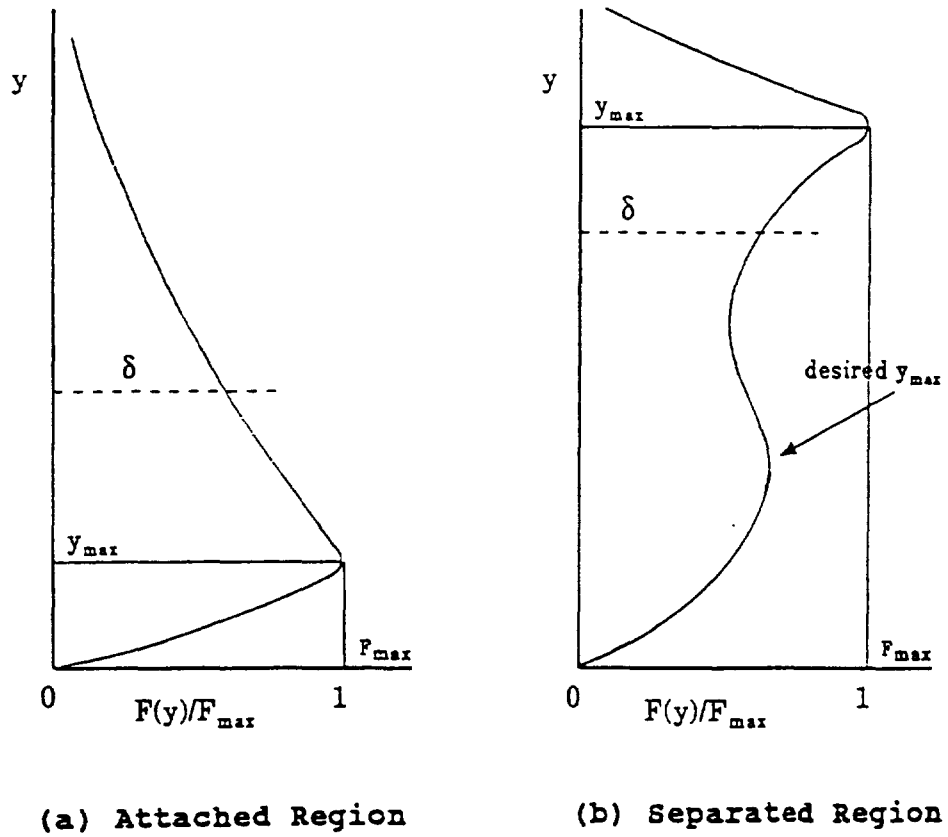


Fig. 2.1 Behavior of $F(y) = y|\bar{\omega}|[(1 - \exp(-y^+/A^+))]$ through the flow field

CHAPTER 3

NUMERICAL METHOD

The unsteady compressible Navier-Stokes equations are a mixed set of parabolic-hyperbolic equations. If the unsteady terms are dropped from these equations, the resulting equations become a mixed set of elliptic-hyperbolic equations. These equations are more difficult to solve than the unsteady compressible Navier-Stokes equations. Most compressible Navier-Stokes equation solutions are obtained using the unsteady term; the steady-state solutions are obtained by time marching until sufficient convergence is achieved.

Both explicit and implicit schemes have been used to solve the compressible Navier-Stokes equations. MacCormack(1969) solved the compressible Navier-Stokes equations using an explicit scheme with a predictor-corrector technique. He used forward differences for all spatial derivatives in the predictor step while backward differences was used in the corrector step. Although the explicit schemes have an advantage that they are easy to implement, these schemes need long computation time because of the limitation on the time step due to the Courant-Friedrichs-Lewy(CFL) stability restriction. For this

reason, schemes with less-restrictive stability conditions have been an important subject of investigation. Allen and Cheng(1970) introduced a nonconsistent approximation scheme $[f_{,xx}^n = (f_{i+1}^n - 2f_i^{n+1} + f_{i-1}^n)/\Delta x^2]$. This approximation scheme becomes consistent when the steady state is reached and it has good stability properties when the mesh Reynolds number is less than 2. MacCormack(1971) modified his original scheme by splitting a sequence of one-dimensional operations. The stability condition on the revised scheme is less restrictive than his original scheme. Deiwert(1975) employed a finite volume method to solve compressible Navier-Stokes equations with less-restrictive stability condition. However, the explicit schemes are not a suitable method for solving high Reynolds number flows where the viscous regions become very thin. For these flows, a very fine mesh is required near the wall in order to resolve the boundary layer. This leads to an expensive calculation because of the small time step due to the stability restriction.

A large and productive effort has been occurred in the area of implicit schemes. Polezhaev(1967) proposed an ADI (Alternating Direction Implicit) scheme without an iterative process. Briley and McDonald(1973) applied the generalized ADI procedure to solve the compressible Navier-

Stokes equation. Beam and Warming(1978) solved the compressible Navier-Stokes equation by the implicit method, which was the same class of ADI schemes developed by McDonald and Briley(1975). MacCormack(1981) developed an implicit scheme analogue of his explicit scheme. Even though implicit schemes are condemned for their large arithmetic operation counts, these schemes have been praised for their improved stability conditions.

In this study, an implicit finite volume, lower-upper time marching code(RPLUS3D), which was developed at NASA Lewis Research Center, is employed, and the boundary conditions and algebraic turbulence model are added in conjunction with the flow physics; the chemical reaction term are eliminated to save the computation time. This computer code employs a lower-upper(LU) factored implicit scheme developed by Jameson and Turkel(1981). This scheme is unconditionally stable in any number of space dimensions. Despite being implicit, the LU scheme requires only scalar diagonal inversions while most other implicit schemes require block matrix inversions. The use of scalar diagonal inversions offers large savings in computation time and temporary storage.

3.1 LU Scheme

The unfactored implicit scheme with time marching for the vectorized Eq. (2.15) can be formulated as follows; viscous terms are treated explicitly to avoid complexity.

$$\begin{aligned}\hat{U}^{n+1} = \hat{U}^n - \Delta t [D_\xi(\hat{E}^{n+1}) + D_\eta(\hat{F}^{n+1}) + D_\zeta(\hat{G}^{n+1})] \\ + \Delta t [D_\xi(\hat{E}_v^n) + D_\eta(\hat{F}_v^n) + D_\zeta(\hat{G}_v^n)]\end{aligned}\quad (3.1)$$

where D_ξ , D_η , and D_ζ are the spatial finite difference operators. The superscript n denotes the time level, i.e., $\hat{U}^n = \hat{U}(n\Delta t)$. The difficulty for solving these algebraic equations comes from the nonlinearity of the set of equation. The linearized equations with the same temporal accuracy can be obtain by the Taylor series expansion.

$$\begin{aligned}\hat{E}(\hat{U}^{n+1}) &= \hat{E}(\hat{U}^n) + \left(\frac{\partial \hat{E}}{\partial \hat{U}} \right)^n (\hat{U}^{n+1} - \hat{U}^n) + O(|\Delta t|^2) \\ \hat{F}(\hat{U}^{n+1}) &= \hat{F}(\hat{U}^n) + \left(\frac{\partial \hat{F}}{\partial \hat{U}} \right)^n (\hat{U}^{n+1} - \hat{U}^n) + O(|\Delta t|^2) \\ \hat{G}(\hat{U}^{n+1}) &= \hat{G}(\hat{U}^n) + \left(\frac{\partial \hat{G}}{\partial \hat{U}} \right)^n (\hat{U}^{n+1} - \hat{U}^n) + O(|\Delta t|^2)\end{aligned}\quad (3.2)$$

Let the linearized flux Jacobians of the convective flux vectors be

$$\hat{A} = \frac{\partial \hat{E}}{\partial \hat{U}}, \quad \hat{B} = \frac{\partial \hat{F}}{\partial \hat{U}}, \quad \hat{C} = \frac{\partial \hat{G}}{\partial \hat{U}} \quad (3.3)$$

and the correction be $\Delta \hat{U} = \hat{U}^{n+1} - \hat{U}^n$. The Jacobian matrices \hat{A} , \hat{B} , and \hat{C} are given in Appendix A.

This unfactored implicit scheme is first order accurate in time. Therefore, the second higher order terms can be neglected without loss of time accuracy of the linearized governing equations.

$$\begin{aligned} & [I + \Delta t (D_\xi \hat{A} + D_\eta \hat{B} + D_\zeta \hat{C})] \Delta \hat{U} \\ & = -\Delta t [D_\xi (\hat{E} - \hat{E}_v) + D_\eta (\hat{F} - \hat{F}_v) + D_\zeta (\hat{G} - \hat{G}_v)] \end{aligned} \quad (3.4)$$

The linearized Eq. (3.4) with the unfactored implicit scheme has large block banded matrices, which require large storage and computation time for inversion. The Eq. (3.4) can be factorized by replacing the operator with a product of three one-dimensional operators. This is same as the ADI scheme, which also requires inversions of block tridiagonal or block pentadiagonal matrices. If one solves the block tridiagonal system by Gaussian elimination without pivoting, the operation count for the block Thomas algorithm is $O(NM^3)$ where M is the block size and N is the number of unknowns. Clearly it is desirable to avoid solving a block tridiagonal system. For many standard

algorithms, one can not be confident that the Thomas algorithm is numerically stable if the diagonal dominance is lost by increasing time steps.

Jameson and Turkel(1981) proposed the idea of a lower-upper factored implicit scheme that is unconditionally stable in any number of space dimensions and also yields a steady-state solution that is independent of Δt . The LU implicit scheme needs only two factors even for three-dimensional problems because of the unique manner of splitting. As a result, this scheme is more stable and robust than ADI schemes. Let

$$\begin{aligned}\hat{A} &= \hat{A}^+ + \hat{A}^- \\ \hat{B} &= \hat{B}^+ + \hat{B}^- \\ \hat{C} &= \hat{C}^+ + \hat{C}^-\end{aligned}\tag{3.5}$$

The split flux Jacobians, \hat{A}^+ , \hat{B}^+ , \hat{C}^+ , \hat{A}^- , \hat{B}^- and \hat{C}^- are constructed such that the eigenvalues of "+" matrices are nonnegative and those of "-" matrices are nonpositive. Of the many ways of splitting, Jameson and Yoon's(1987) method is employed as follows:

$$\begin{aligned}
\hat{A}^+ &= 0.5 (\hat{A} + \gamma_{\hat{A}} \mathbf{I}) \\
\hat{A}^- &= 0.5 (\hat{A} - \gamma_{\hat{A}} \mathbf{I}) \\
\hat{B}^+ &= 0.5 (\hat{B} + \gamma_{\hat{B}} \mathbf{I}) \\
\hat{B}^- &= 0.5 (\hat{B} - \gamma_{\hat{B}} \mathbf{I}) \\
\hat{C}^+ &= 0.5 (\hat{C} + \gamma_{\hat{C}} \mathbf{I}) \\
\hat{C}^- &= 0.5 (\hat{C} - \gamma_{\hat{C}} \mathbf{I})
\end{aligned} \tag{3.6}$$

where $\gamma_{\hat{A}}$, $\gamma_{\hat{B}}$ and $\gamma_{\hat{C}}$ are greater than the spectral radii of the flux Jacobians associated with them:

$$\begin{aligned}
\gamma_{\hat{A}} &= \max (|\lambda_{\hat{A}}|) \\
\gamma_{\hat{B}} &= \max (|\lambda_{\hat{B}}|) \\
\gamma_{\hat{C}} &= \max (|\lambda_{\hat{C}}|)
\end{aligned} \tag{3.7}$$

Here, $\lambda_{\hat{A}}$, $\lambda_{\hat{B}}$ and $\lambda_{\hat{C}}$ represent eigenvalues of Jacobian matrices \hat{A} , \hat{B} and \hat{C} . The spectral radii and eigenvalues of Jacobian matrices are obtained in section 3.3.

Substituting Eq. (3.5) into Eq. (3.4) and performing the first order upwind difference according to the sign of the eigenvalues, The linearized implicit scheme can be obtained:

$$\begin{aligned}
&[\mathbf{I} + \Delta \tau (D_{\xi}^- \hat{A}^+ + D_{\eta}^- \hat{B}^+ + D_{\zeta}^- \hat{C}^+ + D_{\xi}^+ \hat{A}^- + D_{\eta}^+ \hat{B}^- + D_{\zeta}^+ \hat{C}^-)]_{\Delta} \hat{\mathbf{U}} \\
&= -\Delta \tau [D_{\xi} (\hat{\mathbf{E}} - \hat{\mathbf{E}}_v) + D_{\eta} (\hat{\mathbf{F}} - \hat{\mathbf{F}}_v) + D_{\zeta} (\hat{\mathbf{G}} - \hat{\mathbf{G}}_v)] \tag{3.8}
\end{aligned}$$

where D_ξ^- , D_η^- , and D_ζ^- denotes backward-difference operators while D_ξ^+ , D_η^+ , D_ζ^+ are forward-difference operators. Eq. (3.8) can be expanded in discretized form as follows:

$$\begin{aligned} \Delta \hat{U}_{i,j,k} + \Delta t (\hat{A}_{i,j,k}^+ \Delta \hat{U}_{i,j,k} - \hat{A}_{i-1,j,k}^+ \Delta \hat{U}_{i-1,j,k} + \hat{A}_{i+1,j,k}^- \Delta \hat{U}_{i+1,j,k} \\ - \hat{A}_{i,j,k}^- \Delta \hat{U}_{i,j,k} + \hat{B}_{i,j,k}^+ \Delta \hat{U}_{i,j,k} - \hat{B}_{i-1,j,k}^+ \Delta \hat{U}_{i-1,j,k} + \hat{B}_{i+1,j,k}^- \Delta \hat{U}_{i+1,j,k} \\ - \hat{B}_{i,j,k}^- \Delta \hat{U}_{i,j,k} + \hat{C}_{i,j,k}^+ \Delta \hat{U}_{i,j,k} - \hat{C}_{i-1,j,k}^+ \Delta \hat{U}_{i-1,j,k} + \hat{C}_{i+1,j,k}^- \Delta \hat{U}_{i+1,j,k} \\ - \hat{C}_{i,j,k}^- \Delta \hat{U}_{i,j,k}) = \Delta t RHS \end{aligned} \quad (3.9)$$

where

$$RHS = D_\xi (\hat{E} - \hat{E}_v) + D_\eta (\hat{F} - \hat{F}_v) + D_\zeta (\hat{G} - \hat{G}_v) \quad (3.10)$$

This discretized equation can be written as

$$\begin{aligned} [\{ I + \Delta t (\hat{A}^+ - \hat{A}^- + \hat{B}^+ - \hat{B}^- + \hat{C}^+ - \hat{C}^-) \} \\ + \Delta t (D_\xi^- \hat{A}^- + D_\eta^- \hat{B}^- + D_\zeta^- \hat{C}^- - \hat{A}^+ - \hat{B}^+ - \hat{C}^+) \\ + \Delta t (D_\xi^+ \hat{A}^+ + D_\eta^+ \hat{B}^+ + D_\zeta^+ \hat{C}^+ + \hat{A}^- + \hat{B}^- + \hat{C}^-)] \Delta \hat{U} \\ = \Delta t RHS \end{aligned} \quad (3.11)$$

Eq. (3.11) can be factorized according to the sign of the Jacobian matrices

$$\begin{aligned} \{ K + \Delta t (D_\xi^- \hat{A}^- + D_\eta^- \hat{B}^- + D_\zeta^- \hat{C}^- - \hat{A}^+ - \hat{B}^+ - \hat{C}^+) \} (K)^- \\ \{ K + \Delta t (D_\xi^+ \hat{A}^+ + D_\eta^+ \hat{B}^+ + D_\zeta^+ \hat{C}^+ + \hat{A}^- + \hat{B}^- + \hat{C}^-) \} \Delta \hat{U} \\ = \Delta t RHS \end{aligned} \quad (3.12)$$

where

$$K = I + \Delta t (\hat{A}^+ - \hat{A}^- + \hat{B}^+ - \hat{B}^- + \hat{C}^+ - \hat{C}^-) \quad (3.13)$$

Notes that matrix K is diagonal. This can be easily

verified by substituting Eq. (3.6) into Eq. (3.13). K' is also diagonal and can be moved to the right hand side.

$$\begin{aligned} & \{ I + \Delta t (D_{\xi}^{-} \hat{A}^{*} + D_{\eta}^{-} \hat{B}^{*} + D_{\zeta}^{-} \hat{C}^{*} - \hat{A}^{-} - \hat{B}^{-} - \hat{C}^{-}) \} \\ & \{ I + \Delta t (D_{\xi}^{+} \hat{A}^{-} + D_{\eta}^{+} \hat{B}^{-} + D_{\zeta}^{+} \hat{C}^{-} + \hat{A}^{*} + \hat{B}^{*} + \hat{C}^{*}) \} \Delta U \\ & = \Delta t \{ I + \Delta t (\gamma_{\hat{A}} + \gamma_{\hat{B}} + \gamma_{\hat{C}}) I \} RHS \end{aligned} \quad (3.14)$$

The operator on the left hand side of Eq. (3.14) represents Lower and Upper operator of this scheme. These two operator represent forward and backward substitutions. It is interesting to note that if there is no source term in the governing equation, the numerical method completely eliminates the need for block matrix inversion. In fact, the two operators in Eq. (3.14) require only scalar inversions. Although the LU scheme is an implicit scheme, the numerical operation counts are not much different from those of explicit methods.

The discretized equation in the finite volume method is derived by approximating the integral form of the equation to be solved. The computational region is divided into elementary quadrilateral volumes within which the integration is carried out, and the integral equation is evaluated at each subdomain. This method can easily handle the complicated geometry without considering the equation written in curvilinear coordinates. It makes it possible to avoid problems with metric singularities that are usually

associated with finite difference methods. If this method is applied on the uniform rectangular grid, the discretized equation will be equal to the discretized equation using the central finite difference method. It has second order accuracy in space, but for the non-uniform grid the convergence rate in space is less than second order.

3.2 Artificial Dissipation

The finite volume formulation reduces to a central difference approximation on a uniform grid. It allows undamped oscillations with alternative signs at odd and even mesh points. Wiggles appear in the neighborhood of severe pressure gradient regions or stagnation points. These spurious oscillations can not be smoothed out totally by the viscous and dissipation terms. In order to suppress these numerical oscillations, the artificial dissipation terms are added into the LU scheme.

In this study, Jameson's(1981) adaptive artificial dissipation scheme is employed. The dissipation terms consist of blended second and fourth order differences. The fourth order difference terms provide background dissipation throughout the flow field to prevent odd-even decoupling which occurs from the linearized Euler equation terms. The second order dissipation terms are used to

stabilize the flow calculation near the regions of the strong pressure gradients. These terms are explicitly added to the RHS term as an additional residual. The added dissipation term are as follows:

$$\begin{aligned}
& D_{\xi}^{-} \left(\epsilon_{i+\frac{1}{2},j,k}^{(2)} D_{\xi}^{+} \left(\frac{\hat{U}}{J} \right)_{i,j,k} - \epsilon_{i+\frac{1}{2},j,k}^{(4)} D_{\xi}^{+} D_{\xi}^{-} D_{\xi}^{+} \left(\frac{\hat{U}}{J} \right)_{i,j,k} \right) \\
& + D_{\eta}^{-} \left(\epsilon_{i,j+\frac{1}{2},k}^{(2)} D_{\eta}^{+} \left(\frac{\hat{U}}{J} \right)_{i,j,k} - \epsilon_{i,j+\frac{1}{2},k}^{(4)} D_{\eta}^{+} D_{\eta}^{-} D_{\eta}^{+} \left(\frac{\hat{U}}{J} \right)_{i,j,k} \right) \\
& + D_{\zeta}^{-} \left(\epsilon_{i,j,k+\frac{1}{2}}^{(2)} D_{\zeta}^{+} \left(\frac{\hat{U}}{J} \right)_{i,j,k} - \epsilon_{i,j,k+\frac{1}{2}}^{(4)} D_{\zeta}^{+} D_{\zeta}^{-} D_{\zeta}^{+} \left(\frac{\hat{U}}{J} \right)_{i,j,k} \right)
\end{aligned} \tag{3.15}$$

where

$$\epsilon_{i+\frac{1}{2},j,k}^{(2)} = \kappa_2 \chi_{i+\frac{1}{2},j,k} \max \left(\bar{v}_{i+2,j,k}, \bar{v}_{i+1,j,k}, \bar{v}_{i,j,k}, \bar{v}_{i-1,j,k} \right) \tag{3.16}$$

$$\bar{v}_{i,j,k} = \left| \frac{p_{i+1,j,k} - 2p_{i,j,k} + p_{i-1,j,k}}{p_{i+1,j,k} + 2p_{i,j,k} + p_{i-1,j,k}} \right| \tag{3.17}$$

$$\chi_{i+\frac{1}{2},j,k} = \min \left((J\hat{q})_{i+1,j,k}, (J\hat{q})_{i,j,k} \right) \tag{3.18}$$

$$\epsilon_{i+\frac{1}{2},j,k}^{(4)} = \max \left(0, \kappa_4 - \epsilon_{i+\frac{1}{2},j,k}^{(2)} \right) \tag{3.19}$$

κ_2 and κ_4 are scalar constants. In this study, κ_2 and κ_4 are 1 and 1/32, respectively, and the magnitudes of artificial dissipation coefficients are much less than the eddy viscosity in the boundary layer. The term $\hat{\gamma}_{i,j,k}$ is a spectral

radius scaling factor and is defined as

$$\begin{aligned}
 \gamma_{i,j,k} &= \gamma_{\hat{A}} + \gamma_{\hat{B}} + \gamma_{\hat{C}} \\
 &= |\xi_x| |u| + |\xi_y| |v| + |\xi_z| |w| + c (\xi_x^2 + \xi_y^2 + \xi_z^2)^{\frac{1}{2}} \\
 &\quad + |\eta_x| |u| + |\eta_y| |v| + |\eta_z| |w| + c (\eta_x^2 + \eta_y^2 + \eta_z^2)^{\frac{1}{2}} \\
 &\quad + |\zeta_x| |u| + |\zeta_y| |v| + |\zeta_z| |w| + c (\zeta_x^2 + \zeta_y^2 + \zeta_z^2)^{\frac{1}{2}}
 \end{aligned} \tag{3.20}$$

which is the sum of the spectral radii of \hat{A} , \hat{B} and \hat{C} .

The first terms in the parentheses of Eq. (3.15) are the second order dissipation. It has an extra pressure gradient coefficient which is constructed by taking the second difference of the pressure. Its value increases in the neighborhood of the strong pressure gradient region, so the non-physical overshoot or undershoot are eliminated by the second order term. The second terms in the parentheses of Eq. (3.15) are the fourth order dissipation. The coefficient $\varepsilon^{(4)}$ switches off when the second order nonlinear coefficient is larger than the constant of the fourth order coefficient.

3.3 Eigenvalues of Jacobian Matrices

The eigenvalues of Jacobian matrices are required to

analyze the stability of a numerical scheme. The Jacobian matrices of non-conservative equation (\bar{A} , \bar{B} and \bar{C}) are much simpler than the Jacobian matrices of conservative equation (A , B and C). Warming et al. (1975) showed that an uniformly bounded similarity transformation between the Jacobian matrices of non-conservative equation and conservative equation existed in the invicid gas dynamic equations. The Jacobians of the generalized transformed convective flux vectors can be expressed by the Jacobians of conservative equation.

$$\begin{aligned}\hat{A} &= \frac{\partial \hat{E}}{\partial \hat{U}} = \xi_x \frac{\partial E}{\partial U} + \xi_y \frac{\partial F}{\partial U} + \xi_z \frac{\partial G}{\partial U} = \xi_x A + \xi_y B + \xi_z C \\ \hat{B} &= \frac{\partial \hat{F}}{\partial \hat{U}} = \eta_x \frac{\partial E}{\partial U} + \eta_y \frac{\partial F}{\partial U} + \eta_z \frac{\partial G}{\partial U} = \eta_x A + \eta_y B + \eta_z C \quad (3.21) \\ \hat{C} &= \frac{\partial \hat{G}}{\partial \hat{U}} = \zeta_x \frac{\partial E}{\partial U} + \zeta_y \frac{\partial F}{\partial U} + \zeta_z \frac{\partial G}{\partial U} = \zeta_x A + \zeta_y B + \zeta_z C\end{aligned}$$

Using the similarity transformation, Eq. (3.21) is changed to the simple form.

$$\begin{aligned}\hat{A} &= M (\xi_x \bar{A} + \xi_y \bar{B} + \xi_z \bar{C}) M^{-1} \\ \hat{B} &= M (\eta_x \bar{A} + \eta_y \bar{B} + \eta_z \bar{C}) M^{-1} \\ \hat{C} &= M (\zeta_x \bar{A} + \zeta_y \bar{B} + \zeta_z \bar{C}) M^{-1}\end{aligned} \quad (3.22)$$

It is not hard to find the eigenvalues of the Jacobian matrices in the non-conservative equation. The eigenvalues

of \bar{A} are as follows:

$$\begin{aligned}\bar{\lambda}_{1,2,3} &= u \\ \bar{\lambda}_4 &= u + c \\ \bar{\lambda}_5 &= u - c\end{aligned}\tag{3.23}$$

The eigenvalues of \bar{B} and \bar{C} are similar to those of \bar{A} , only u in the eigenvalue of \bar{A} has to replace to v and w , respectively.

The eigenvalues of \hat{A} , \hat{B} and \hat{C} are easily obtained using the Eq. (3.23). The eigenvalue of \hat{A} are as follows:

$$\begin{aligned}\hat{\lambda}_{1,2,3} &= \xi_x u + \xi_y v + \xi_z w \\ \hat{\lambda}_4 &= \xi_x u + \xi_y v + \xi_z w + c (\xi_x^2 + \xi_y^2 + \xi_z^2)^{\frac{1}{2}} \\ \hat{\lambda}_5 &= \xi_x u + \xi_y v + \xi_z w - c (\xi_x^2 + \xi_y^2 + \xi_z^2)^{\frac{1}{2}}\end{aligned}\tag{3.24}$$

The eigenvalues of \hat{B} and \hat{C} are similar to those of \hat{A} , only ξ in the eigenvalues of \hat{A} has to replace to η and ζ , respectively.

In order to obtain the bound of the spectral radii in the flux Jacobians, the biggest eigenvalue is tested.

$$\begin{aligned}
\gamma_{\hat{A}} &= \max (\hat{\lambda}_i)_{i=1,5} \\
&\leq |\xi_x| |u| + |\xi_y| |v| + |\xi_z| |w| + c (\xi_x^2 + \xi_y^2 + \xi_z^2)^{\frac{1}{2}} \\
&\leq AAA (|u| + |v| + |w| + \sqrt{3} c) \\
&\leq AAA (2 \sqrt{u^2 + v^2 + w^2} + 2 c)
\end{aligned} \tag{3.25}$$

where $AAA = \max(\xi_x, \xi_y, \xi_z)$.

Using the same method, the bound of the spectral radii of \hat{B} and \hat{C} can be obtained:

$$\gamma_{\hat{B}} = BBB (2 \sqrt{u^2 + v^2 + w^2} + 2 c) \tag{3.26}$$

$$\gamma_{\hat{C}} = CCC (2 \sqrt{u^2 + v^2 + w^2} + 2 c) \tag{3.27}$$

where $BBB = \max(\eta_x, \eta_y, \eta_z)$ and $CCC = \max(\zeta_x, \zeta_y, \zeta_z)$

CHAPTER 4

DIFFUSING S-DUCT WITHOUT VORTEX GENERATORS

4.1 Geometry and Grid

The geometry of the diffusing S-duct examined in this study is shown in Fig. 4.1. The duct centerline is defined by two circular arcs with identical radii of curvature, which are 5 times the inlet duct diameter, and subtended angle $\theta_{\max}/2 = 30^\circ$. Both arcs lie within the xy-plane as shown in Fig. 4.1. The coordinates (x_{cl}, y_{cl}, z_{cl}) of the duct centerline are given by Eq. (4.1):

For $0 \leq \theta \leq \theta_{\max}/2$

$$x_{cl} = R \sin \theta$$

$$y_{cl} = R \cos \theta - R$$

$$z_{cl} = 0$$

For $\theta_{\max}/2 \leq \theta \leq \theta_{\max}$ (4.1)

$$x_{cl} = 2 R \sin \left(\frac{\theta_{\max}}{2} \right) - R \sin (\theta_{\max} - \theta)$$

$$y_{cl} = 2 R \cos \left(\frac{\theta_{\max}}{2} \right) - R - R \cos (\theta_{\max} - \theta)$$

$$z_{cl} = 0$$

The cross-sectional shape of the duct perpendicular to the centerline is circular. The diameter of the cross section varies with the arc angle θ and is given by Eq. (4.2).

$$\frac{D}{D_i} = 1 + 3 \left(\frac{D_e}{D_i} - 1 \right) \left(\frac{\theta}{\theta_{\max}} \right)^2 - 2 \left(\frac{D_e}{D_i} - 1 \right) \left(\frac{\theta}{\theta_{\max}} \right)^3 \quad (4.2)$$

where D_i and D_e are the diameter at the S-duct inlet and exit, respectively. The area ratio of the duct exit to inlet is 1.51. The offset of the duct resulting from the centerline curvature is $1.34D_i$. The length of the duct measured along the centerline is $5.24D_i$. A straight pipe, which is $4.6D_i$ long, is installed upstream of the S-duct to provide the desired boundary layer thickness at the inlet of the S-duct. In order to minimize any downstream effect, a $9D_e$ straight section of pipe is attached at the exit of the S-duct. The average inlet Mach number is 0.6 and the Reynolds number based on the duct diameter is 1.76×10^6 .

In the present study, an O-grid is adopted because it conforms well to the boundaries of the circular duct. The O-grid consists of 47 radial points, 42 circumferential points in the half duct, and 70 streamwise nodal points. A finer grid is used in the region of flow separation. Exponential stretching is used to obtain a fine mesh near the wall. The upstream and downstream lengths of straight ducts are also extended using the exponential stretching. The mesh size adjacent to the duct surface is almost 1.25×10^{-4} times the duct inlet diameter. The two grid points

nearest the wall are at value of y^+ of about 2.6 and 5.7 at the reference station ($S/D_i = -1.5$).

The computed results do not depend on the initial velocity conditions, i.e., the initial velocity profile with or without adjusting the axial velocity by the one-seventh power velocity distribution law near the wall. The mass flow changes between the inlet and exit was within 1 percent for all calculations. The residuals for these numerical solutions were reduced approximately three orders of magnitude. Solutions were obtained on the Cray-YMP. The number of iterations required to obtain the converged solutions was approximately 40,000. The computational speed was approximately 960 iterations per CPU hour.

4.2 Results and Discussion

When discussing numerical and experimental results, streamwise position will refer to the distance to cross stream-planes measured from the inlet of S-duct along the duct centerline and normalized by the duct inlet diameter. Position within cross stream-planes is specified by the polar angle ϕ , measured from the vertical in a positive clockwise direction as shown in Fig. 4.1, and the radial distance from the centerline of the duct.

Fig. 4.2 shows the surface static-pressure distributions at $\varphi = 10^\circ, 90^\circ$ and 170° which are compared with two experimental data. Note that the definition of the surface static-pressure coefficient in the two experiments is different. Vakili et al.(1986) measured the reference flow parameters at $S/D_i = -1.5$, upstream of the S-duct for normalizing downstream flow data. The reference variables were evaluated at the center of the duct.

Wellborn et al.(1992) measured the reference flow parameters at $S/D_i = -0.5$, upstream of the S-duct. The reference dynamic pressure was evaluated by subtracting the wall static-pressure from the total-pressure measured at the center of the duct. They used a similar duct but larger than that used by Vakili et al.(1986); therefore, the Reynolds number of Wellborn et al.(1992) experiment is 47% higher than that of Vakili et al.(1986) experiment. However, In this study, calculations were made using the same Reynolds number as the Vakili et al.(1986) experiment.

The computed surface static-pressure distributions are in good agreement with the experimental data except in the separation region. In the separation region, the predicted values of surface static-pressure are higher than the two experimental results. Both experimental data show constant values of static-pressure at $\varphi = 90^\circ$ and 170° in the region

$2 \leq S/D_i \leq 3$; the computational result shows a similar result in the region $3 \leq S/D_i \leq 4$.

The experimental flow separation region shown in Fig. 4.2 was determined by surface oil flow visualization. The computed flow separation region is determined by examining the streamwise velocity in the vertical plane of symmetry. The predicted separation length is 1.94, which is a little shorter than the experimental value of 2.1. The predicted separation ($2.44 < S/D_i < 4.40$) occurs farther downstream than was observed experimentally ($2.02 < S/D_i < 4.13$). This indicates that the applied turbulence model, even as modified, cannot correctly account for the three-dimensional separation flow with very strong secondary flow. The experimental and numerical results show that the flow fields in a diffusing S-duct have strong secondary velocities with flow separation, and the counter-rotating vortices resulting from the flow separation are stretched into the second half bend of the duct by the streamwise velocity. These complex flow fields result in the moment of vorticity($F(y)$) having several peak values along the normal direction from the wall. Although the first peak value from the wall is chosen as the length scale(y_{max}) in order to avoid choosing an inappropriate length scale, this chosen length scale in the flow separation region cannot be

considered as a perfectly correct length scale.

The reverse flow in a diffusing S-duct is associated with the adverse pressure gradient due to the increase of duct area and the secondary flow due to the duct curvature. Fig. 4.3 shows the velocity profiles in the vertical plane of symmetry. The reverse flow occurs away from the wall; an enlarged view is shown in Fig 4.3(b) to display this feature more clearly. These different characteristics of flow separation can occur due to the turbulence model. If the function $F(y)$ has a peak value close to the wall, the eddy viscosity along the normal direction from the wall approaches quickly to zero by the Klebanoff intermittency factor except the region of the near wall. This incorrect viscosity profile cannot adequately account for the reverse flow associated with the adverse pressure gradient and the strong secondary flow.

Fig. 4.4 shows the surface static-pressure distribution along the circumferential direction at the three different streamwise locations $S/D_i = 0.96, 2.97$ and 4.01 . The computational results at $S/D_i = 0.96$ and 4.01 agree quite well with the experimental data. $S/D_i = 0.96$ and 4.01 are located upstream and downstream of the flow separation region, respectively. The computed values of surface static-pressure at $S/D_i = 2.97$, which is located

within the flow separation region, are higher than the experimental data. This overprediction of surface static-pressure seems to result from the inadequate turbulence model as previously mentioned.

Fig. 4.5 shows the static-pressure contours at the various streamwise locations. The computed results are compared with Vakili et al.s(1987) experimental data. Since the flow is symmetric with respect to a vertical plane passing through the centerline, only half of the plots are shown in these figures. The calculated static-pressure contours show similar trends as the experimental results, but the computed static-pressure levels are higher than the experimental values. The static-pressure coefficient are evaluated as $(p_{\text{local}} - p_{\text{ref}})/q_{\text{ref}}$, and the reference values are measured at the center of duct in the reference plane ($S/D_i = -1.5$). Comparing two experimental results of the surface static-pressure coefficient of Fig. 4.2(a) and the static-pressure coefficient contours of Fig. 4.5, the static-pressure coefficient near the wall in Fig. 4.5 is much lower than that shown in Fig 4.2(a). However, the computed static-pressure coefficient near the wall in Fig. 4.5 are very close to the experimental surface static-pressure coefficient, and also Fig. 4.2(a) shows that the surface static-pressure coefficients, even if at the reference

plane, are much different along the circumferential direction. This probably results from deficiencies in the experiments, primarily coarse data acquisition locations and uncertainties in the static-pressure measurements using pitot tubes.

Figs. 4.5(a) and 4.5(b) show the increase of the static-pressure toward the outer wall in the first half bend. This result is anticipated by the inviscid theory. In the second bend, the static-pressure increases from the upper wall to the lower wall as shown in Figs. 4.5(d) and 4.5(e) due to the adverse curvature direction. The static pressure along the duct increases due to the increase of duct area. The static pressure core shown in Fig. 4.5(e) results from the streamwise velocity deficit at the region of the two counter-rotating vortices. This means that nonuniform flow at the exit occurs from the flow separation.

Total-pressure contours compared with the experimental data obtained by Vakili et al.(1987) are shown in Fig. 4.6. Fig. 4.7 shows the total-pressure contours compared with the experimental data obtained by Wellborn et al.(1992). Note the different definition of the total-pressure coefficient in the two experimental data. The agreement between the computational and experimental results is quite good except downstream of the flow separation. The

disagreement at the downstream of the flow separation caused by the different flow separation region.

A qualitative picture of the secondary flow pattern in a curved duct is that an inviscid core fluid moves toward the outer wall of the duct, and a low speed boundary layer fluid migrates circumferentially from the outer wall to the inner wall in the first half of the S-duct. This phenomenon results in low energy flow accumulating near the inner wall of the first half bend. This is shown in the total-pressure contours of Fig. 4.6(d). The adverse pressure gradient is induced on the second half bend of the duct due to increase of the duct area. The pressure gradient causes a thick boundary layer and deflection of the streamwise flow direction.

The above mentioned secondary flow pattern contributes to the formation of a pair of counter-rotating vortices by the three-dimensional flow separation. Tobak and Peake(1982) showed the topographical structure of three-dimensional flow separation. The counter-rotating vortices formed by the vortex lift-off stretch to the exit of the S-duct by the streamwise velocity, and move away from the wall to the center of the duct. In the region between two counter-rotating vortices, the secondary velocities induced by these vortices push the low energy flow toward the center of the duct. The high energy flow between the

vortices and the duct wall is pushed toward the boundary layer. This mechanism makes the convex shape of the inviscid core flow region as shown in Fig. 4.6(f).

The shape of the total-pressure contours in the cross plane depends on the strength of the counter-rotating vortices and the core location of the vortices in that plane. They are related to the original location of the counter-rotating vortices in the duct. The computed three-dimensional flow separation region occurred further downstream than was observed in the two experiments. This causes the discrepancy between the computational and experimental total pressure contours at $S/D_i = 5.24$ and 5.73.

Comparing Figs. 4.7 and 4.8, we see that axial Mach number contours are very similar to the total-pressure contours at the same axial location. The computational total-pressure contours at $S/D_i = 5.24$ and 5.73 indicate that the computed streamwise velocity deficit ($U_\infty - u$) at the region of the counter-rotating vortices is bigger than was observed experimentally. This large streamwise velocity deficit makes the inviscid core flow region larger in order to satisfy the constant mass flux along the streamwise direction.

Fig. 4.9 shows the secondary velocity profiles at the

five stations along the duct. They are compared with the experimental results obtained by Vakili et al.(1987). Fig. 4.10 is the secondary velocity profiles compared with the experimental results obtained by Wellborn et al.(1992) at $S/D_i = 5.73$. The development of secondary flow in the curved duct is clearly shown in these figures. The computational results are in good agreement with experimental data except downstream of the flow separation region. The secondary velocity profiles in the first bend clearly depict the qualitative picture of the secondary flow pattern in the curved duct as mentioned in the discussion concerning the total-pressure contours.

Fig. 4.9(c) shows the accumulation of low energy flow at the lower wall, which is consistent with the observation of the total-pressure contours. Downstream of the flow separation region, Figs. 4.9 and 4.10 show that a pair of counter-rotating vortices move away from the wall and toward the center of the duct. The computational results show that the secondary velocity is overestimated downstream of flow separation. This results from the small eddy viscosity effect in the flow separation region by the implemented turbulence model, i.e., F_{max} and y_{max} are chosen at the point of the first peak value from the wall in that region.

The variations of boundary layer thickness at $\varphi = 10^\circ$, 90° and 170° along the duct are shown in Fig. 4.11. The boundary layer thickness is defined as the normal distance from the wall where the total-pressure coefficient is 1.0. The predicted results are compared with the experimental results obtained by Vakili et al.(1987). The computational results and experimental data are in reasonable agreement. The rapid boundary layer growth at $\varphi = 170^\circ$ is caused by the flow separation. In the transition region ($S/D_i = 0.0$) from the straight duct into the first bend, the computed results show that the boundary layer thickness at $\varphi = 170^\circ$ is less than that at $\varphi = 10^\circ$. The streamwise velocity near the lower wall in the transition region is faster than that near the upper wall due to the effect of the curved geometry. It was well depicted in the static-pressure contours as shown in Fig. 4.5. The experimental data do not clearly show the effect of this flow mechanism. As shown in the secondary flow pattern of Fig. 4.9, the high energy flow migrates toward the outer wall in the first bend, therefore the boundary layer thickness at $\varphi = 10^\circ$ along the duct is less than that at $\varphi = 90^\circ$ and 170° .

Downstream of the flow separation, the computational result shows that the boundary layer thickness at $\varphi = 90^\circ$ is less than that at $\varphi = 10^\circ$. The reason is that the strong

secondary velocities induced by the counter-rotating vortices push the high energy flow toward the wall. The stronger secondary velocities, as compared with experiments, are associated with the fact the computed total-pressure boundary layer is thinner than the experimentally measured one.

Fig. 4.12 shows the velocity profile along the normal direction from the wall at the four different streamwise locations. The first grid points in the computation are located inside the viscous sublayer ($y^+ < 5$). At the first grid points, the friction velocity is calculated to normalize the velocity profile. The viscous sublayer region, the log linear region, and the wake region are shown in this figure. In Fig. 4.12(b), the velocity profile at $\varphi = 170^\circ$ is not shown because the definition of the friction velocity is not applicable in the flow separation region. At the exit of S-duct ($S/D_i = 5.2$), the flow is reattached but a pair of counter-rotating vortices are present as shown in Fig. 4.9(e). These cause the boundary layer profile to deviate from the law of the wall at $\varphi = 170^\circ$. The velocity profiles at $\varphi = 170^\circ$ show the large streamwise velocity deficit ($U_\infty - u$). Fig. 4.12(d) shows a comparison with the velocity profile measured by Wellborn et al.(1992) at $S/D_i = 5.73$. The agreement in the wake

region is poor because the strength of the counter-rotating vortices was overestimated as previously mentioned.

The skin friction values along the streamwise direction are plotted for $\varphi = 10^\circ$, 90° and 170° in Fig. 4.13. Note that there is no experimental data for the skin friction values. The trends of the computed results are similar to the trends of Bansod and Bradshaw's(1973) experimental data for low speed flow in a nondiffusing S-duct. The skin friction decreases along the duct due to the increase of the duct area.

Fig. 4.14 shows the streamlines in the symmetry plane along the duct. The experimental result was obtained by placing a thin metal plate in the symmetry plane of the S-duct. Even though there is no cross flow in this symmetry plane, the presence of thin plate in the symmetry plane introduces shear layer development and blockage. However, the comparison with Wellborn et al.'s(1992) experimental result agrees well qualitatively.

In the current computations, numerical results demonstrate the capability of a modified algebraic turbulence model in the flow fields of the three-dimensional flow separation with a strong secondary flow. The computed results agree quite well with the experimental results except in the flow separation region. Even though there are deviations between experimental and numerical

results in the flow separation region, the computed results depict well the flow structure in the diffusing S-duct. However, further studies to obtain the correct length scale in the flow separation region are required.

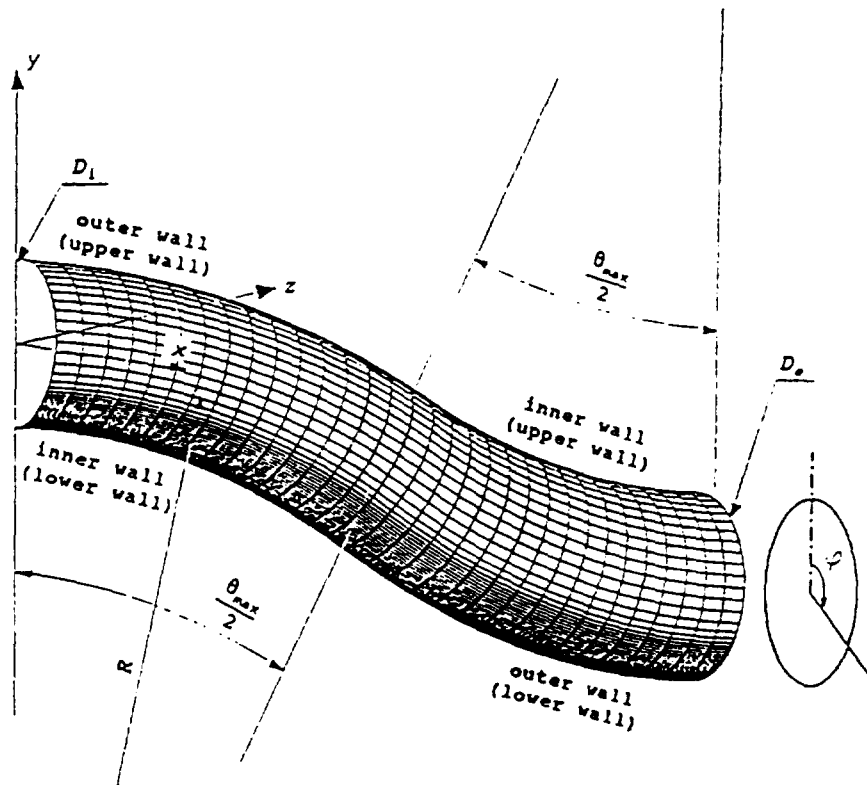


Fig. 4.1(a) The geometry of the diffusing S-duct.

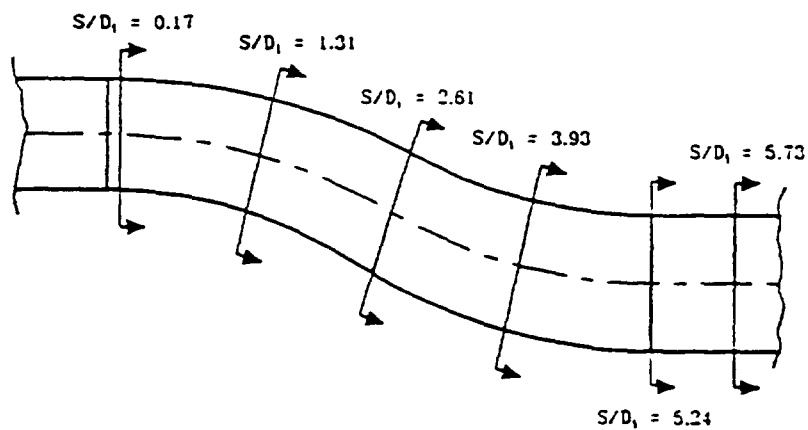


Fig. 4.1(b) Measurement stations along the streamwise direction.

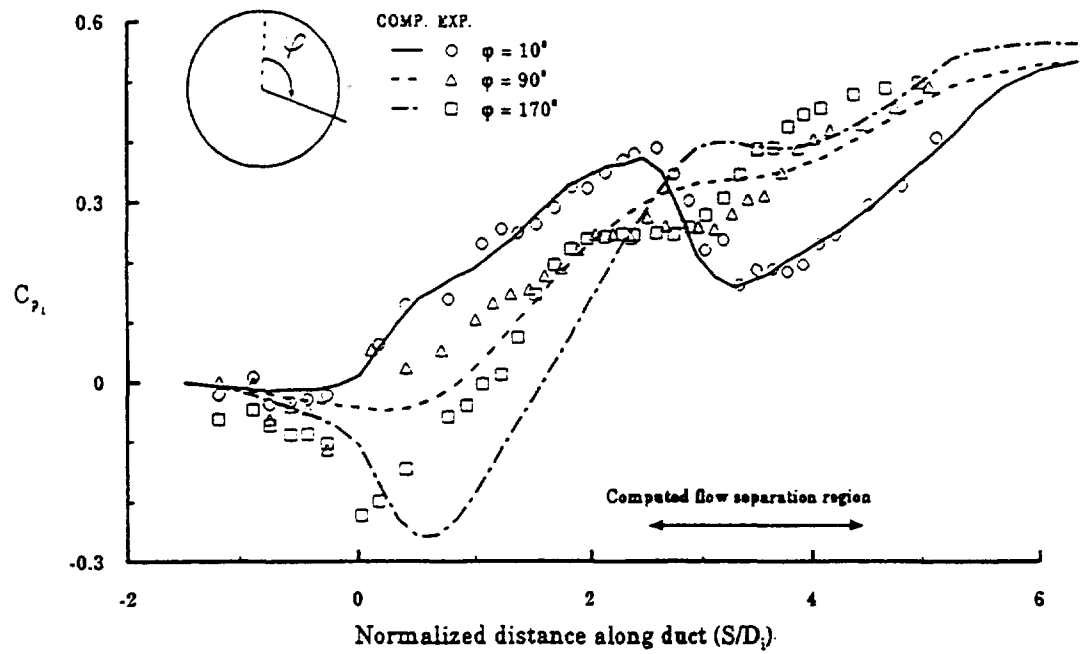


Fig. 4.2(a) Axial surface-static pressure coefficient.

$$C_{pi} = (p_{local} - p_{ref}) / q_{ref}$$

($Ma = 0.6$, $Re_d = 1.76 \times 10^6$)
 Exp. Vakili et al. (1986)

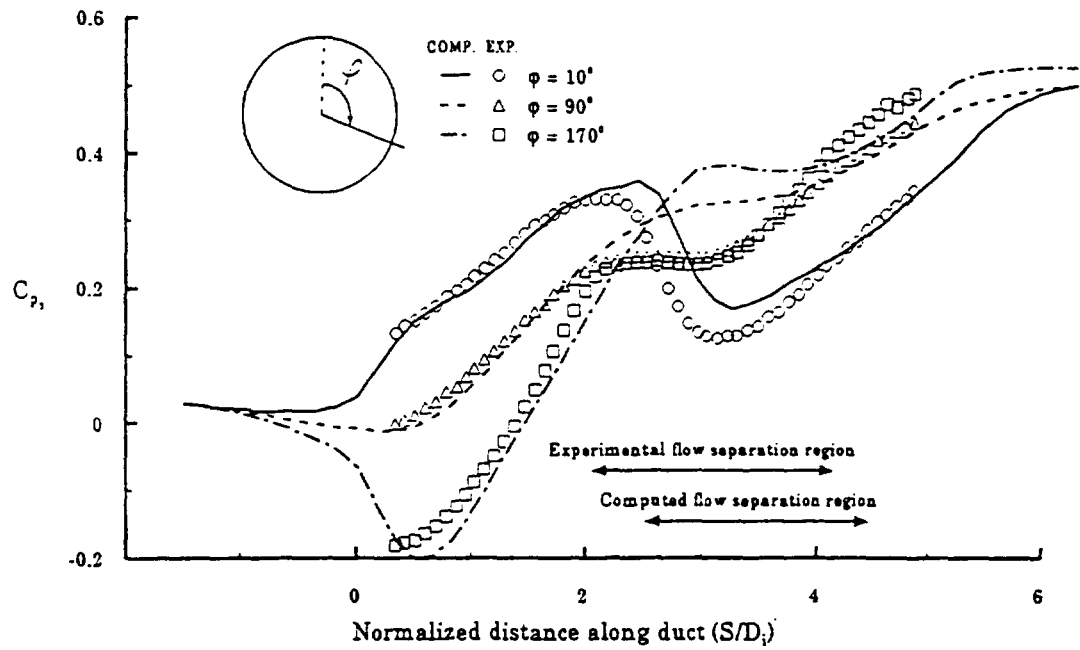
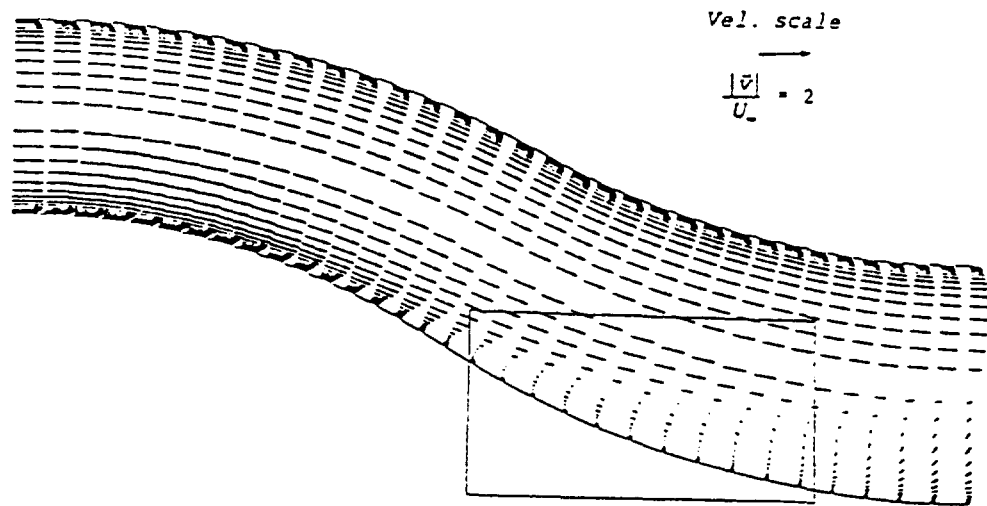


Fig. 4.2(b) Axial surface-static pressure coefficient.

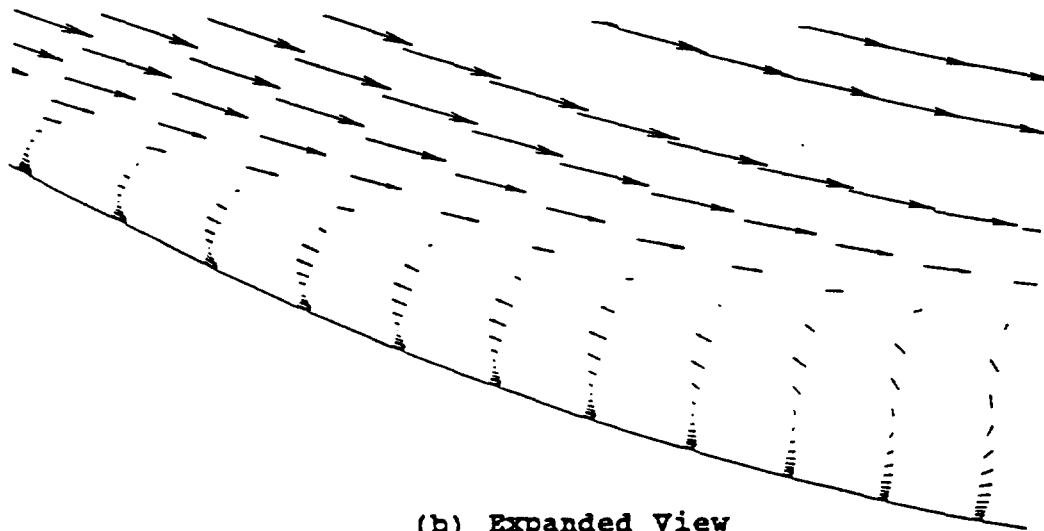
$$C_{p2} = (P_{local} - P_{wall}) / (P_{a,d} - P_{wall})$$

($Ma = 0.6$, $Re_d = 1.76 \times 10^6$)

Exp. Wellborn et al. (1992)
($Ma = 0.6$, $Re_d = 2.6 \times 10^6$)



(a) at Vertical Plane



(b) Expanded View

Fig. 4.3 Streamwise velocity profiles in the vertical plane of symmetry on the S-duct.
 ($Ma = 0.6$, $Re_d = 1.76 \times 10^6$)

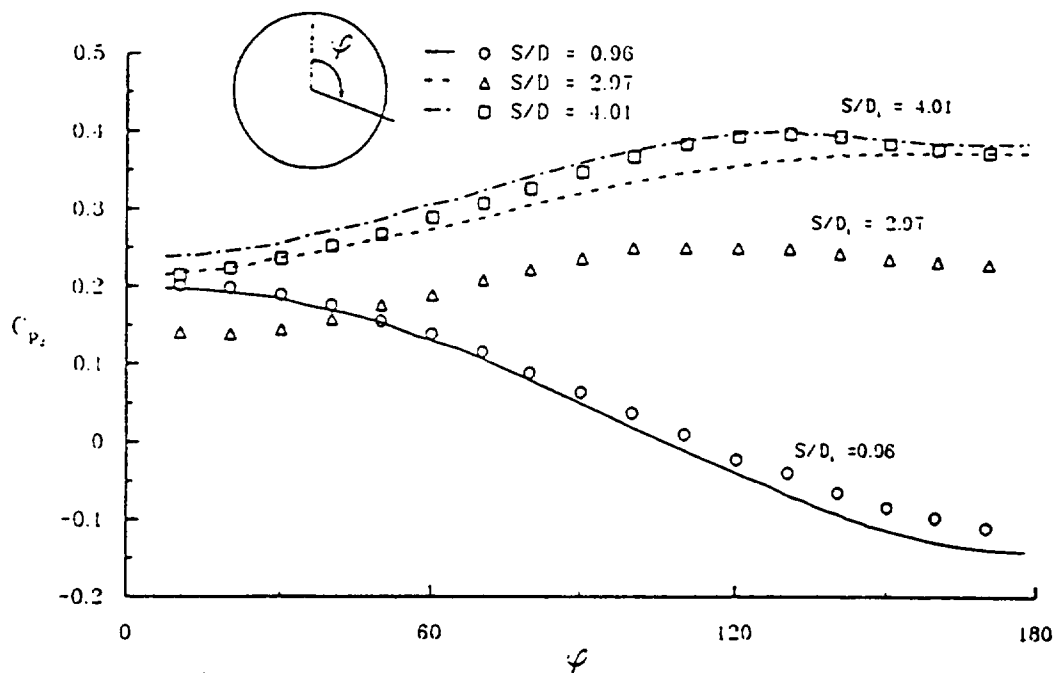


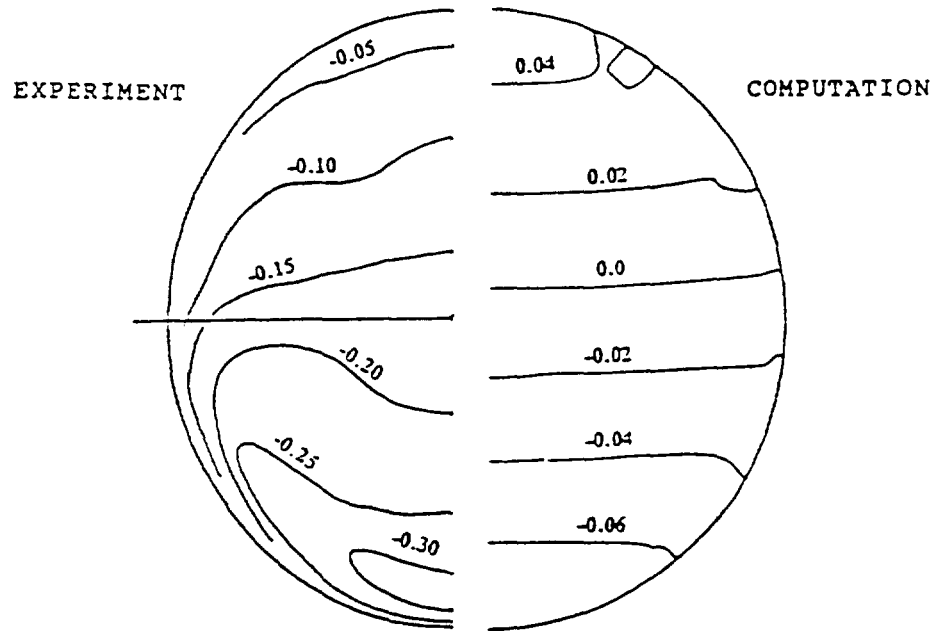
Fig. 4.4 Circumferential surface-static coefficient.

$$C_{p2} = (P_{local} - P_{wall}) / (P_{o,cl} - P_{wall})$$

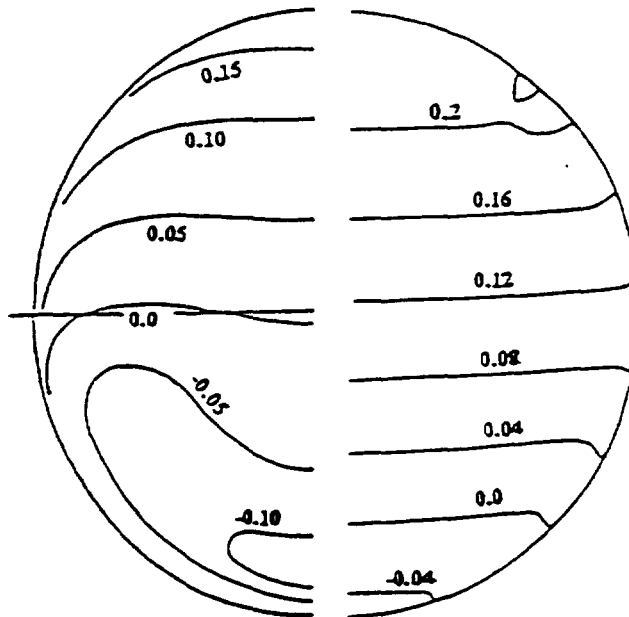
(Ma = 0.6, $Re_d = 1.76 \times 10^6$)

Exp. Wellborn et al. (1992)
(Ma = 0.6, $Re_d = 2.6 \times 10^6$)

STATIC PRESSURE COEFFICIENT CONTOURS
(Without Vortex Generators)



(a) at $S/D_i = 0.17$

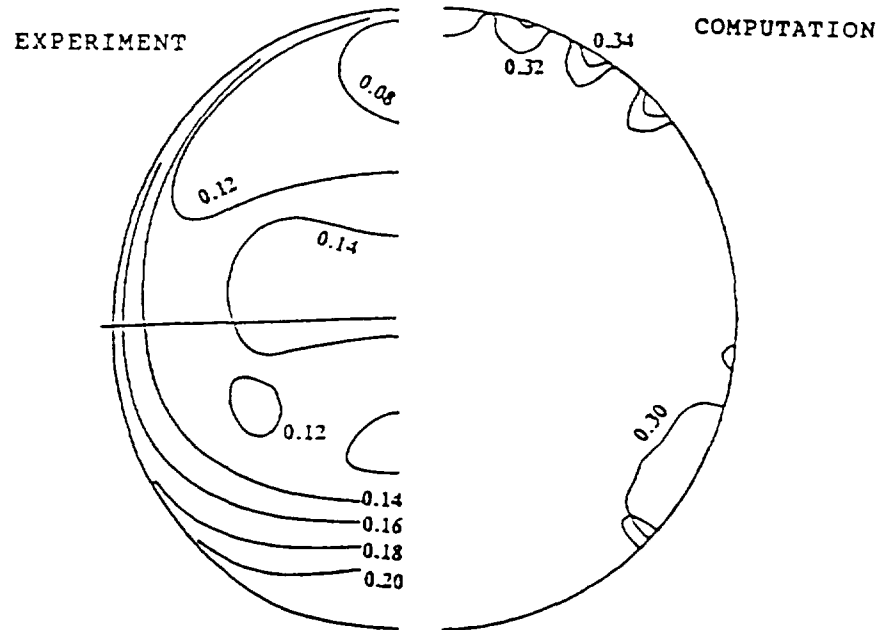


(b) at $S/D_i = 1.31$

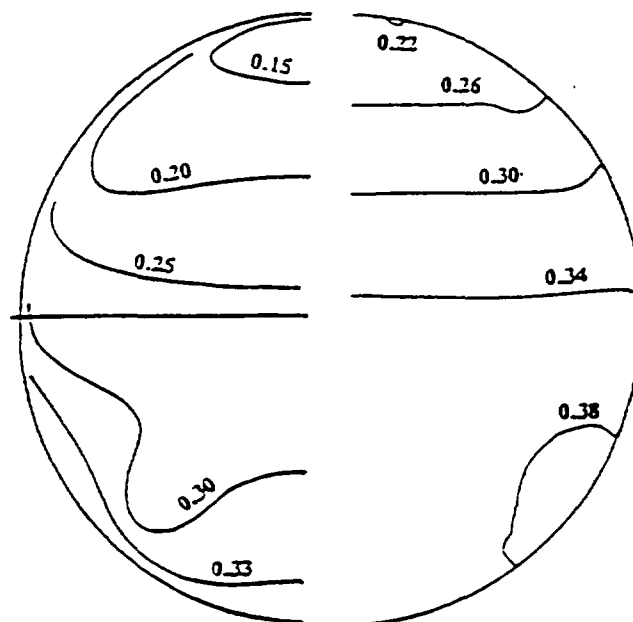
Fig. 4.5 Static-pressure coefficient contours without vortex generators.

($Ma = 0.6$, $Re_d = 1.76 \times 10^6$)

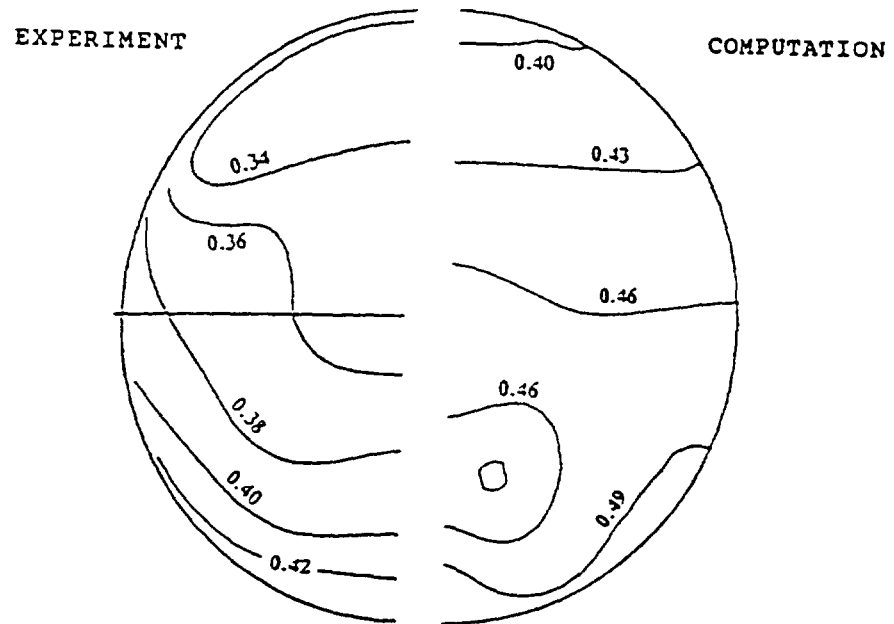
Exp. Vakili et al. (1987)



(c) at $S/D_1 = 2.62$



(d) at $S/D_1 = 3.93$



(e) at $S/D_i = 5.24$

TOTAL PRESSURE COEFFICIENT CONTOURS
(Without Vortex Generators)

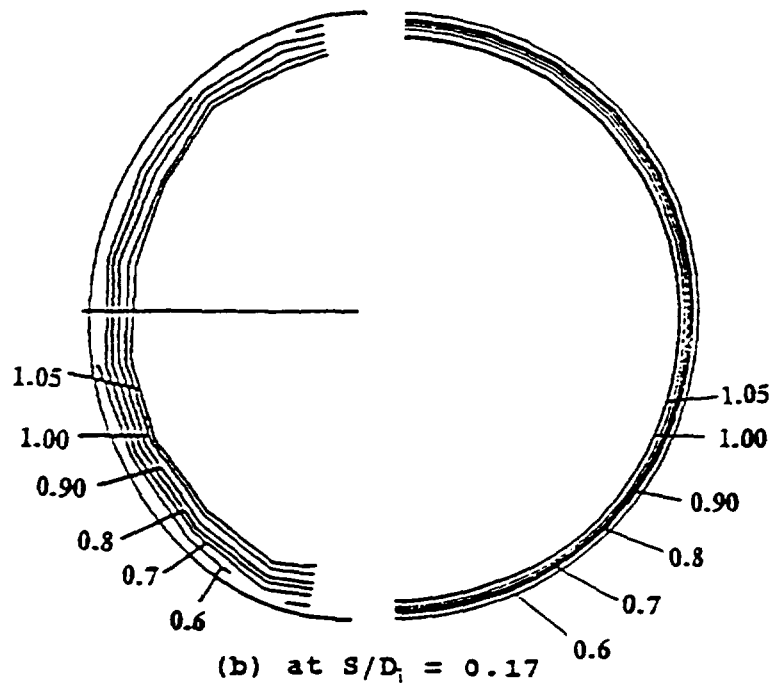
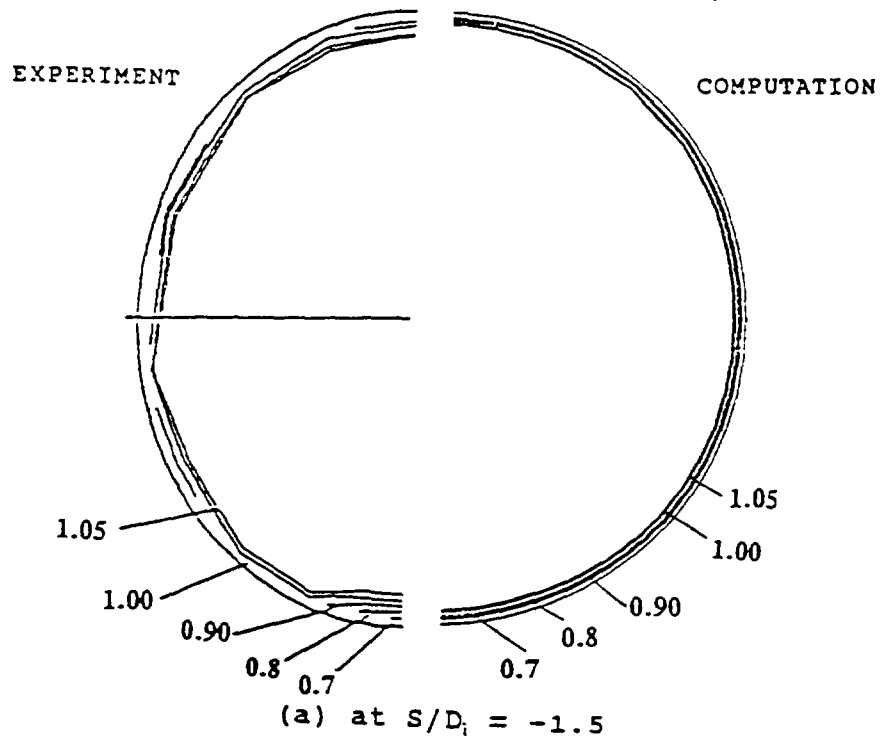
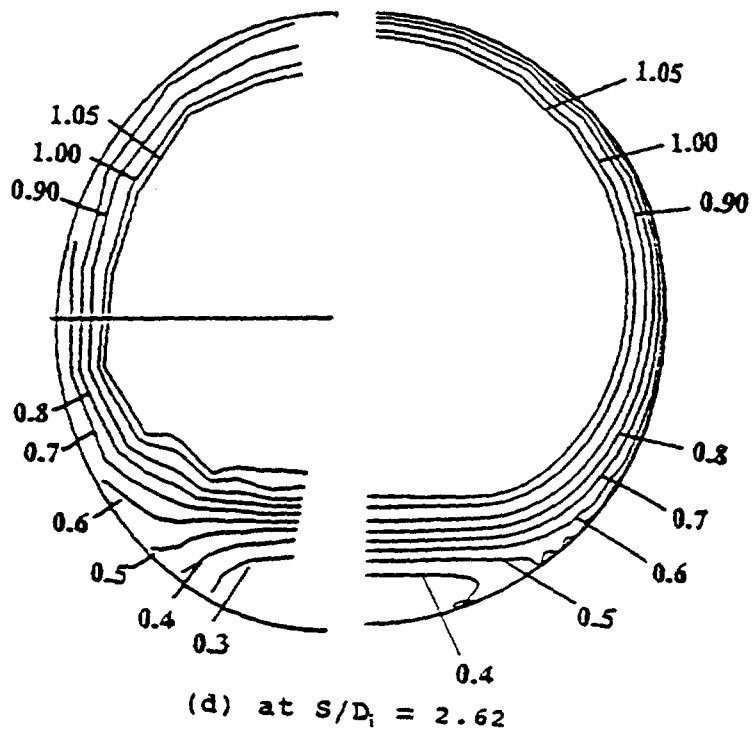
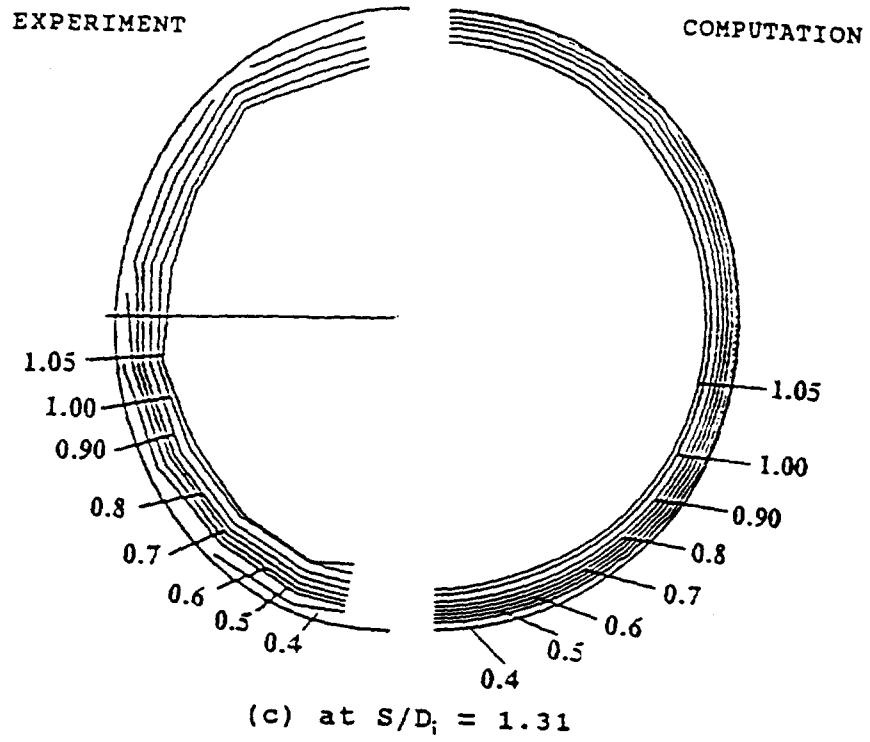


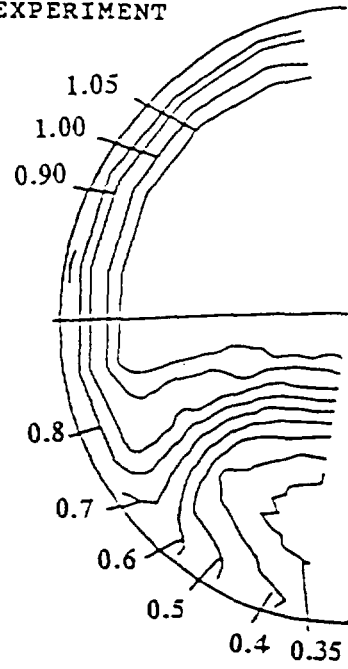
Fig. 4.6 Total-pressure coefficient contours without vortex generators.

($Ma = 0.6$, $Re_d = 1.76 \times 10^6$)

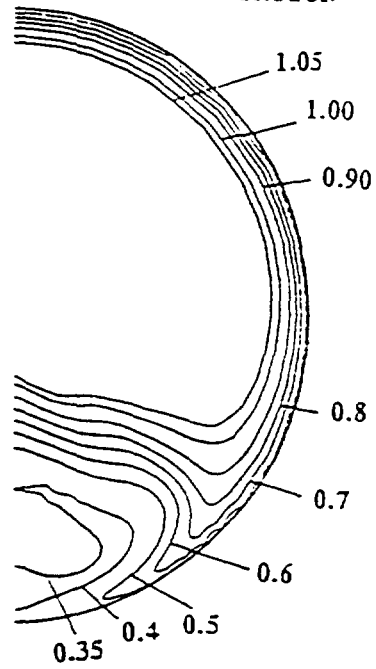
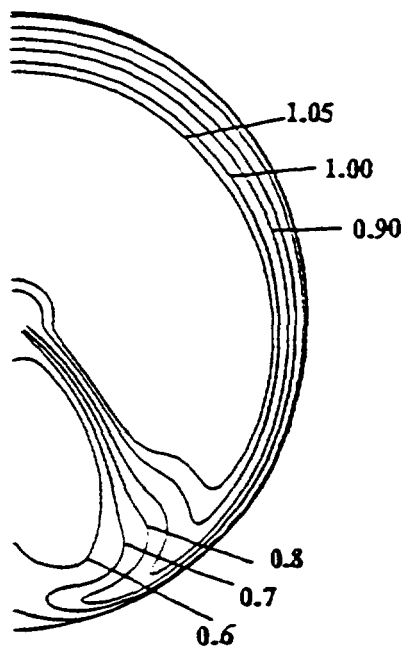
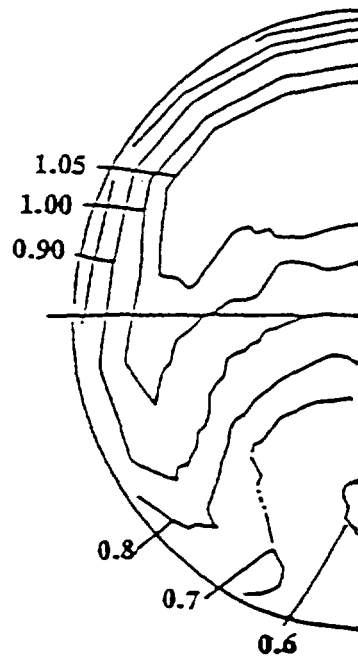
Exp. Vakili et al. (1987)



EXPERIMENT



COMPUTATION

(e) at $S/D_i = 3.93$ (f) at $S/D_i = 5.24$

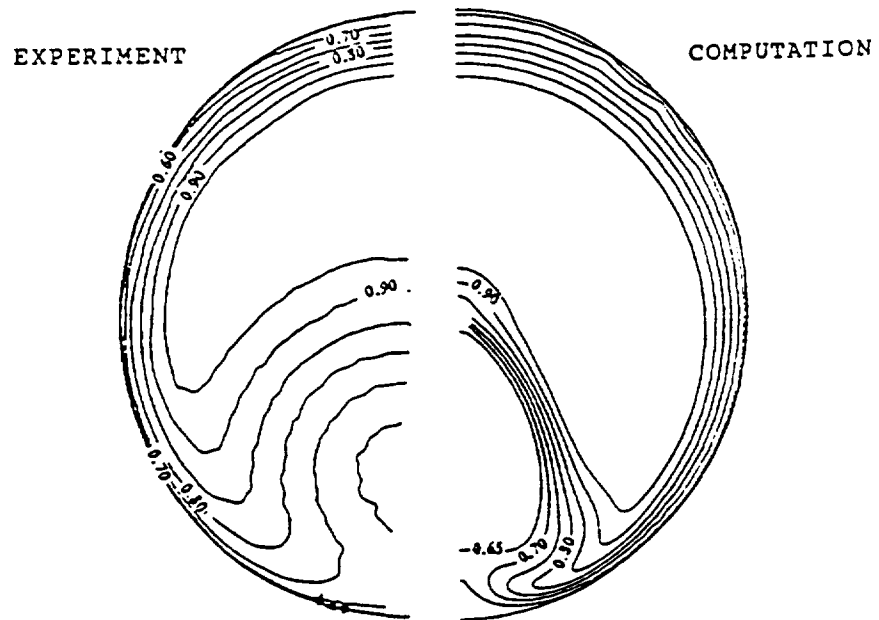


Fig. 4.7 Total-pressure coefficient contours without vortex generators. At $S/D_s = 5.73$
 ($Ma = 0.6$, $Re_d = 1.76 \times 10^6$)

Exp. Wellborn et al. (1992)
 ($Ma = 0.6$, $Re_d = 2.6 \times 10^6$)

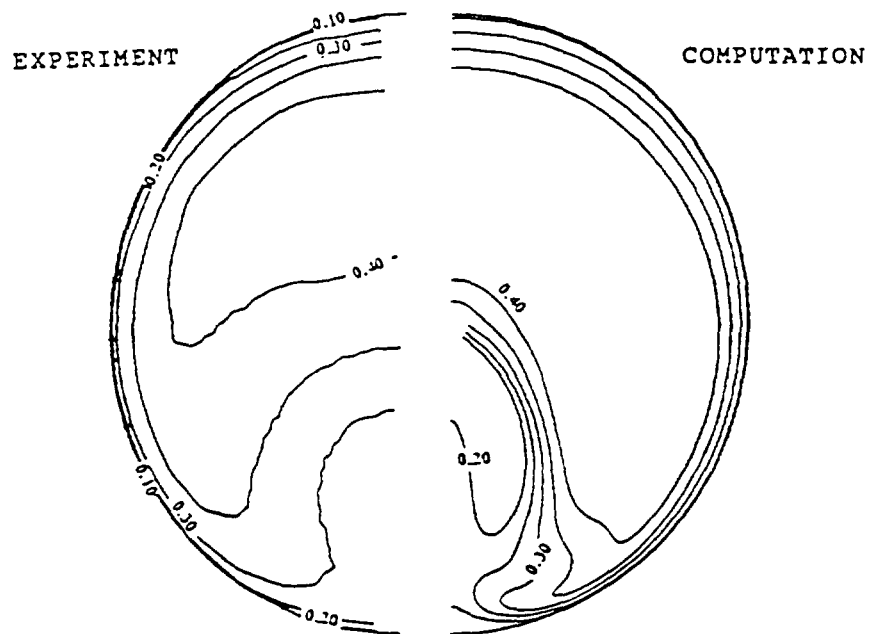
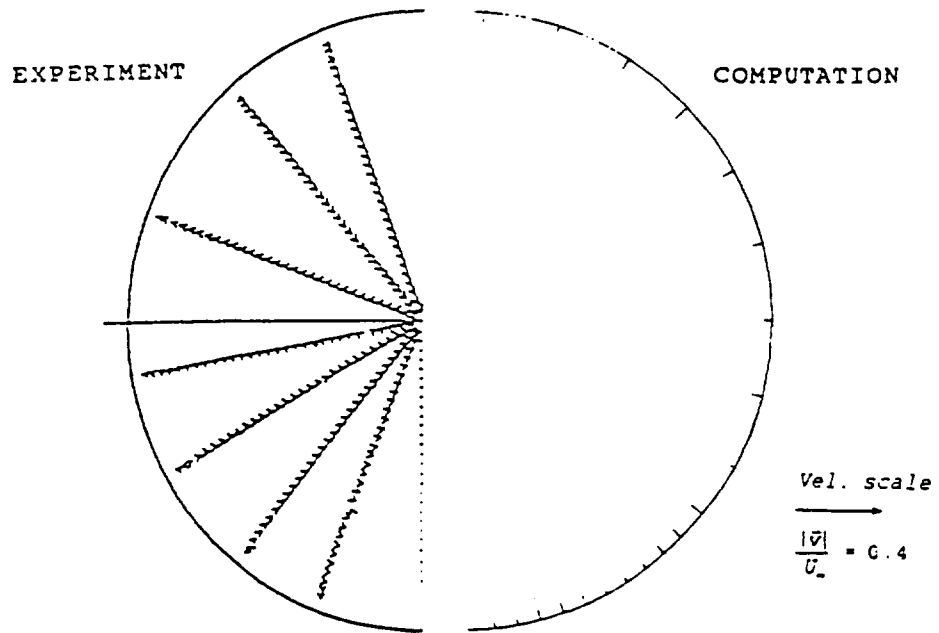


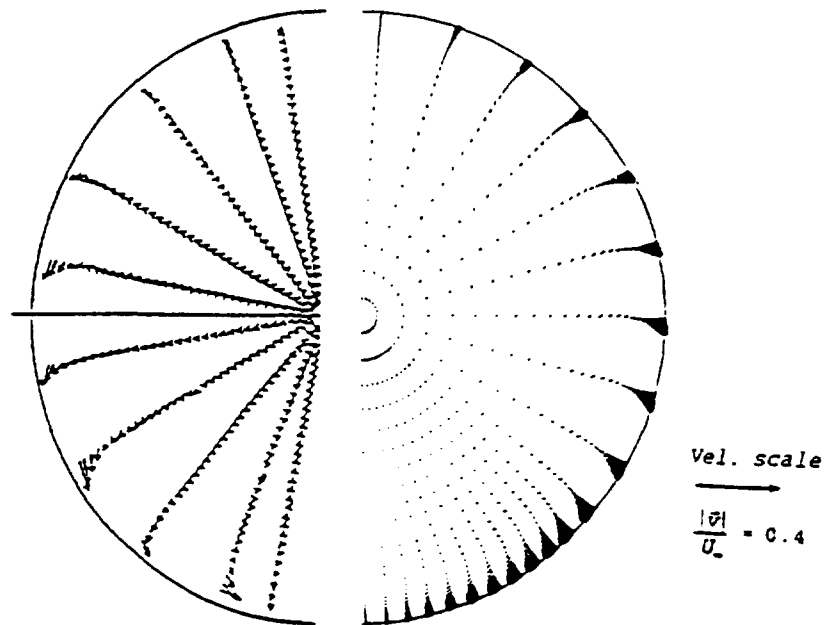
Fig. 4.8 Axial Mach number contours without vortex generators. At $S/D_i = 5.73$
($Ma = 0.6$, $Re_j = 1.76 \times 10^6$)

Exp. Wellborn et al. (1992)
($Ma = 0.6$, $Re_d = 2.6 \times 10^6$)

SECONDARY VELOCITY VECTORS
(Without Vortex Generators)



(a) at $S/D_i = -1.5$

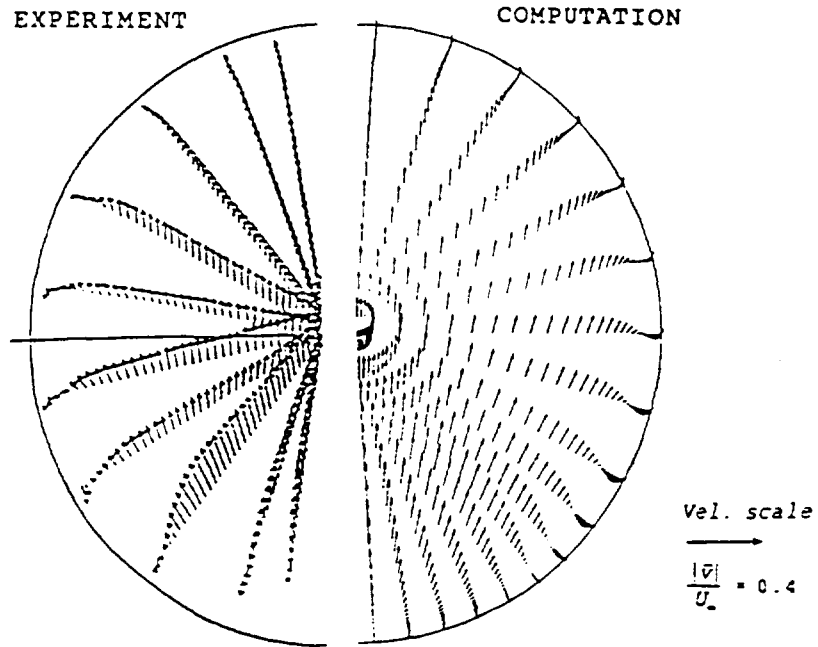
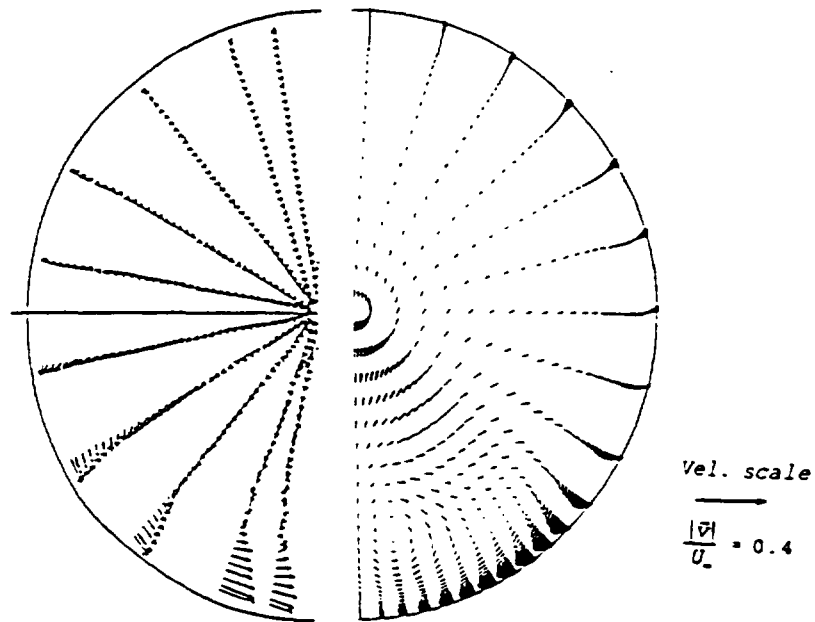


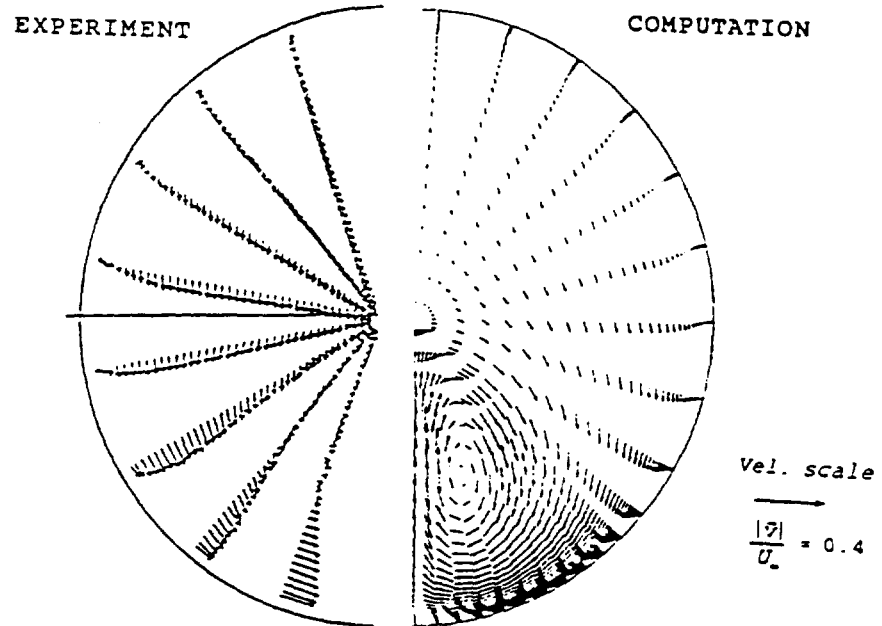
(b) at $S/D_i = 1.31$

Fig. 4.9 Secondary velocity profiles without vortex generators.

($Ma = 0.6$, $Re_d = 1.76 \times 10^6$)

Exp. Vakili et al.(1987)

(c) at $S/D_i = 2.62$ (d) at $S/D_i = 3.93$



(e) at $S/D_i = 5.24$

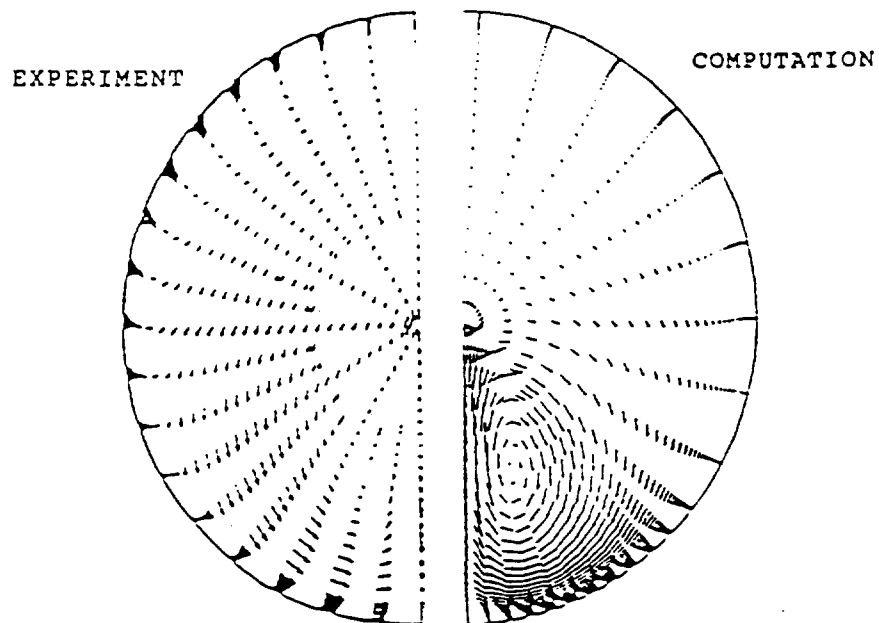


Fig. 4.10 Secondary velocity profiles without vortex generators. At $S/D_i = 5.73$
($Ma = 0.6$, $Re_d = 1.76 \times 10^6$)

Exp. Wellborn et al. (1992)
($Ma = 0.6$, $Re_d = 2.6 \times 10^6$)

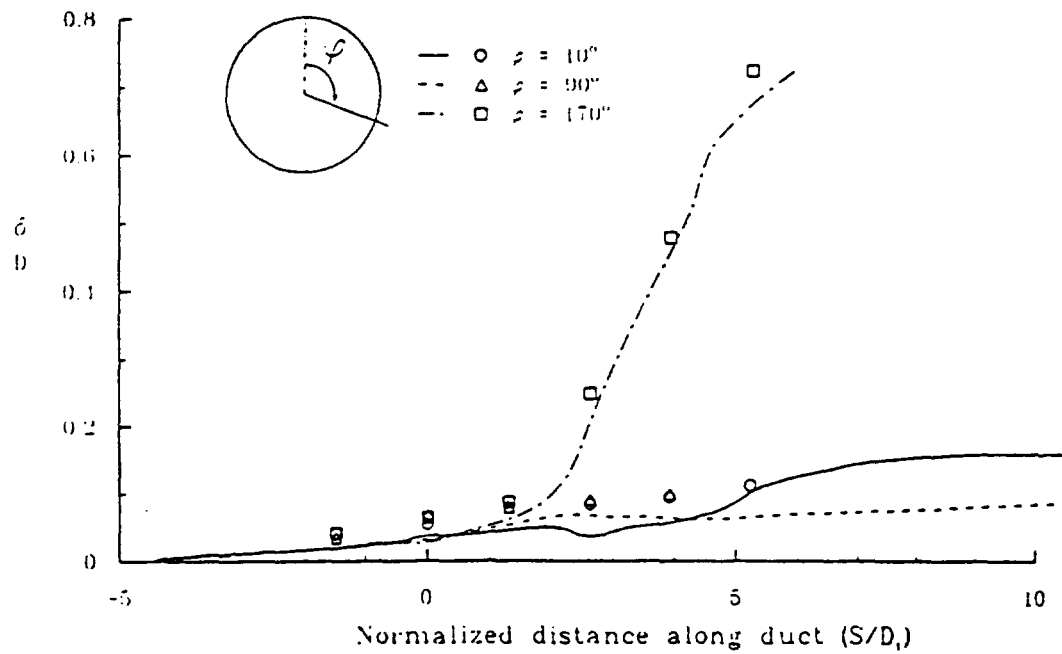


Fig. 4.11 Boundary layer thickness.
 ($Ma = 0.6$, $Re_d = 1.76 \times 10^6$)
 Exp. Vakili et al. (1987)

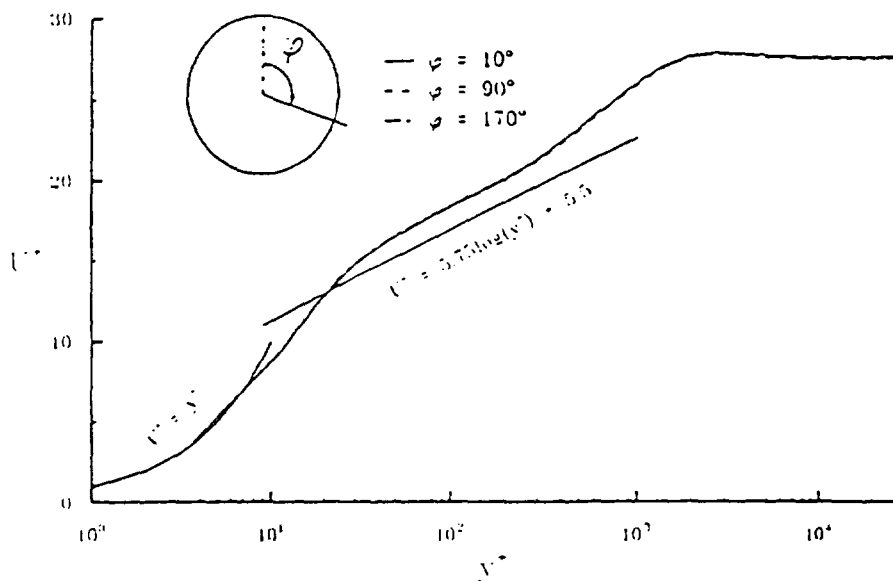


Fig. 4.12(a) Boundary layer wall coordinates plots at $S/D_i = -1.5$

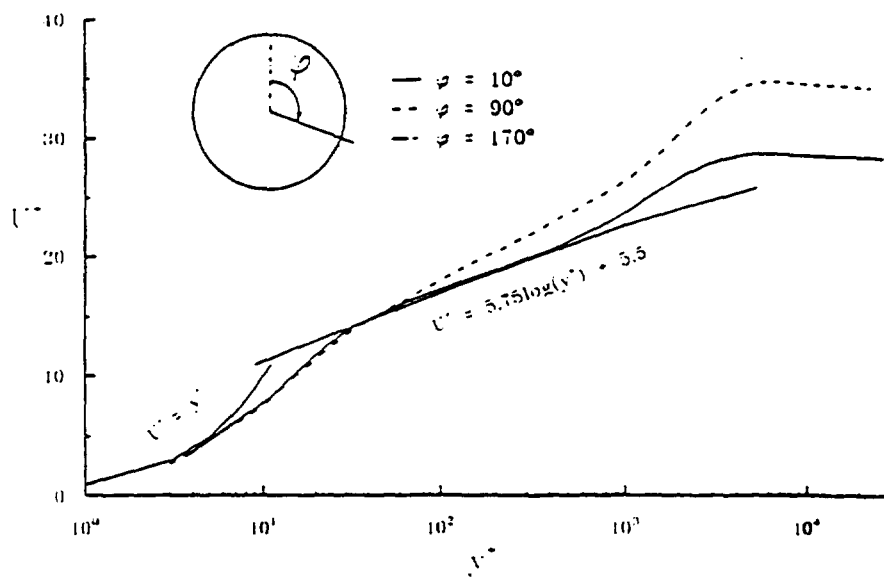


Fig. 4.12(b) Boundary layer wall coordinates plots at $S/D_i = 2.61$

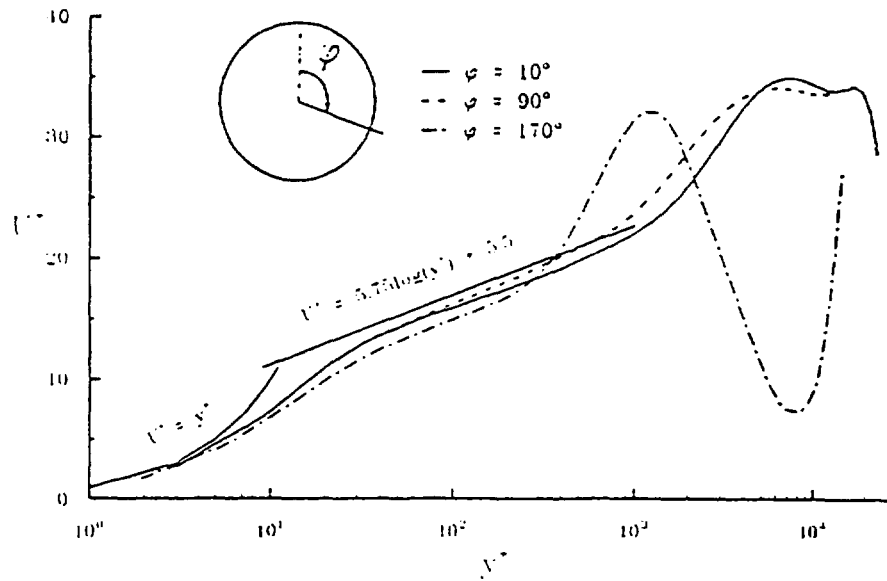


Fig. 4.12(c) Boundary layer wall coordinates plots at $S/D_i = 5.24$

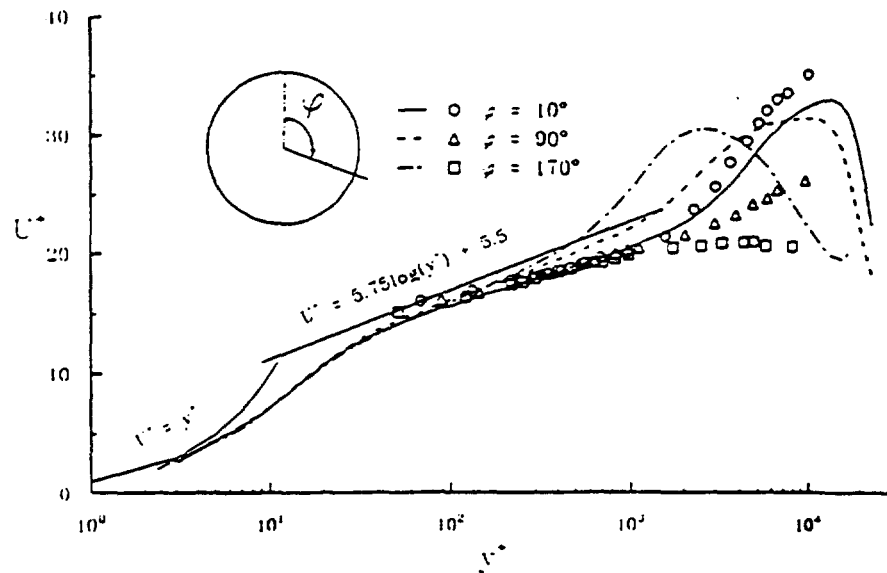


Fig. 4.12(d) Boundary layer wall coordinates plots at $S/D_i = 5.73$

Exp. Wellborn et al. (1992)
($Ma = 0.6$, $Re_d = 2.6 \times 10^6$)

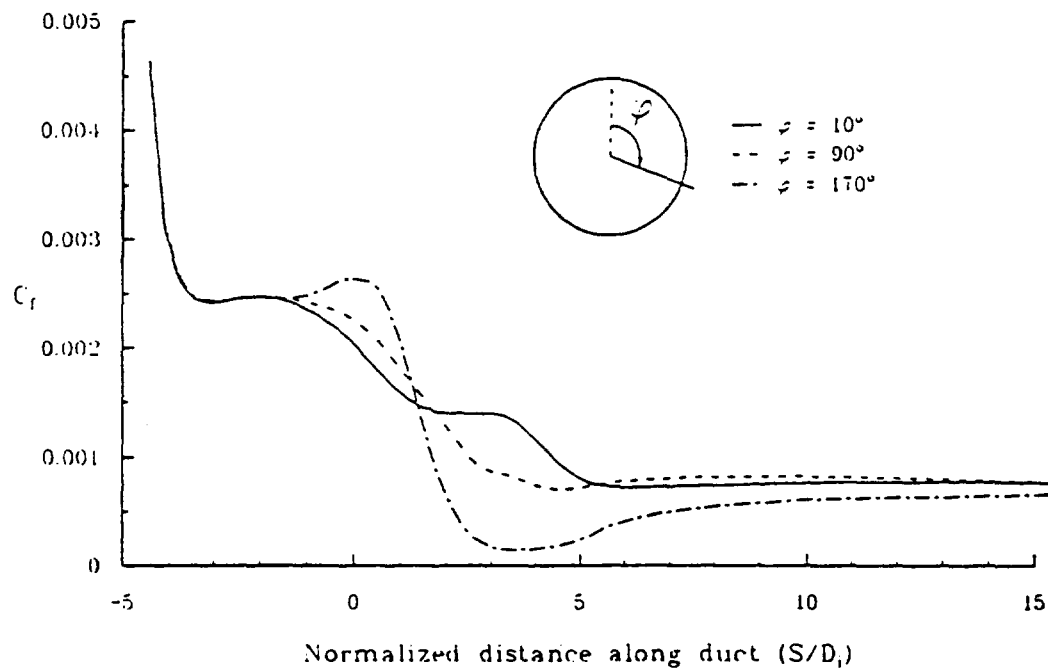


Fig. 4.13 Skin friction coefficient. ($C_f = \tau_{wall}/q_{ref}$)

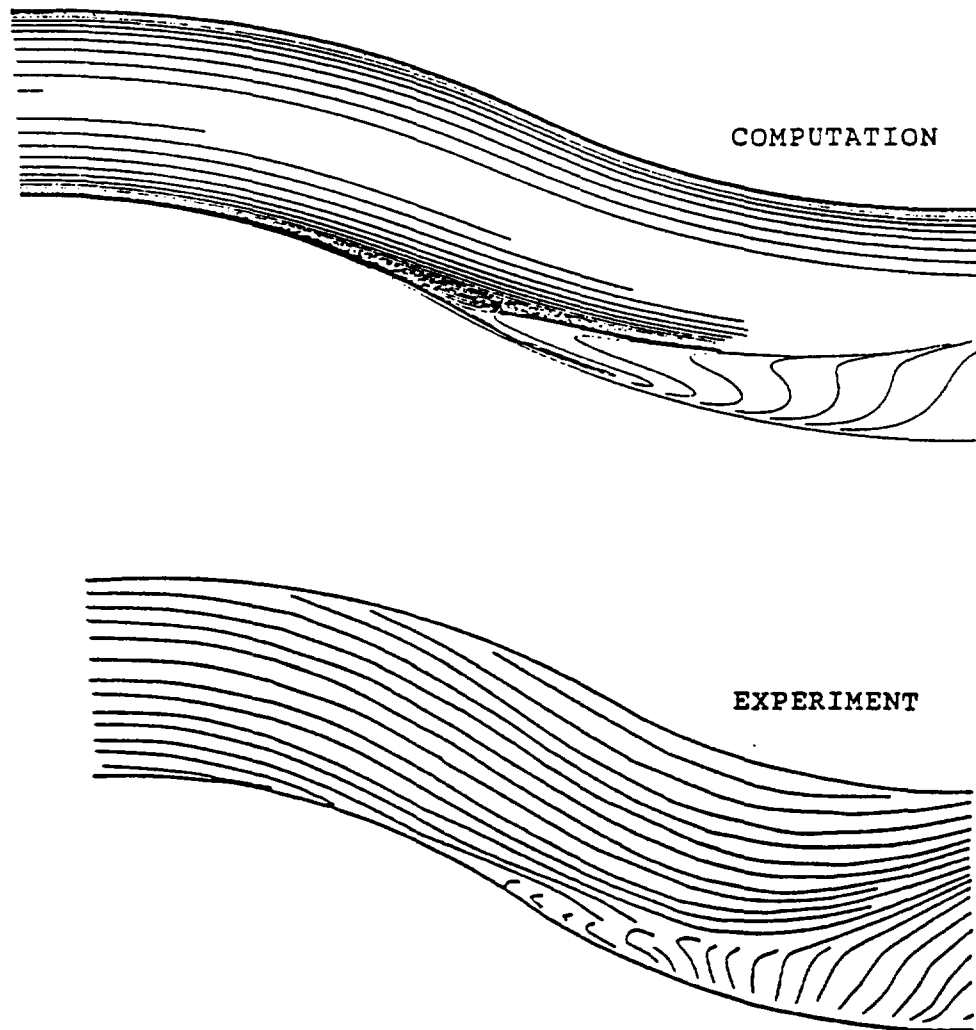


Fig. 4.14 Streamline along the S-duct centerline
($Ma = 0.6$, $Re_d = 1.76 \times 10^6$)

Exp. Wellborn et al. (1992)
($Ma = 0.6$, $Re_d = 2.6 \times 10^6$)

CHAPTER 5

STRAIGHT DUCT WITH VORTEX GENERATORS

The spiral longitudinal vortex interactions with turbulent boundary layer are numerically investigated in a cylindrical duct. The helical motion of the injected vortex is compared with the prediction by imagine vortex system and the prediction by Wendt et al.'s(1992) vortex interaction model. Two prediction models are derived in the Appendix B and C. In a second model, the constants which were derived from the experimental result of the external flow are employed. Although it is not sufficient to apply the same constants to predict the helical motion of the injected vortices in the internal flow, a reasonable prediction can be obtained in a short region just downstream of the vortex generators.

Kunik(1986) conducted a numerical study about the behavior of the injected vortex using the PNS equations on the straight duct. The flow was incompressible and the Reynolds number based on pipe diameter was 2000. The injected vortex was set up at the inlet of the computational region because the PNS equations could be solved by forward marching in space. Note that the PNS equations cannot consider the streamwise velocity deficit at the vortex core sufficiently because of neglecting the

streamwise diffusion term of the FNS equations.

In the present study, the injected vortices are set up within the computational region, and three-dimensional FNS equations are solved by the previous described numerical technique. Fig. 5.1 shows the computational grid for a cylindrical duct with $L/D = 20.0$. The polar grid topology consists of 47 radial points, 73 circumferential points and 60 streamwise nodal points. Exponential stretching is used to obtain a fine mesh near the wall. In order to obtain high quality velocity profile, the wall shear stresses are measured within the viscous sublayer. The first grid point nearest the wall has a y^+ value of less than 3, which is about 1.6×10^{-4} times the duct diameter. The location of vortex generator is at $X/D = 2.1$. The entrance Mach number is 0.6 and the Reynolds number based on the inlet diameter is 1.0×10^6 .

The number of iterations required to obtain a converged solution was approximately 25,000. Solutions were obtained on the Cray-YMP. The computational speed for the full duct was approximately 540 iterations per CPU hour. The residuals for these solutions were reduced by almost three orders of magnitude. The mass flow changes between the inlet and exit were within 1 percent.

5.1 Vortex Generator Model

The shed vortex from the vortex generator is modeled by providing the two-dimensional secondary flow structure in a crossplane. The secondary velocity structure is formulated as a viscous trailing vortex on the assumption of steady, incompressible, laminar and axisymmetric flow. The secondary velocity structure obtained with the above assumptions can be applied to the compressible and turbulent flow, because only one crossplane of the computational domain employs this vortical structure to simulate the shed vortex downstream of vortex generator.

The Navier-Stokes equations in cylindrical coordinates based on the origin of the trailing vortex in the infinite space are as follows:

$$\begin{aligned} \text{radial mom. eq.} \quad u_r \frac{\partial u_r}{\partial r} + u_x \frac{\partial u_r}{\partial x} - \frac{u_\theta^2}{r} = -\frac{1}{\rho} \frac{\partial p}{\partial r} \\ + \nu \left[\nabla^2 u_r - \frac{u_r}{r^2} \right] \end{aligned} \quad (5.1)$$

$$\begin{aligned} \text{rotational mom. eq.} \quad u_r \frac{\partial u_\theta}{\partial r} + u_x \frac{\partial u_\theta}{\partial x} + \frac{u_r u_\theta}{r} = \nu \left[\nabla^2 u_\theta - \frac{u_\theta}{r^2} \right] \end{aligned} \quad (5.2)$$

$$\text{axial mom. eq.} \quad u_r \frac{\partial u_x}{\partial r} + u_x \frac{\partial u_x}{\partial x} = -\frac{1}{\rho} \frac{\partial p}{\partial x} + \nu \nabla^2 u_x \quad (5.3)$$

$$\text{continuity eq.} \quad \frac{1}{r} \frac{\partial(r u_r)}{\partial r} + \frac{\partial u_x}{\partial x} = 0 \quad (5.4)$$

where

$$\nabla^2 \equiv \frac{\partial^2}{\partial r^2} + \frac{\partial}{r \partial r} + \frac{\partial^2}{\partial x^2} \quad (5.5)$$

These equations are linearized and solved by making the following assumptions:

- 1) The streamwise velocity deficit $u_d = U_\infty - u_x$ and the rotational velocity u_θ are small compared to the free-stream velocity U_∞ .
- 2) The radial velocity u_r is very small compared to U_∞ .
- 3) The Reynolds number of the main flow, $U_\infty x / \nu$, is large.

These assumptions reduce the above momentum and continuity Eqs. (5.1) - (5.4) to

$$\text{radial mom. eq.} \quad \frac{u_\theta^2}{r} = \frac{1}{\rho} \frac{\partial p}{\partial r} \quad (5.6)$$

$$\text{rotational mom. eq.} \quad U_\infty \frac{\partial u_\theta}{\partial x} = \nu \left[\frac{\partial^2 u_\theta}{\partial r^2} + \frac{1}{r} \frac{\partial u_\theta}{\partial r} - \frac{u_\theta}{r^2} \right] \quad (5.7)$$

$$\text{axial mom. eq. } U_{\infty} \frac{\partial u_d}{\partial x} = \nu \left[\frac{\partial u_d^2}{\partial r^2} + \frac{1}{r} \frac{\partial u_d}{\partial r} \right] \quad (5.8)$$

$$\text{continuity eq. } \frac{1}{r} \frac{\partial(r u_r)}{\partial r} - \frac{\partial u_d}{\partial x} = 0 \quad (5.9)$$

The boundary conditions to be satisfied by these linearized equations are:

$$x > 0, \quad u_{\theta} \rightarrow 0 \text{ and } u_d \rightarrow 0 \text{ as } r \rightarrow \infty$$

$$x \rightarrow \infty, \quad u_{\theta} \rightarrow 0 \text{ and } u_d \rightarrow 0 \text{ for all } r$$

$$x = 0, \quad u_{\theta} = \Gamma/2\pi r, \quad u_d = 0 \text{ except at the singular point } r = 0.$$

By the nature of the approximations, the vortex is examined at some distance downstream of its origin. Hence it is sufficient to assume that the vortex is suddenly generated at $x = 0$ as a free vortex of circulation Γ . Far downstream, the vortex finally decays until all the perturbation velocities u_r , u_{θ} and u_d are once again zero. Under these boundary conditions, the solutions of the reduced Eqs. (5.6) - (5.9) are as follows:

$$u_{\theta} = \frac{\Gamma}{2\pi r} \left[1 - \exp \left(-\frac{U_{\infty} r^2}{4\nu x} \right) \right] \quad (5.10)$$

$$u_r = -\frac{Ar}{2x^2} \exp \left(-\frac{U_{\infty} r^2}{4\nu x} \right) \quad (5.11)$$

$$u_d = \frac{A}{x} \exp \left(-\frac{U_{\infty} r^2}{4\nu x} \right) \quad (5.12)$$

The integration constant A can be found from equating the change of momentum of the flow in the entire wake flow to the drag on the vortex generator;

$$A = \frac{D_0}{4\pi\rho\nu} \quad (5.13)$$

where D_0 is the profile drag of the vortex generator.

Rotational velocity Eq. (5.10) and radial velocity Eq. (5.11) can be used to set up the vortical flow in the cross plane. However, comparing the magnitude of these velocities with the assumptions that a small section of NACA 0012 wing is used as a vortex generator with a proper angle of attack and the length x from the origin of vortex to the cross plane for vortical structure is $O(1)$, the radial velocity is small compared with the rotational velocity.

$$\begin{aligned} \frac{u_{\theta}}{u_r} &= \frac{\frac{\Gamma}{2\pi r} \left[1 - \exp \left(-\frac{U_{\infty} r^2}{4\nu x} \right) \right]}{-\frac{Ar}{2x^2} \exp \left(-\frac{U_{\infty} r^2}{4\nu x} \right)} \\ &= -\frac{\Gamma\rho x U_{\infty}}{D_0} \left[1 + \frac{1}{2!} \left(\frac{U_{\infty} r^2}{4\nu x} \right) + \frac{1}{3!} \left(\frac{U_{\infty} r^2}{4\nu x} \right)^2 + \dots \right] \end{aligned}$$

$$= -\frac{C_L}{C_d} \left[1 + \frac{1}{2!} \left(\frac{U_\infty r^2}{4\nu x} \right) + \frac{1}{3!} \left(\frac{U_\infty r^2}{4\nu x} \right)^2 + \dots \right] = O(10^2) \quad (5.14)$$

Only the rotational velocity is used to make the vortical structure in a crossplane.

$$u_\theta = \frac{\Gamma}{2\pi r} \left[1 - \exp \left(-\frac{U_\infty r^2}{4\nu x} \right) \right] \quad (5.10)$$

If we apply the vortical structure of Eq. (5.10), which is formulated as one fully rolled up trailing vortex, to the circular duct directly, normal velocity component exists on the duct wall. In order to consider the shed vortex created from the vortex generator mounted within the circular duct, we can employ the image vortex because of a very small vortex core just downstream of vortex generator. The image vortex of equal strength as the inviscid flow is located outside the duct using Milne-Thomson's circle theorem(1968). The superposed vortical flow within the duct has no normal velocity component at the wall. The tangential velocity component approaches zero at the wall by reducing the magnitude of the superposed vortical flow inside the boundary layer by the one-seventh power velocity distribution law. These adjusted vortical velocities are introduced at every point in the crossplane.

In order to consider the streamwise velocity deficit

$(u_d = U_\infty - u_r)$ in that crossplane, the flow passing the vortex generators is assumed as the steady-state steady-flow process. The temperature and stagnation enthalpy at the crossplane are calculated by averaging these values in the upstream-plane and downstream-plane of the crossplane for vortical structure. Even though the streamlines between two crossplanes are not the same as the streamwise direction due to the vortical flow, this approximation is sufficient if the vortical flow is small compared with the axial flow or the distance between two planes is small compared with the duct diameter. The stagnation enthalpy obtained by this approximation are uniform at every local grid points of the crossplane because of the streamwise velocity deficit in the downstream-plane for vortical structure. From this stagnation enthalpy at the local grid point, we can obtain the deficit of streamwise velocities in the crossplane with the calculated vortical velocities and temperatures.

5.2 Results and Discussion

In order to examine the usefulness of the vortex generator model and to investigate the effect of the different type vortex generators in a straight duct, four

different cases are tested: (1) single embedded vortex, (2) counter-rotating vortices of the same strength that rotate toward each other, (3) counter-rotating vortices of the same strength that rotate away from each other, and (4) co-rotating vortices, one vortex having double the strength of the other.

number	Γ/DU_∞	φ	$\lambda = r/R$
(1)	0.062	0°	0.831
(2)	-0.062, +0.062	$-18^\circ, 18^\circ$	0.831
(3)	+0.062, -0.062	$-27^\circ, 27^\circ$	0.831
(4)	-0.062, -0.031	$-27^\circ, 27^\circ$	0.831

Table 5.1 The strength and location of the embedded vortices (Γ is positive when the vortex rotates counter-clockwise, and φ is the circumferential angle from the vertical plane on the lower wall)

The boundary layer thickness at the axial location of the vortex generator ($x/D = 2.1$) is 0.06 times the duct radius. The vortex generator is at a height of 0.16 times the duct radius. Therefore, the vortex generator tip is located well outside of the boundary layer.

Figs. 5.2 - 5.4 show the computational results when a

single vortex is embedded in a crossplane within the duct. The total-pressure contours and secondary velocity profiles at the several different streamwise locations are shown in Fig. 5.2 and Fig. 5.3, respectively. Fig. 5.2(a) and Fig. 5.3(a) are the total-pressure contours and secondary velocity profiles at the location of the vortex generator ($x/D = 2.1$). The location of the shed vortex along the downstream is shown in Fig 5.4. It is compared with the predicted location by the image vortex and the vortex interaction system.

The total-pressure contours in Fig. 5.2 show that the boundary layer thickness in the region of downflow is decreased because the induced secondary flow pushes the high energy flow toward the wall. Adversely, the boundary layer thickness in the region of upflow is increased by the induced secondary flow. It shows that the appropriate vortex generators can control the main flow.

The secondary velocity profiles in Fig. 5.3 show that the strength of the vortex decays in the downstream direction due to viscous diffusion. The streamwise vortex trajectory shows a helical character which is predicted by the inviscid theory. This characteristic is clearly shown in Fig. 5.4.

Fig. 5.4(a) shows that the injected vortex moves radially inward. It shows significant deviation between the

computational result and simplified vortex interaction model. Even though the prediction model using the image vortex considers a mechanism which the injected vortex moves radially inward, it is very weak because the vortex moves radially inward after then the vortex core reaches the wall. The predicted locations obtained by two simplified prediction models are the same along the streamwise direction, as shown in Fig. 5.4(a).

Physically, the boundary layer growth on the duct wall retards the growth of the vortex core to the wall, but the vortex core grows without blockage to the center of the duct. This causes a transverse pressure gradient which is not symmetric with respect to the vortex center. The pressure gradient between the vortex center and the duct wall is steeper than that between the vortex center and the center of the duct as shown in Fig. 5.2. The vortex moves radially inward as a result of this nonsymmetric pressure gradient.

The location of the vortex along the circumferential direction is in agreement with the location predicted by the simplified model in the short region just downstream of the location of vortex generator as shown in Fig. 5.4(b). The deviation between the model location and computed results increases with increasing downstream distance. Even though the vortex interaction model considers the decay of

vortex strength by the wall effect, this model does not adequately consider the mechanism by which the vortex moves radially inward. At the same strength of vortex, if the vortex moves radially inward 10% from the original location, the induced velocity by the image vortex is reduced around 16% at the vortex core. The induced velocities overestimated by the simple models overpredict the azimuthal location of the vortex as it moves downstream.

Fig. 5.5 shows the progression of the counter-rotating vortices of the same strength that rotate toward each other as they march down the duct. The left hand side and right hand side of Fig. 5.5 are the total-pressure contours and the secondary velocity profiles, respectively. Fig. 5.5(f) shows that the boundary layer thickness in the lower wall of the duct is one third of that in the upper wall of the duct at the station VI ($x/D = 16.10$). It shows that the main flow can be controlled by adjusting the number of vortex generators, strength and location of vortex, etc.,.

The behavior of the vortices as they move downstream is qualitatively similar to the behavior predicted by the inviscid theory. Two vortices move away from each other, and also move radially inward as shown in Fig. 5.6(a). The deviation between the computational results and the predictions of the two simple models is due to the weak

mechanism of radial flow behavior in the simple models as mentioned in case of the single embedded vortex.

The secondary velocities, induced by the counter-rotating vortices rotating toward each other, force the high energy flows into each other. Therefore, the pressure gradient with respect to the vortex axis in the case of counter-rotating vortices rotating toward each other is more symmetric than that of the single embedded vortex, whose larger induced velocities near the wall are associated with steeper pressure gradient near the wall. Comparing Figs. 5.4 and 5.6, one sees that the rate of radially inward motion when counter-rotating vortices are embedded as shown in Fig. 5.6 is approximately 7% lower than that when the single vortex is embedded as shown in Fig. 5.4. However, the rate of circumferential movement of counter-rotating vortices is lower than that of the single embedded vortex, even though the radial location of counter-rotating vortices is closer to the wall than that of the single embedded vortex. This is consistent because the secondary velocity induced by counter vortex acts oppositely to the direction which is induced on the vortex core by image vortex.

Fig. 5.7 shows the progression of the counter-rotating vortices of the same strength that rotate away from each other as they march down the duct. The left hand side and

right hand side of Fig. 5.7 are the total-pressure contours and the secondary velocity profiles, respectively. Fig. 5.7(f) shows that the boundary layer thickness at the lower wall of the duct is much greater than that at the upper wall of the duct. This is a contrary result compared with the case of the counter-rotating vortices of the same strength that rotate toward each other.

The streamwise trajectories of vortices exhibit the same behavior as that predicted by the inviscid theory. The vortices attract each other in a short region downstream of after the vortex generators, and then they proceed to march away from the wall. As the two vortices move closer to each other, the pressure gradient between the vortex center and the duct wall is increased, but the pressure gradient between the vortex center and the center of the duct is decreased. Downstream of station IV ($x/D = 8.20$), the pressure gradient between the vortex center and the symmetric line of two vortices is steeper than that between the vortex center and the duct wall as shown in Fig. 5.8. It means that the two vortices move away from each other during the time they proceed to march away from the wall as shown in Fig. 5.7.

Fig. 5.7 shows that the predicted vortex location by two models is overpredicted except in a short region downstream of the vortex generators. This deviation occurs

from the weak mechanism of the two simplified models as previously mentioned. Two prediction models do not have a mechanism which each vortex tries to settle at a stable location, i.e., vortex moves to the position of radially symmetric pressure gradient.

Fig. 5.10 shows the total-pressure contours along the duct when the co-rotating vortices are embedded; the secondary velocity profiles are shown in Fig 5.11. The strength of vortex(A) is twice the strength of vortex(B). As the vortices march down the duct, the circumferential movement of vortex(A) is faster than that of vortex(B) because of its large induced velocity on the vortex core. This is anticipated by the inviscid theory. The vortex(B) is collapsed into the vortex(A) at some distance as shown in Fig. 5.11 because two vortices have the same direction of vorticity.

Figs. 5.12 and 5.13 are the locations of vortex(A) and vortex(B) along the duct, respectively. They agree well with the results by the prediction models in a short region just after vortex generators. The deviation between the computational results and the prediction by two models occurs from the weak mechanism of the two prediction models as previously mentioned.

The satisfactory results of the computation in the straight duct with vortex generators suggest that the

vortex model employed in this work can be applied to solve the full three-dimensional Navier-Stokes equations. The internal flow can be controlled by an appropriate adjustment of the location, strength, lateral spacing, and number of vortex generators. The computational results agree well with the results of the prediction models in a short region just after the location of the vortex generators, even though we adopted the same constants which were derived from the experimental results on the external flow. For the better prediction of vortices along downstream in the internal flow, an experiment in the duct with vortex generators is necessary to find the correct constants.

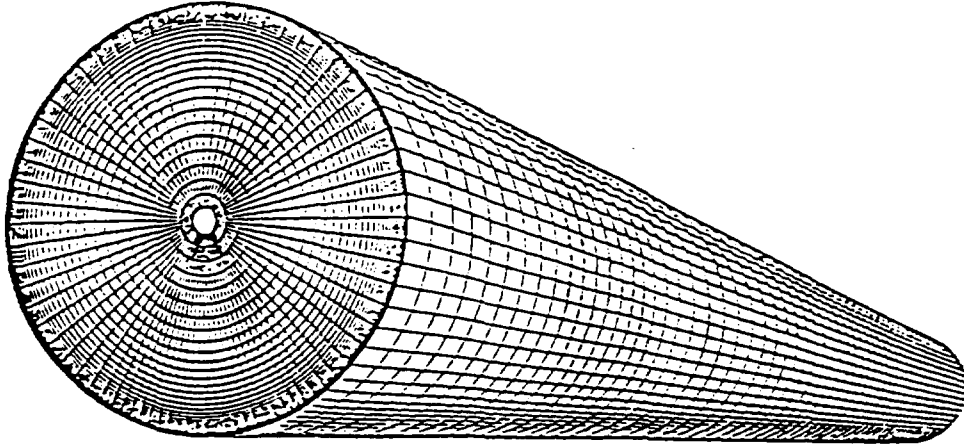


Fig. 5.1(a) Computational grid for the vortex interaction studies within a cylindrical duct, $L/D = 20.0$

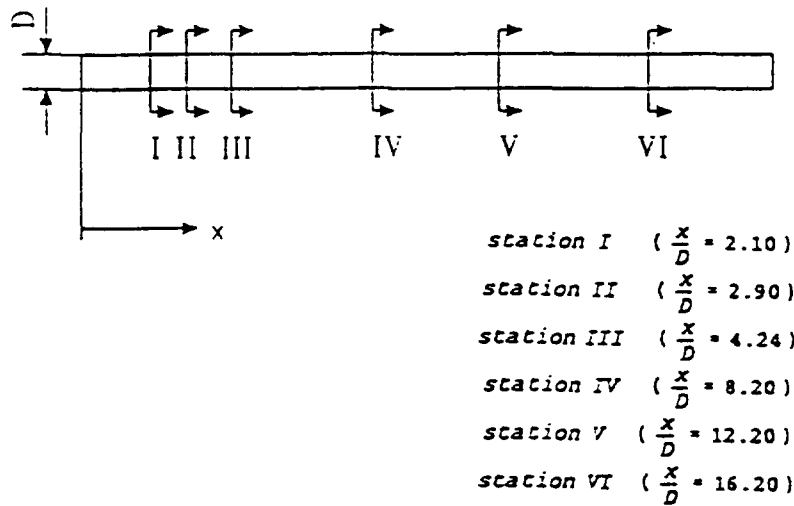
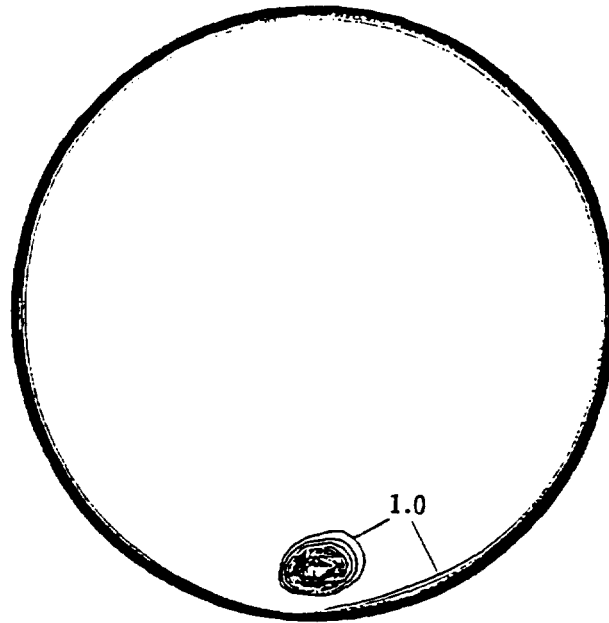


Fig. 5.1(b) Measurement stations along the circular straight duct.

TOTAL PRESSURE COEFFICIENT CONTOURS
(Single vortex embedded)



contour decrement = 0.05

vortex core location:

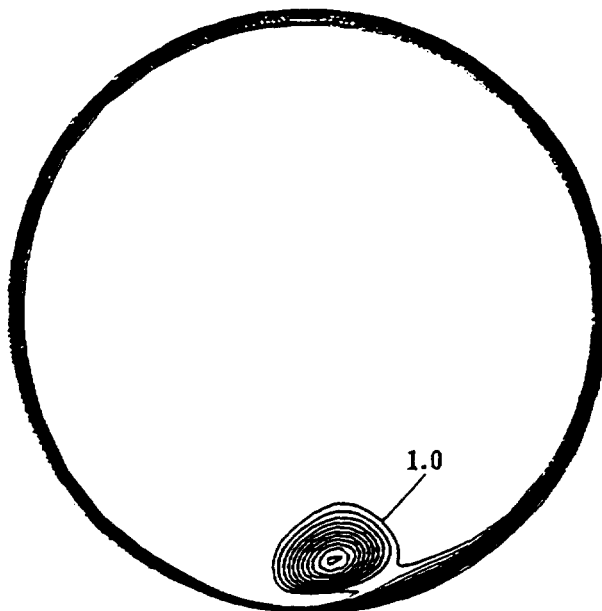
$$\lambda = \frac{r}{R} = 0.831$$

$$\varphi = 0^\circ$$

strength of vortex:

$$\frac{\Gamma}{DU_\infty} = 0.062$$

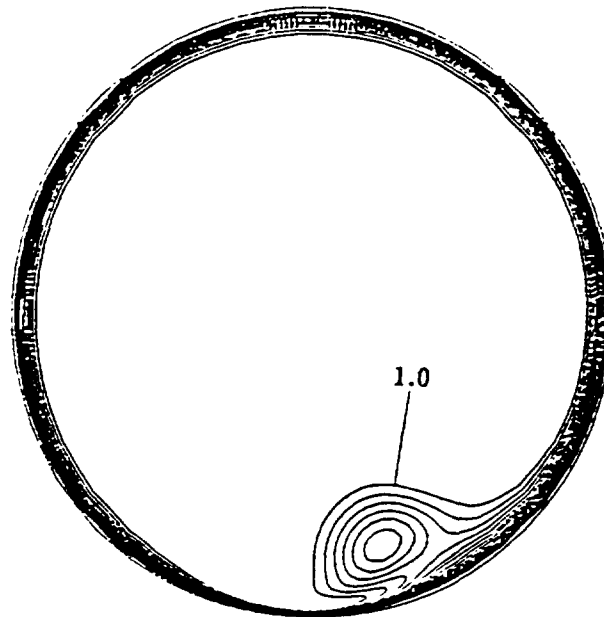
(a) station I ($x/D = 2.10$)



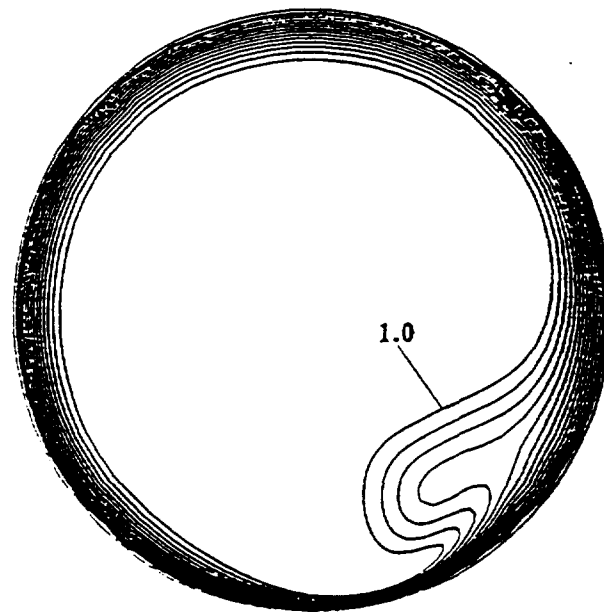
(b) station II ($x/D = 2.90$)

Fig. 5.2 Total-pressure coefficient contours of the single embedded vortex.

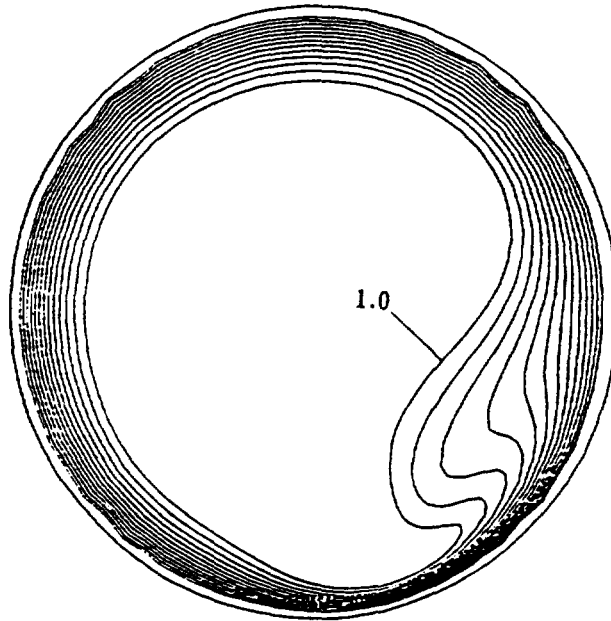
($Ma = 0.6$, $Re_\delta = 1.0 \times 10^6$)



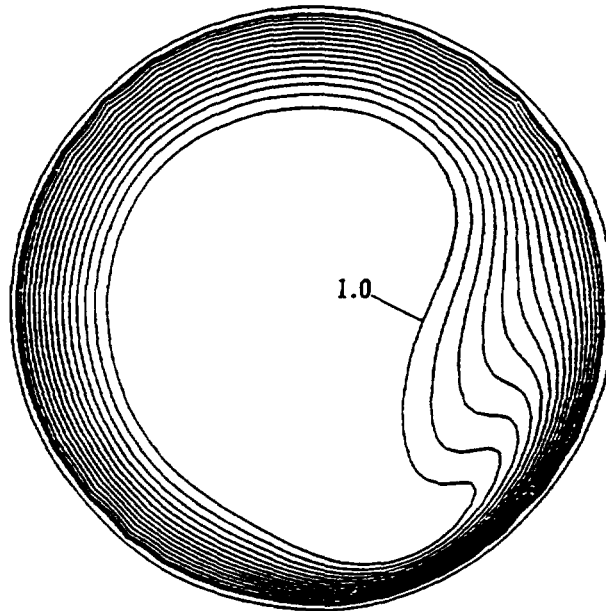
(c) station III ($x/D = 4.24$)



(d) station IV ($x/D = 8.20$)

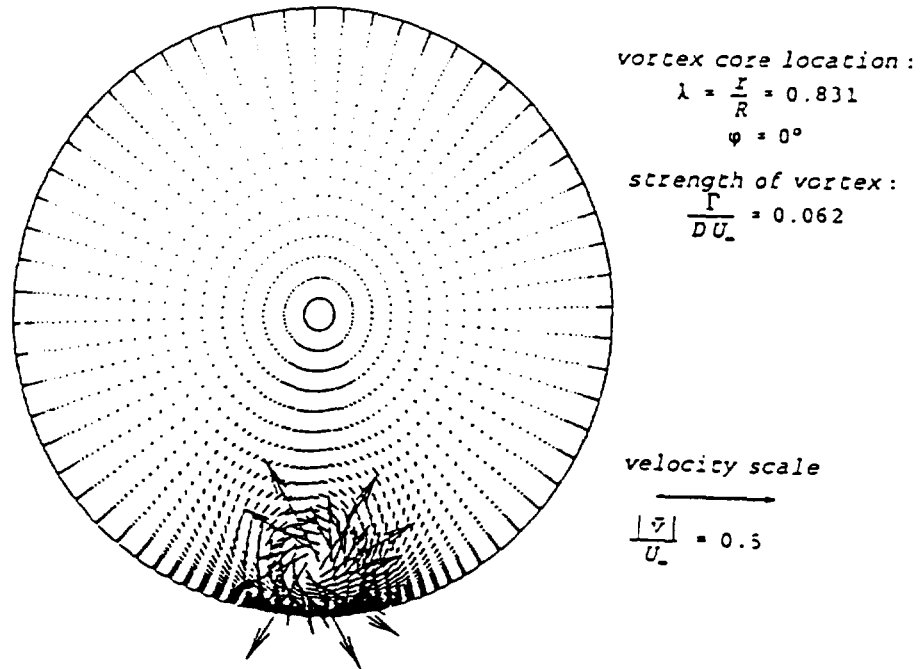


(e) station V ($x/D = 12.20$)

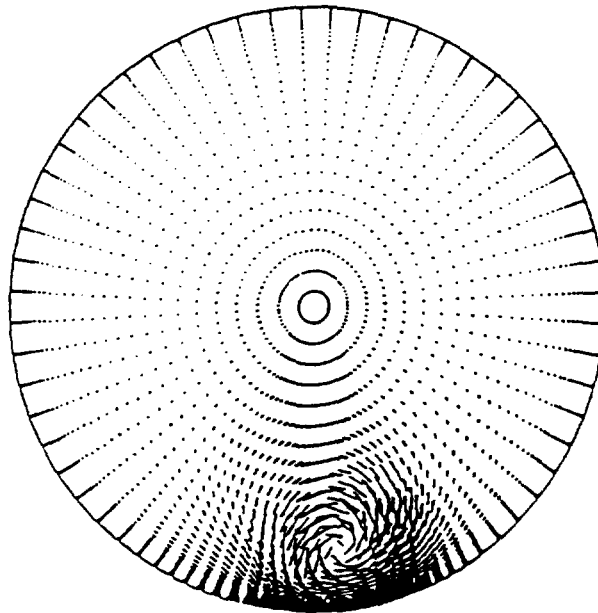


(f) station VI ($x/D = 16.20$)

SECONDARY VELOCITY VECTORS
(Single vortex embedded)

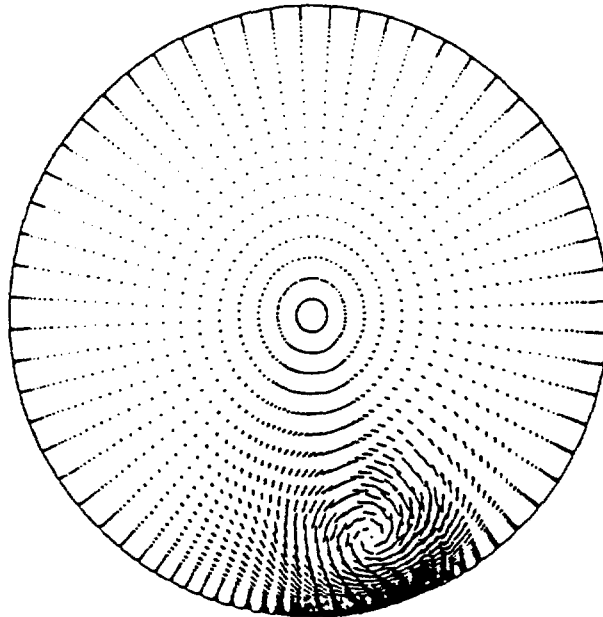


(a) station I ($x/D = 2.10$)

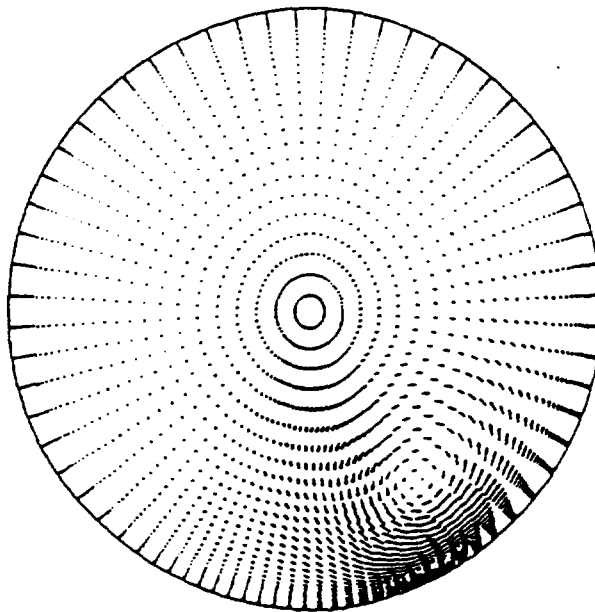


(b) station II ($x/D = 2.90$)

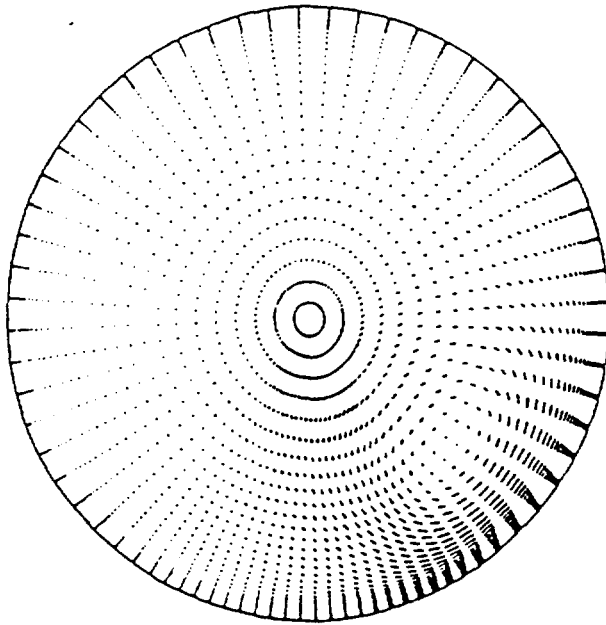
Fig. 5.3 Secondary velocity profiles of the single embedded vortex.
 ($Ma = 0.6$, $Re_d = 1.0 \times 10^6$)



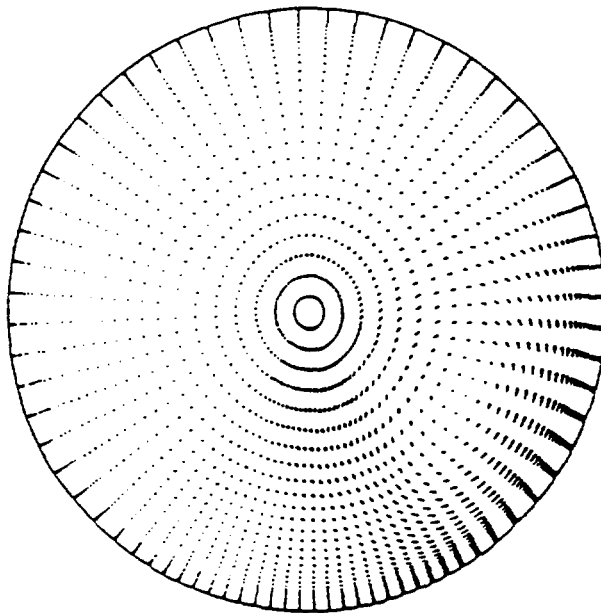
(c) station III ($x/D = 4.24$)



(d) station IV ($x/D = 8.20$)



(e) station V ($x/D = 12.20$)



(f) station VI ($x/D = 16.20$)

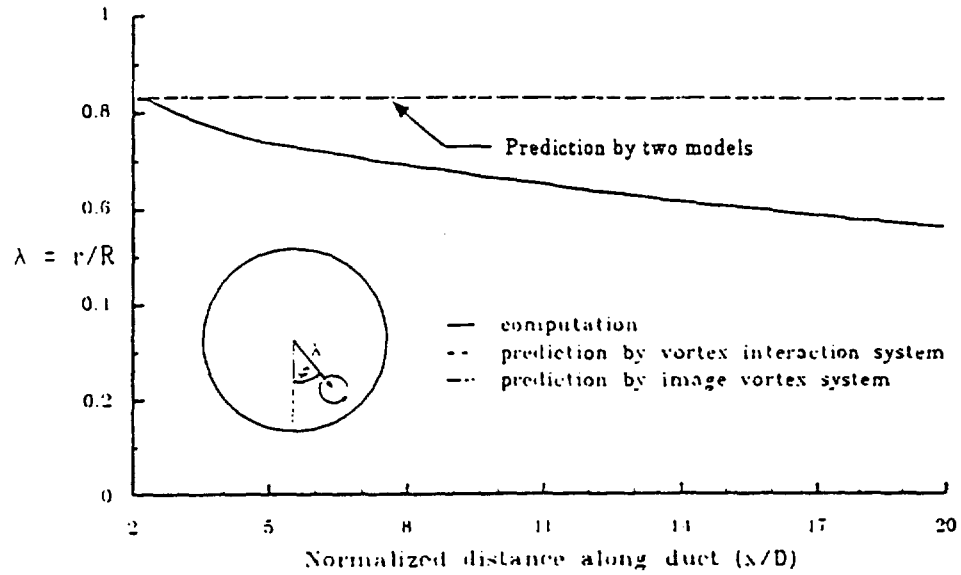


Fig. 5.4(a) Radial trajectory of the single embedded vortex.

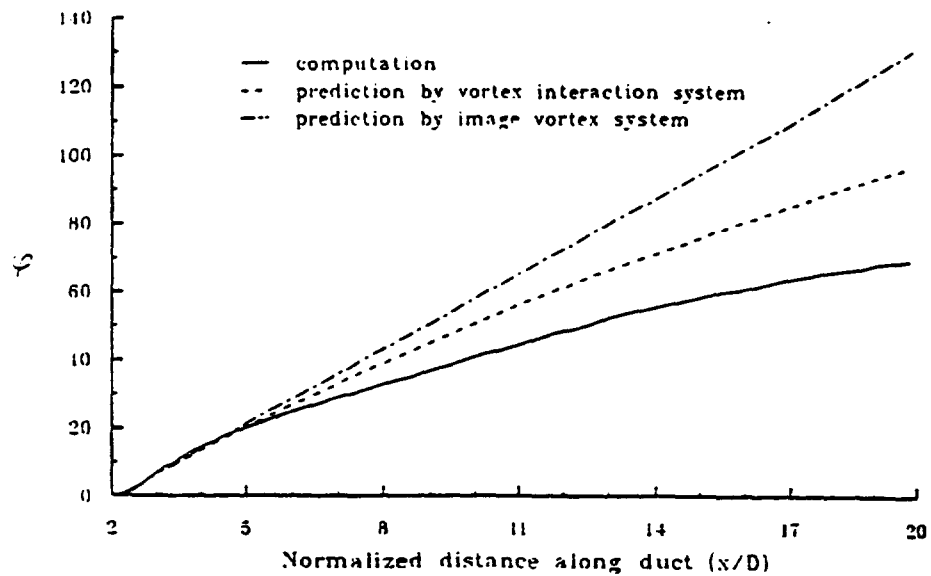


Fig. 5.4(b) Angular trajectory of the single embedded vortex.

COUNTER-ROTATING VORTICES (Downflow pairs)

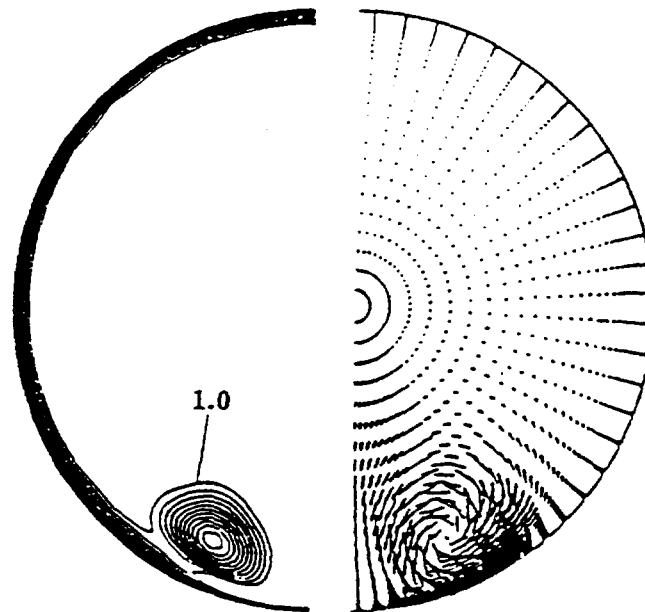
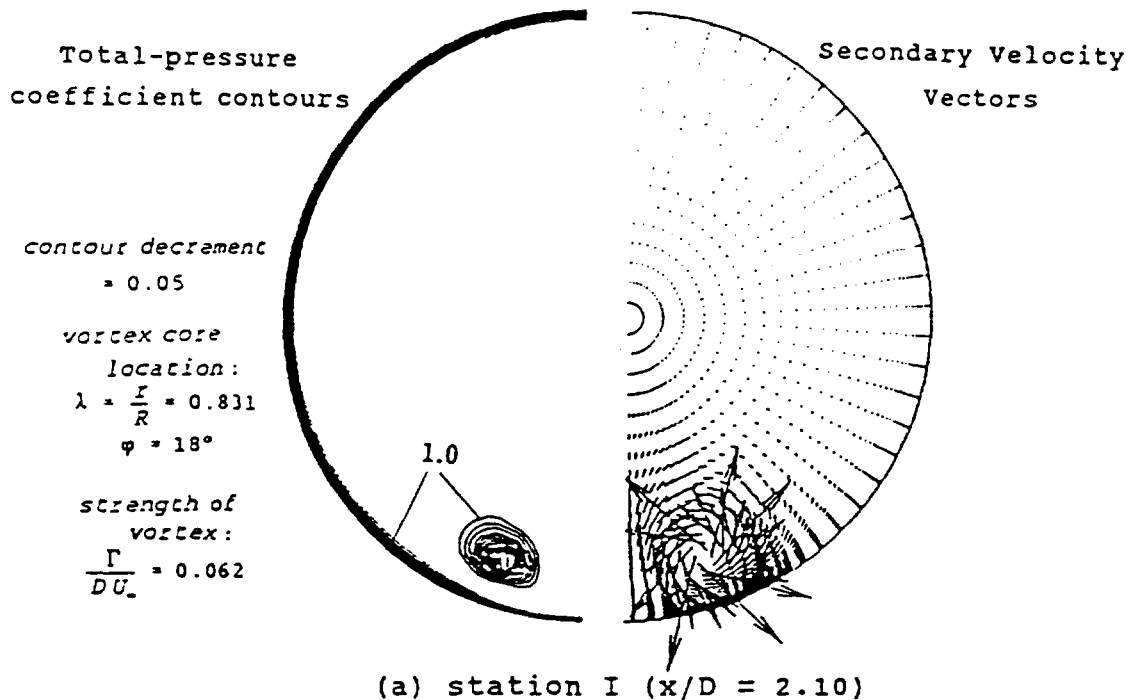
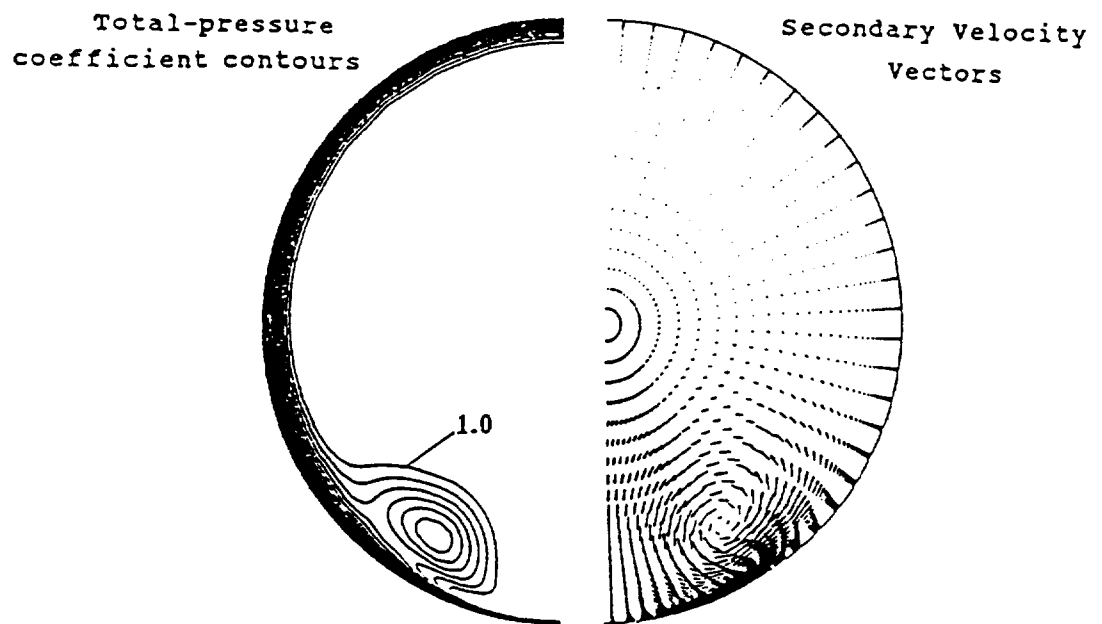
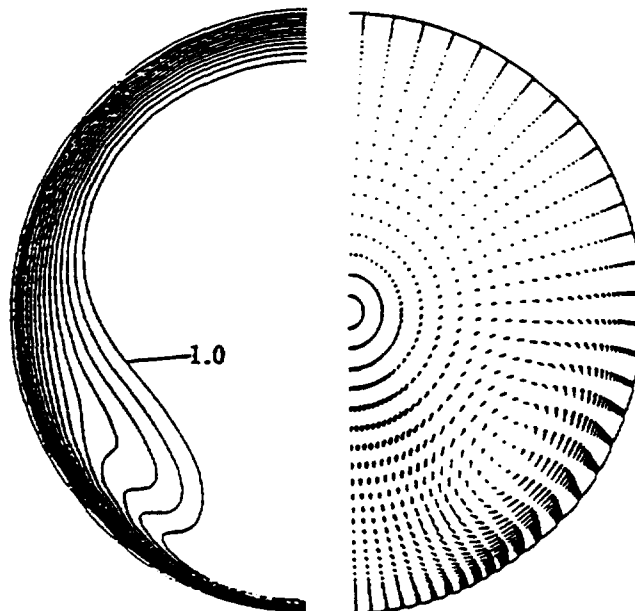
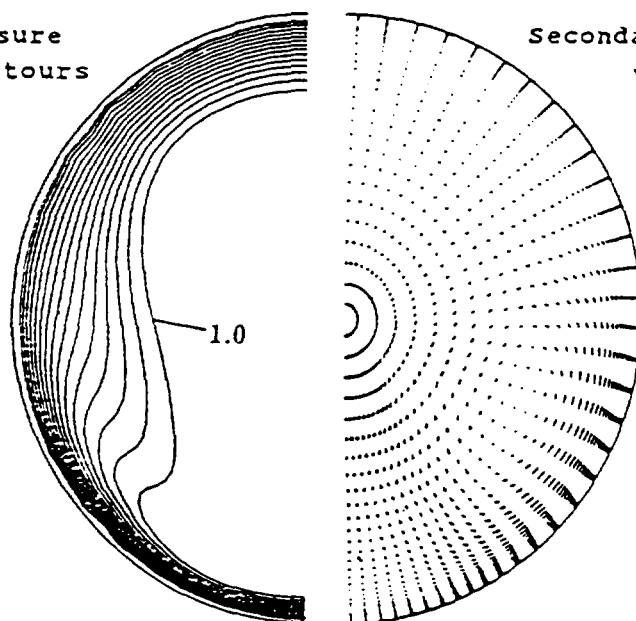


Fig. 5.5 Total-pressure coefficient contours and secondary velocity profiles of the counter rotating vortices of the same strength that rotate toward each other.
($Ma = 0.6$, $Re_d = 1.0 \times 10^6$)

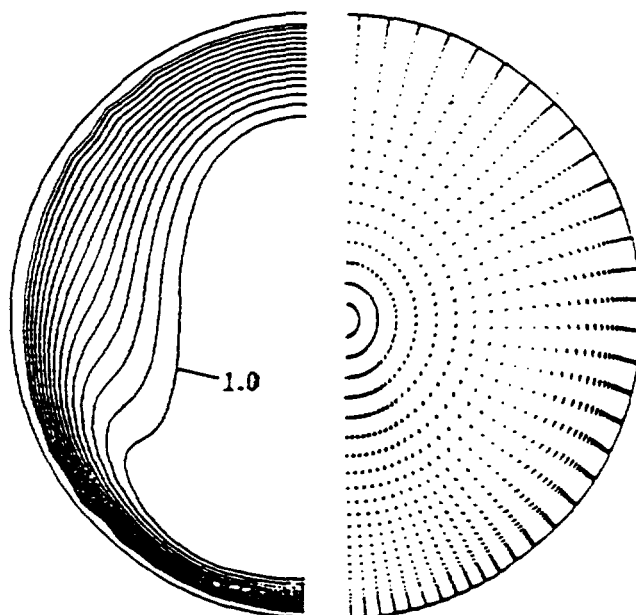
(c) station III ($x/D = 4.24$)(d) station IV ($x/D = 8.20$)

Total-pressure
coefficient contours

Secondary Velocity
Vectors



(e) station V ($x/D = 12.20$)



(f) station VI ($x/D = 16.20$)

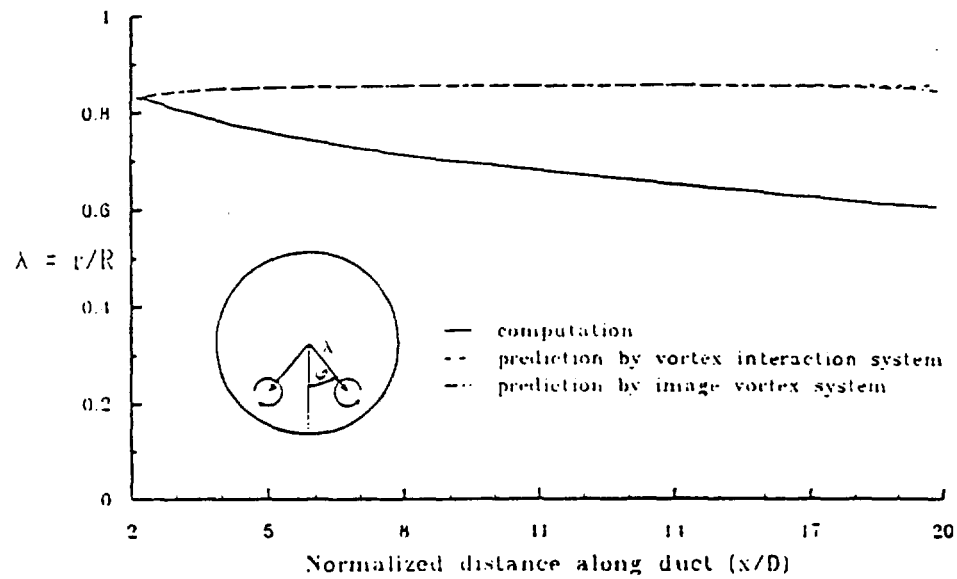


Fig. 5.6(a) Radial trajectory of the counter rotating vortices of the same strength that rotate toward each other.

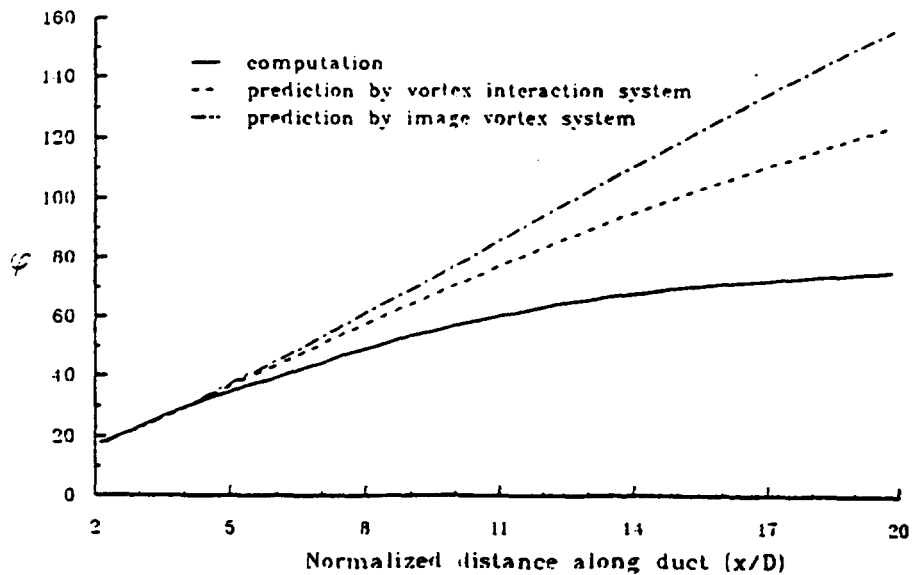


Fig. 5.6(b) Angular trajectory of the counter rotating vortices of the same strength that rotate toward each other.

COUNTER-ROTATING VORTICES
(Upflow pairs)

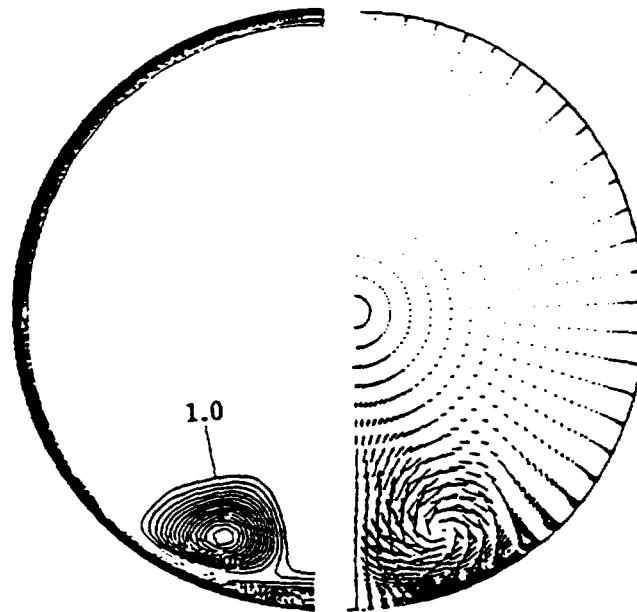
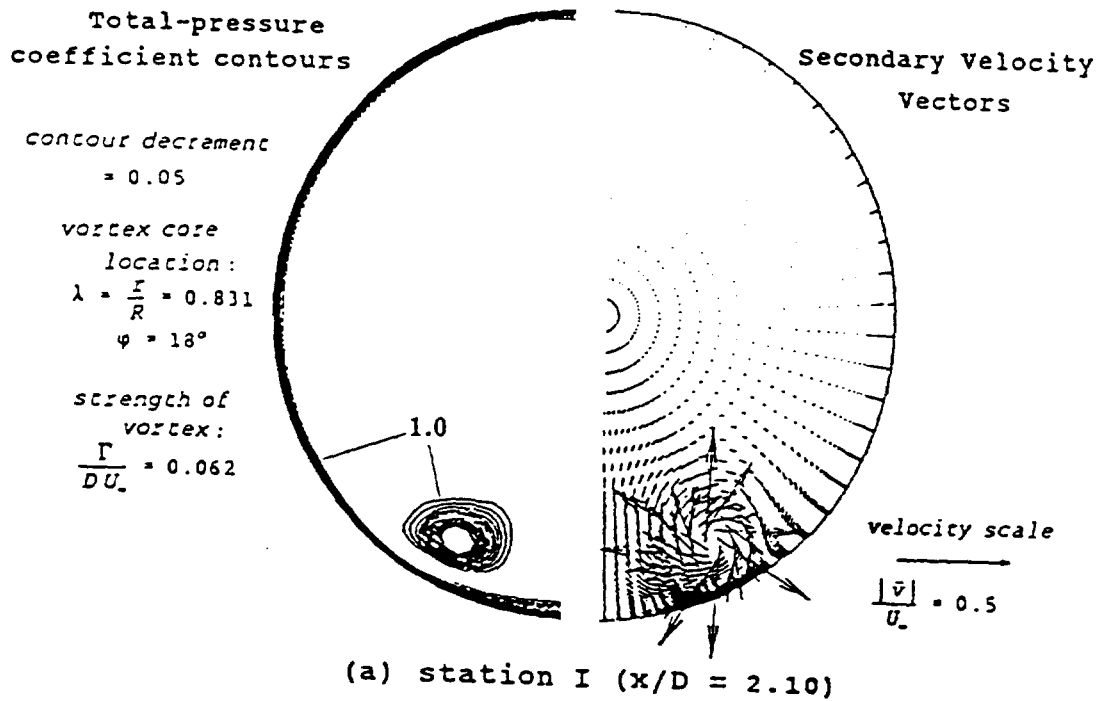
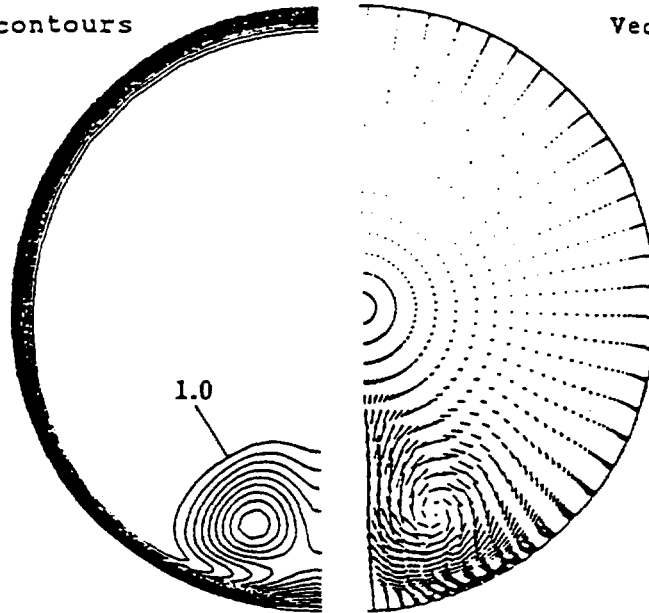


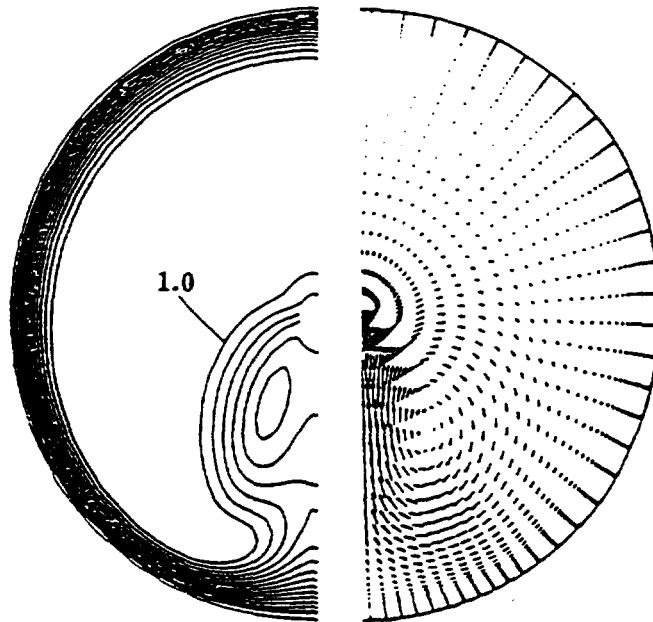
Fig. 5.7 Total-pressure coefficient contours and secondary velocity profiles of the counter-rotating vortices of the same strength that rotate away from each other.
($Ma = 0.6$, $Re_d = 1.0 \times 10^6$)

Total-pressure
coefficient contours

Secondary Velocity
Vectors



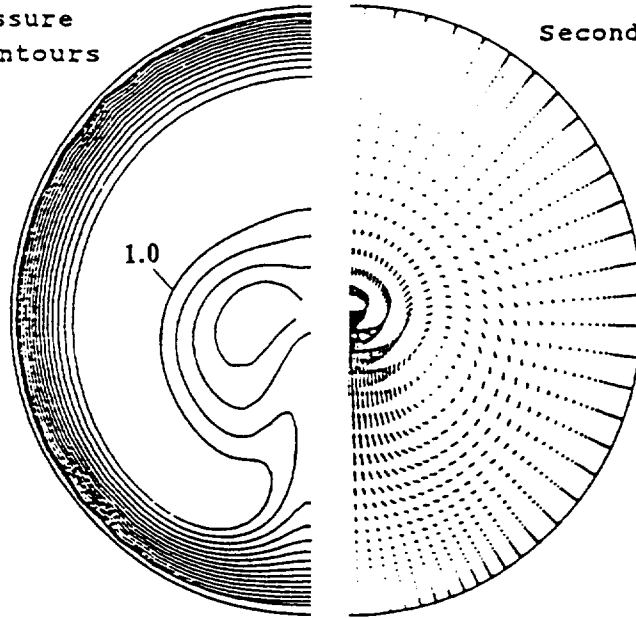
(c) station III ($x/D = 4.24$)



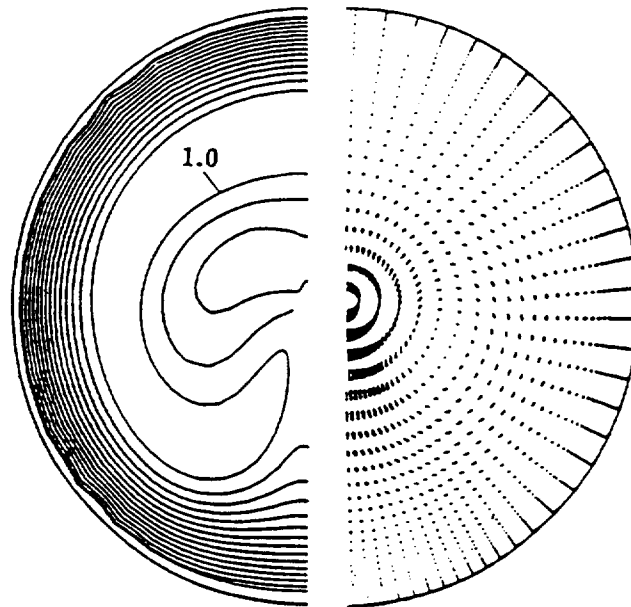
(d) station IV ($x/D = 8.20$)

Total-pressure
coefficient contours

Secondary Velocity
Vectors

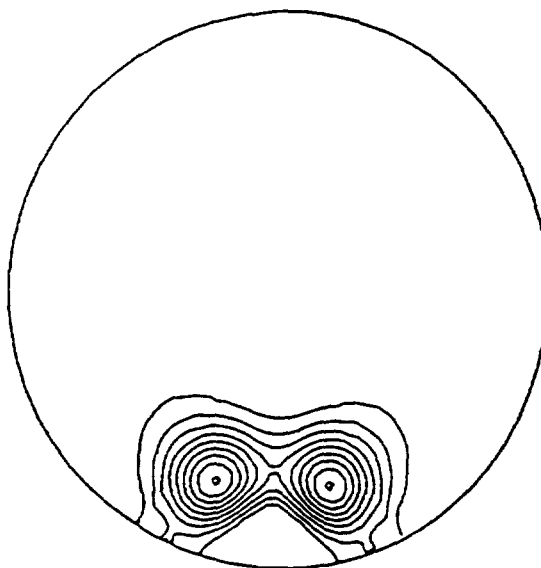


(e) station V ($x/D = 12.20$)



(f) station VI ($x/D = 16.20$)

STATIC PRESSURE COEFFICIENT CONTOURS
(Upflow pairs)



vortex core location :

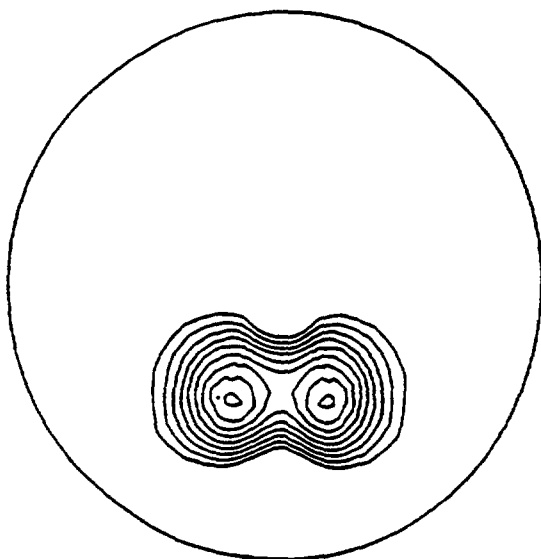
$$\lambda = \frac{r}{R} = 0.831$$

$$\varphi = 27^\circ$$

strength of vortex :

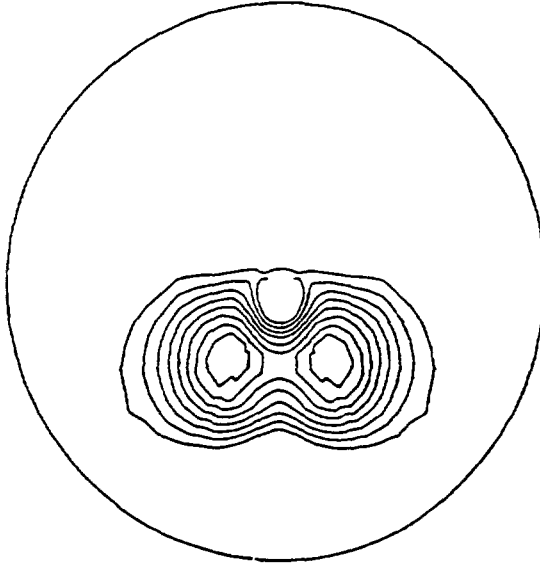
$$\frac{\Gamma}{DU_\infty} = 0.062$$

(a) station III ($x/D = 4.24$)

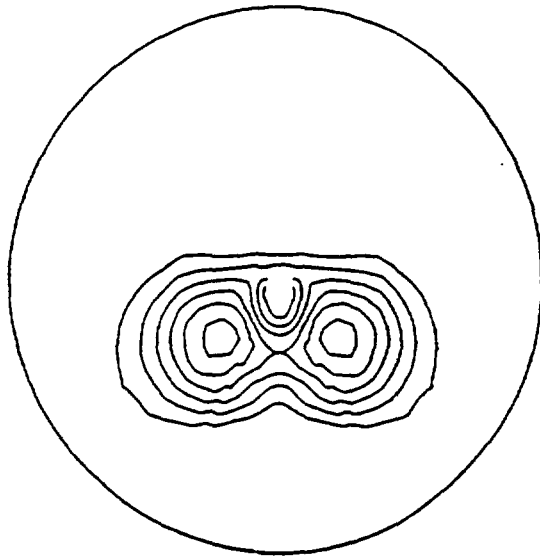


(b) station IV ($x/D = 8.20$)

Fig. 5.8 Static-pressure coefficient contours of the counter-rotating vortices of the same strength that rotate away from each other.
($Ma = 0.6$, $Re_d = 1.0 \times 10^6$)



(c) at $(x/D = 10.20)$



(d) station V $(x/D = 12.20)$

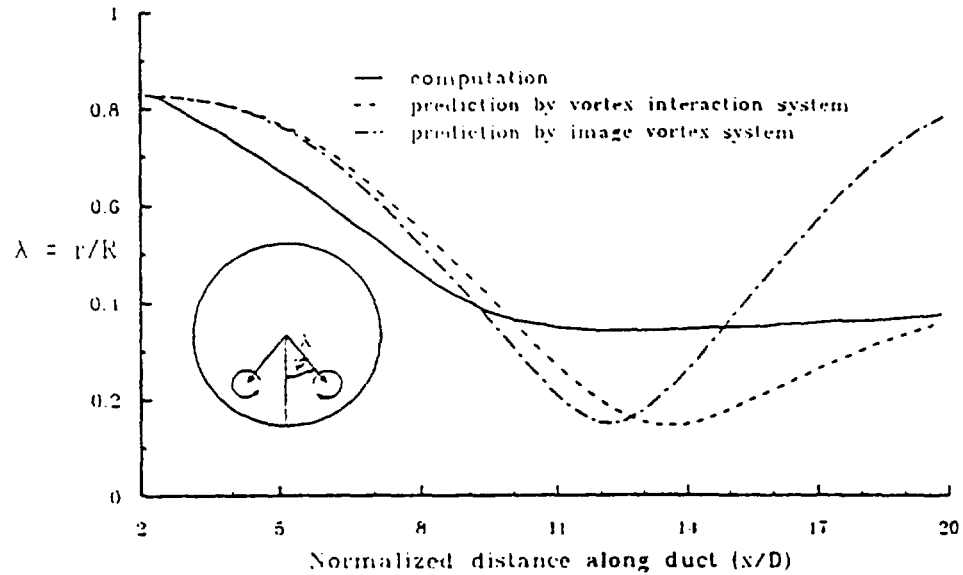


Fig. 5.9(a) Radial trajectory of the counter-rotating vortices of the same strength that rotate away from each other.

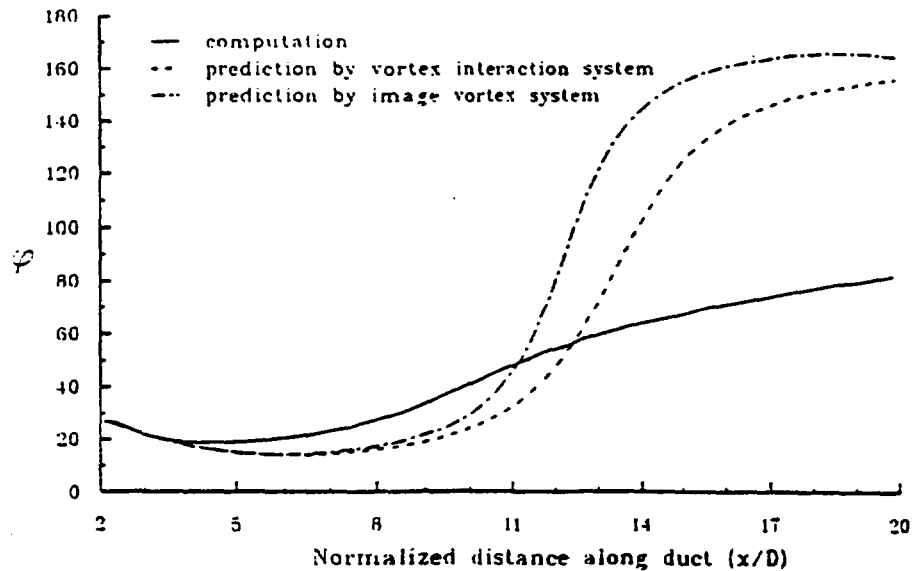
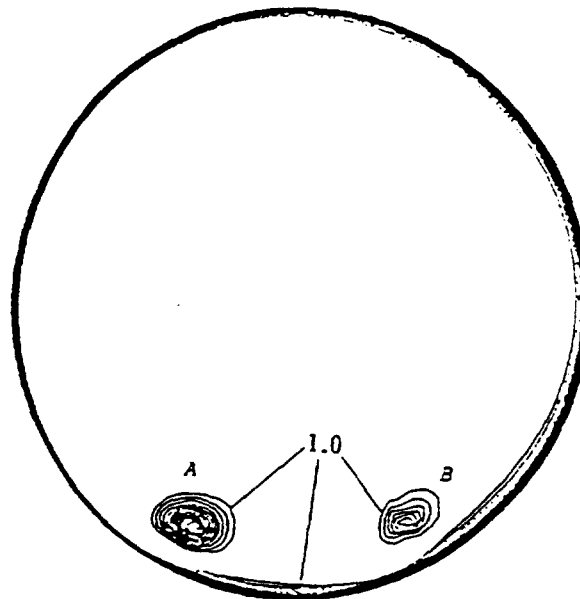


Fig. 5.9(b) Angular trajectory of the counter-rotating vortices of the same strength that rotate away from each other.

TOTAL PRESSURE COEFFICIENT CONTOURS
(Co-rotating vortices)



contour decrement = 0.05

vortex (A) core location:

$$\lambda = \frac{r}{R} = 0.831$$

$$\varphi = -27^\circ$$

strength of vortex (A) :

$$\frac{\Gamma}{DU_\infty} = 0.062$$

vortex (B) core location:

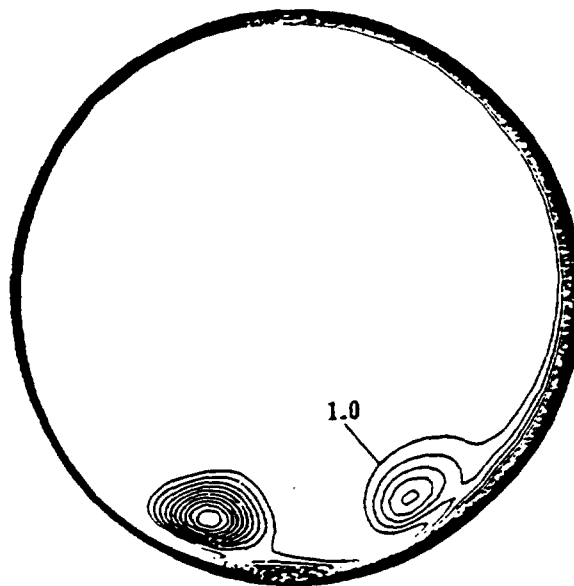
$$\lambda = \frac{r}{R} = 0.831$$

$$\varphi = 27^\circ$$

strength of vortex (B) :

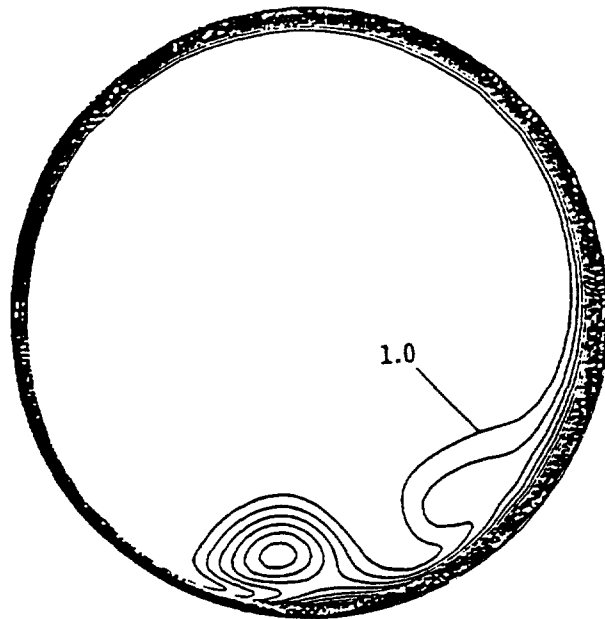
$$\frac{\Gamma}{DU_\infty} = 0.031$$

(a) station I ($x/D = 2.10$)

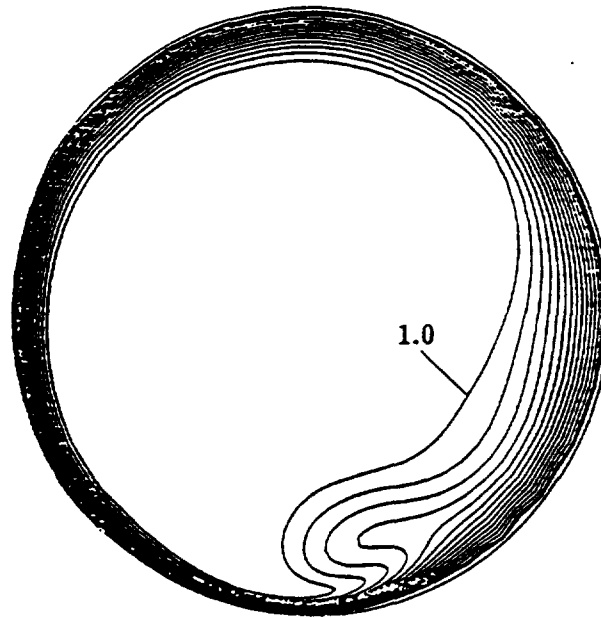


(b) station II ($x/D = 2.90$)

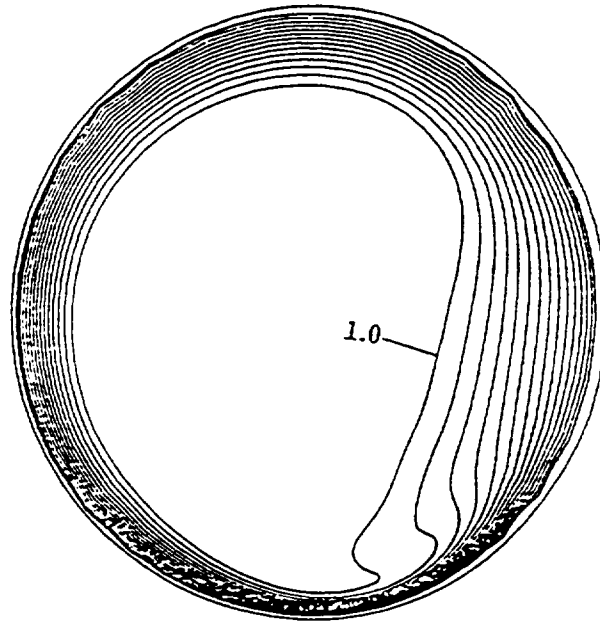
Fig. 5.10 Total-pressure coefficient contours when the co-rotating vortices are embedded. Vortex (A) has double the strength of vortex (B).
($Ma = 0.6$, $Re_d = 1.0 \times 10^6$)



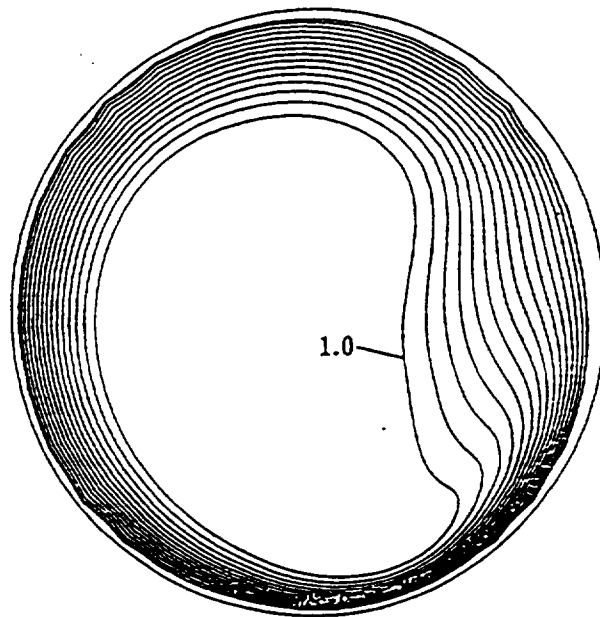
(c) station III ($x/D = 4.24$)



(d) station IV ($x/D = 8.20$)

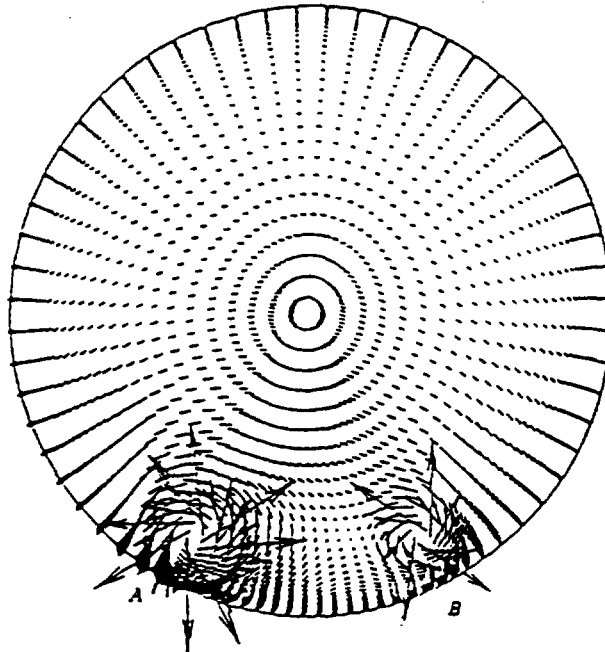


(e) station V ($x/D = 12.20$)



(f) station VI ($x/D = 16.20$)

SECONDARY VELOCITY VECTORS
(Co-rotating vortices)



(a) station I ($x/D = 2.10$)

vortex (A) core location:

$$\lambda = \frac{r}{R} = 0.831$$

$$\varphi = -27^\circ$$

strength of vortex (A) :

$$\frac{\Gamma}{DU_\infty} = 0.062$$

vortex (B) core location:

$$\lambda = \frac{r}{R} = 0.831$$

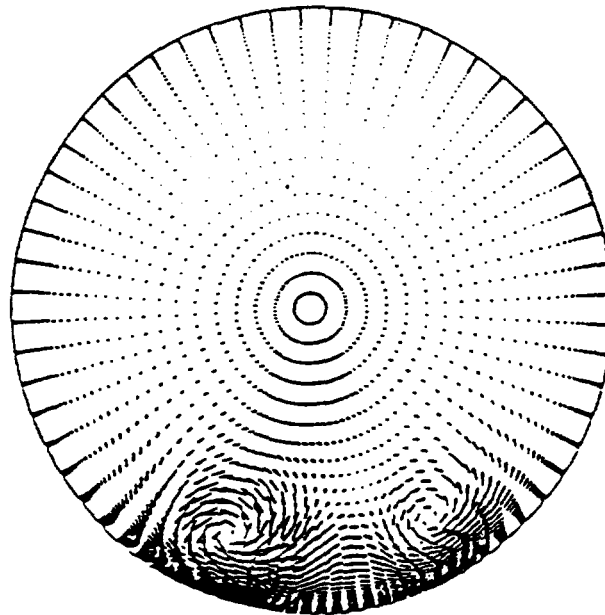
$$\varphi = 27^\circ$$

strength of vortex (B) :

$$\frac{\Gamma}{DU_\infty} = 0.031$$

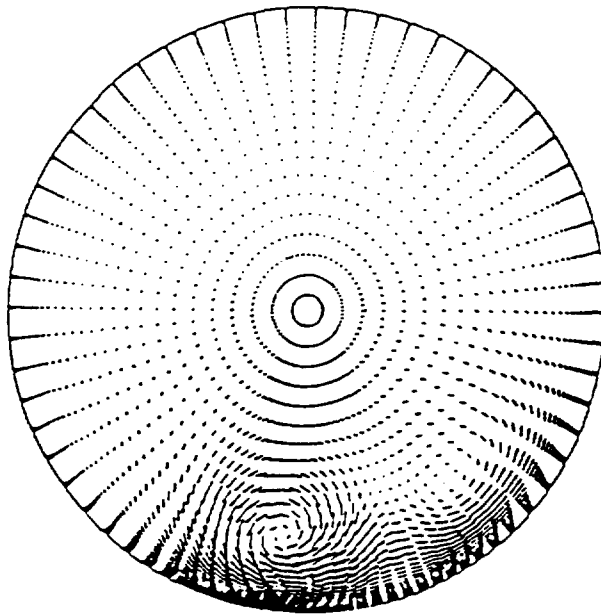
velocity scale

$$\frac{|\vec{v}|}{U_\infty} = 0.5$$

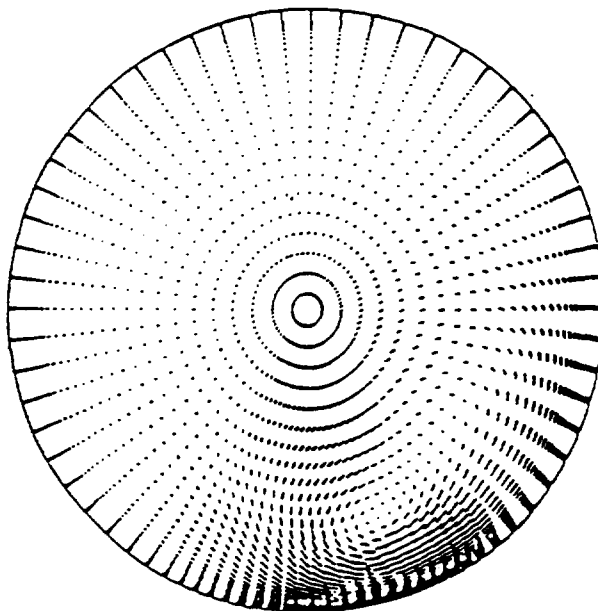


(b) station II ($x/D = 2.90$)

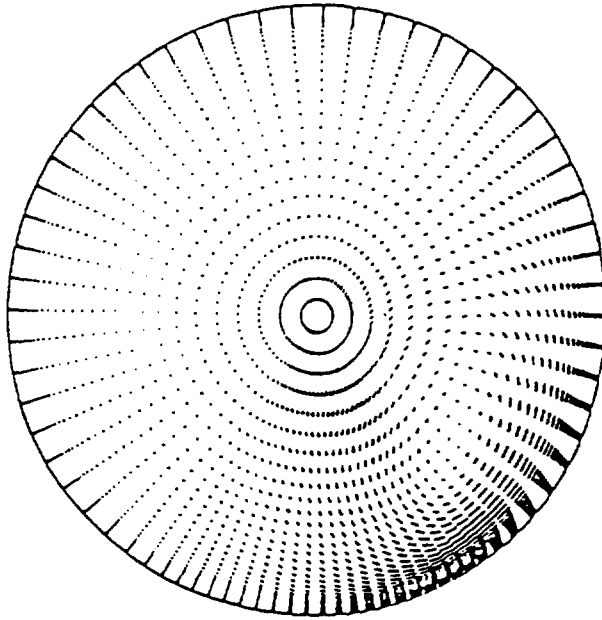
Fig. 5.11 Secondary velocity profiles when the co-rotating vortices are embedded. Vortex(A) has double the strength of vortex (B).
($Ma = 0.6$, $Re_d = 1.0 \times 10^6$)



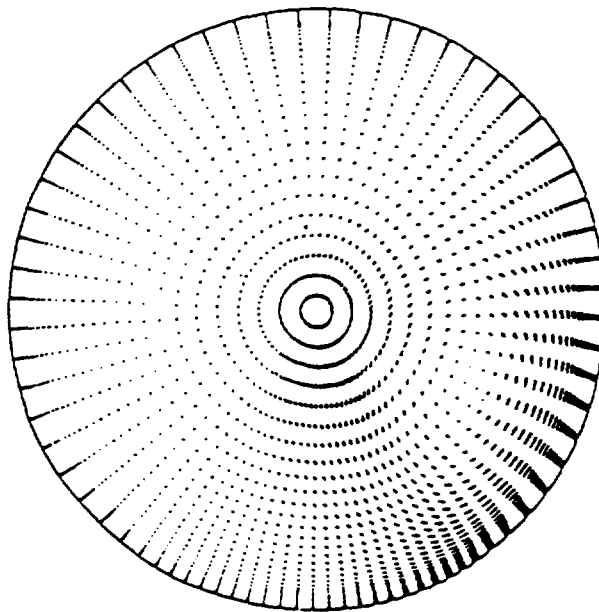
(c) station III ($x/D = 4.24$)



(d) station IV ($x/D = 8.20$)



(e) station V ($x/D = 12.20$)



(f) station VI ($x/D = 16.20$)

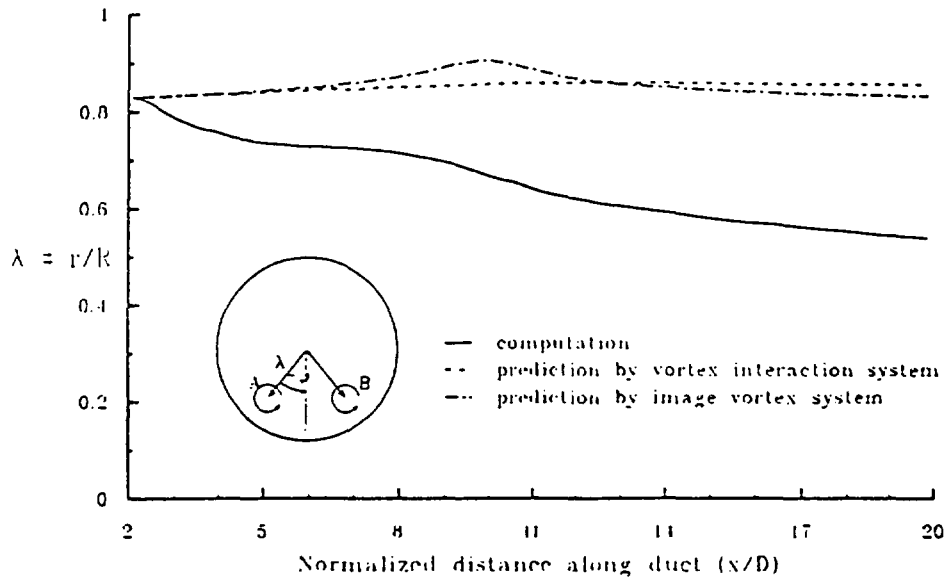


Fig. 5.12(a) Radial trajectory of the vortex(A) which has double the strength of the vortex(B) in the co-rotating vortices.

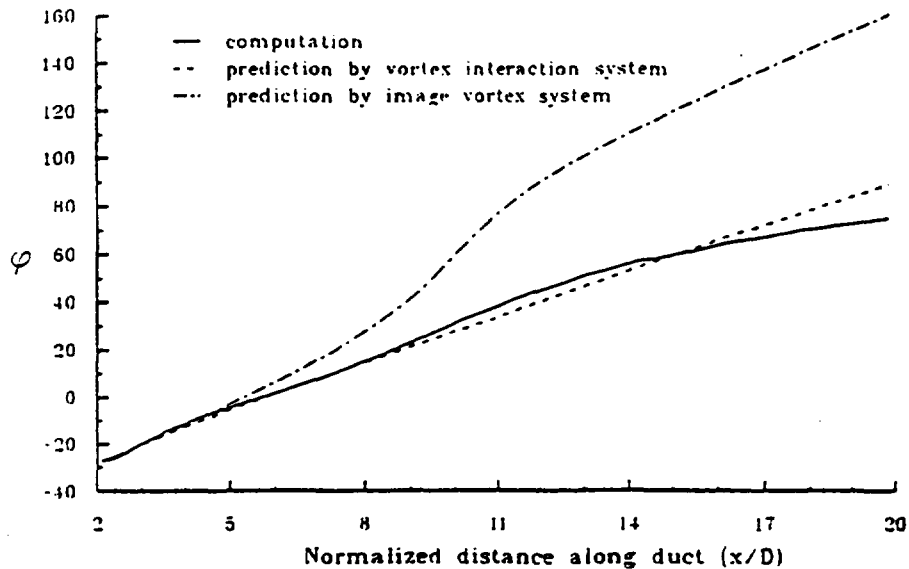


Fig. 5.12(b) Angular trajectory of the vortex(A) which has double the strength of the vortex(B) in the co-rotating vortices.

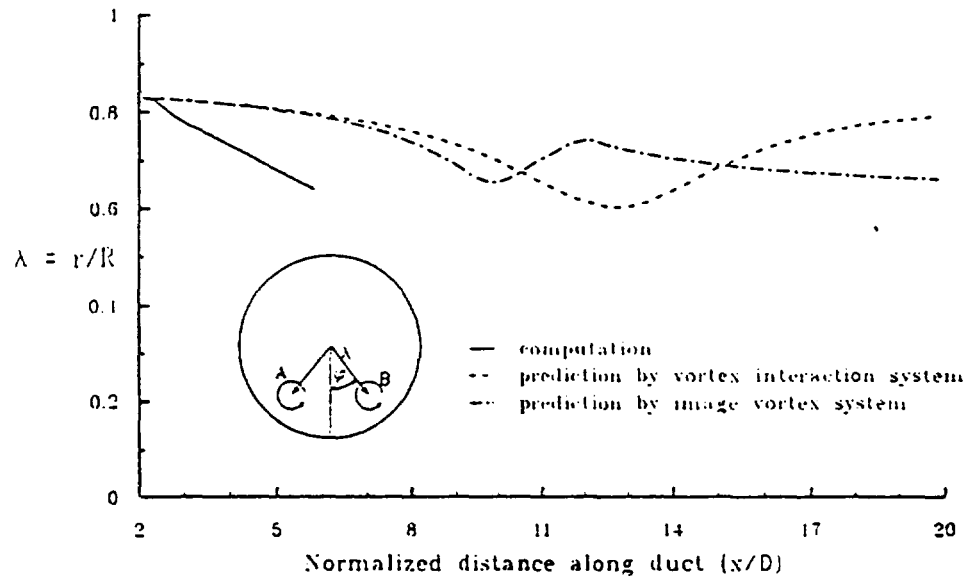


Fig.5.13 (a) Radial trajectory of the vortex(B) which has half the strength of the vortex(A) in the co-rotating vortices.

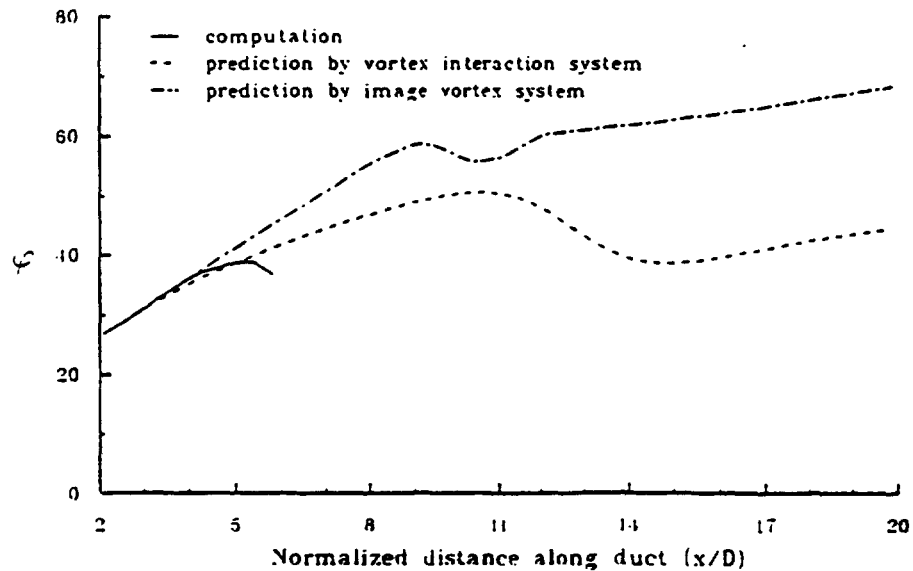


Fig.5.13 (b) Angular trajectory of the vortex(B) which has half the strength of the vortex(A) in the co-rotating vortices.

CHAPTER 6

DIFFUSING S-DUCT WITH VORTEX GENERATORS

6.1 Vortex Model

The shed vortex from the vortex generators is modeled by introducing two-dimensional vortical flow in the cross-plane. Eq. (5.10) provides this vortical structure.

$$u_\theta = \frac{\Gamma}{2 \pi r} \left[1 - \exp \left(-\frac{U_\infty r^2}{4 \nu x} \right) \right] \quad (5.10)$$

Γ is the vortex strength at the tip of the vortex generator. The Γ term is a function of the geometry of the generator, and the oncoming flow conditions. Γ is defined by the strength of one fully rolled up trailing vortex;

$$\Gamma = C_\alpha \frac{c_L}{2} c_l u \quad (6.1)$$

where c_L is the lift coefficient, c_l is the chord length of the vortex generator, u is the velocity of the flow at the generator tip, and C_α is the constant which considers the viscosity and turbulence effect, etc.,. C_α cannot be greater than 0.45 according to inviscid wing theory and by experiment.

Three pairs of one half of the NACA0012 wing section were used as the vortex generators in the Vakili et al.(1986) experiment. They were installed in the duct at $S/D_i = 0.087$, and at azimuthal angles of -41.4° , 0.0° and $+41.4^\circ$. The height and chord length of the vortex generator were $h/D_i = 0.715 \times 10^{-1}$ and $c_i/D_i = 0.108$, respectively. The vortex generator pairs had geometric incidence angles of $+14^\circ$ and -14° relative to the duct centerplane.

Eq. (6.1) can be expressed in nondimensional form;

$$\frac{\Gamma}{D_i U_\infty} = C_\alpha \frac{C_L}{2} \frac{c_i}{D_i} \frac{u}{U_\infty} \quad (6.2)$$

From the experimental conditions, u/U_∞ is taken as 1 and C_L is assigned as 1.4 because the incident angle of the vortex generator is 14° . In this study, six different vortex strengths $\Gamma/D_i U_\infty = 0.005, 0.010, 0.015, 0.020, 0.025$ and 0.030 are investigated to compare with the experimental data and to study the parametric effect of different vortex strengths. When the vortex strength ($\Gamma/D_i U_\infty$) is equal to 0.030 , C_α is 0.4 . In the choice of various vortex strength, the decreasing of the vortex strength implies that the incident angle of the mounted vortex generator is decreasing.

In Eq. (5.10), the length x is estimated to be the

distance $0.087D_i$ from the location of the vortex generator to the crossplane of the vortical structure. The rotational velocities at the cross plane ($S/D_i = 0.17$) are evaluated with the image vortices based on the circle theorem mentioned in section 4.2.1. If the rotational velocity near the vortex core is greater than $U_\infty/5$, the velocity at that point is assumed to be of that magnitude. These secondary velocities of the vortex model are added to the secondary velocities without vortex generator at the same plane. The combined vortical structures are applied as the source term in the crossplane. Fig. 6.1 shows the secondary flow structure at this plane.

In this computation, the residuals for these numerical solutions were reduced approximately three orders of magnitude. Solutions were obtained on the Cray-YMP. The number of iterations required to obtain the converged solutions were approximately 25,000. The computational speed was 950 iterations per CPU hour. The mass flow changes between the inlet and exit was within 1 percent.

6.2 Results and Discussion

Fig. 6.2 shows values of the computed static-pressure coefficients (continuous curves in the figure) and

experimental values (symbols) at $\varphi = 10^\circ$, 90° and 170° for various vortex strengths. Numerical results with $\Gamma/D_i U_\infty = 0.025$ are close to the experimental data. In the following discussion, these numerical results will be compared with the experimental results obtained by Vakili et al. (1986). The surface static-pressure distribution at $\varphi = 170^\circ$ shows some deviation between the experimental and numerical results near the location of the vortex generators. Recent experimental results on the same geometry by Reichert and Wendt (1992) show that there is no perceptible upstream influence on the static-pressure distribution, caused by the vortex generator arrays. In their experiment, Wheeler wishbone generators are used. This type of generator forms a pair of counter-rotating vortices with the flow between vortices directed upwards. However, the experimental data obtained by Vakili et al. (1986) show some influence on the static-pressure distribution by the vortex generator arrays. The influence of the vortex generator arrays on the static-pressure distribution depends on the location of the vortex generators and data acquisition points, but the vortex model employed in this study shows very little upstream influence on the static-pressure distribution, as can be seen in Fig. 6.3.

For the smallest vortex strength ($\Gamma/D_i U_\infty = 0.005$), the

results differ only marginally from the flow without vortex generators as shown in Fig. 6.3(a). Figs. 6.3(b) and 6.3(c) show higher values of static-pressure for the larger vortex strength in the second half bend of the duct. The static-pressure distribution lines cross each other at the inflection point of the duct ($S/D_i = 2.62$). The static-pressure value at the cross point is less than the peak value at $\varphi = 0^\circ$ near $S/D_i = 2.5$. These results are very similar to the experimental results conducted by Reichert and Wendt(1992).

In Figs. 6.3(a) and 6.3(b), the constant static-pressure values at $\varphi = 170^\circ$ in $3 < S/D_i < 4$ are associated with the flow separation. These figures show that the region of the constant static-pressure value decreases with increasing the vortex strength. The reverse flow of streamwise velocity dose not occur when the injected vortex strength is greater than $\Gamma/D_i U_\infty = 0.020$.

Fig. 6.4 shows the secondary velocity profiles compared with the experimental results. The computed and experimental results show on the right hand side and left hand side, respectively; only half of the cross-plane is shown because the flow is symmetric along the duct cross section. The numerical results agree closely with the experimental results except the behavior of the vortices(C)

along the downstream. Note that the resolution and the locations of data collection points of the experiment and computations are different. The computational results of Fig. 6.4(a) are plotted in a denser resolution in order to show more clearly the vortices just downstream of the vortex generators.

At the first half bend, the high energy flow moves toward the upper wall and the low energy flow migrates circumferentially from the upper wall to the lower wall. In Fig. 6.1, the rotational velocities of the injected vortices(B) have the same direction as the low energy flow near the wall, but vortices(A) and (C) have opposite rotational velocities to the low energy flow. This makes the secondary velocities of vortices(B) results in stronger than those of the other vortices. It also makes vortices(C) more quickly decaying. In the experimental results, the vortices(C) do not decay as quickly as in the computation; even if the strength of vortices(C) is weaker than the other vortices. The low energy flow at the vortex plane is retarded by the installed vortex generators on the wall. This means the injected vortices have little influence from the low energy flow. The vortical structure of the vortex model is strongly influenced by the low energy flow at the location of the vortex generators.

Fig. 6.5 shows the total-pressure contours compared

with the experimental results. The small effect of the vortices(C) is clearly shown in this figure. The thickness of the computed "boundary layer" at $\varphi = 90^\circ$ is less than observed experimentally.

The static-pressure contours are shown in Fig 6.6. The numerical results agree qualitatively with the experimental results. In the first half bend, higher static pressure is shown near the upper wall because of the duct curvature. Opposite behavior is shown in the second half bend owing to the same reason.

The variation of the boundary layer thickness at $\varphi = 10^\circ$, 90° and 170° along the duct is shown in Fig. 6.7. The boundary layer thickness is defined as the normal distance from the wall where the total-pressure coefficient is 1.0. The boundary layer thickness of the flow with vortex generators depends greatly on the vortex strength. The computed boundary layer thickness at $\varphi = 90^\circ$ is less than the experimental result because the injected vortices(C) are weaker than the experimental values. However, the computed results show that the trend of the boundary layer thickness variation along the duct is quite similar to the experimental results.

Fig. 6.8 shows the total-pressure contours with and without vortex generators. The right hand side and left hand side show the numerical results with and without

vortex generators, respectively. The effect of the injected vortices is clearly shown in this figure. The injected vortices push the high energy flow toward the lower energy region. This resulting force prevents the flow separation at the inflection point of the duct.

Fig. 6.8(a) to (c) show that the boundary layer thickness of the flow with vortex generators near the upper wall is less than that of the flow without vortex generators. This results from satisfying a constant mass flux because the shed vortices injected near the lower wall cause a streamwise velocity deficit in the region of the vortex core. However, the experimental results do not show any difference between the boundary layer thicknesses with and without vortex generators in the upper wall of the first half of the duct. This probably results from deficiencies in the experiments, primarily coarse data acquisition locations and uncertainties in the total pressure measurements using pitot tubes.

Fig. 6.9 shows the secondary velocity profiles with and without vortex generators. The interaction between the injected vortices and the counter-rotating vortices resulting from the flow separation is clearly shown in this figure. The injected vortices suppress the growth of these counter-rotating vortices.

The static-pressure contours with and without vortex

generators are shown in Fig. 6.10. At the vortical plane ($S/D_1 = 0.17$), the distortion of the constant static-pressure contours is a result of the injected vortices. The change of the static-pressure along the duct shows the same flow phenomena as mentioned in the discussion of the flow without vortex generators. Figs. 6.10(d) and 6.10(e) show that the constant static-pressure contours are flatter in the low energy flow region of the second half bend. The injected vortices result in a more uniform flow and higher diffusion at the exit than occurs without vortices.

Figs. 6.11 and 6.12 show the numerical results with the vortex strength ($\Gamma/D_1 U_\infty = 0.015$). The computed results show that the effect of the injected vortices is weaker than with the strong vortex strength ($\Gamma/D_1 U_\infty = 0.025$), as one could expect. The region of diminished total-pressure at the exit is larger and the static-pressure contours are more distorted. Fig. 6.12 shows the interaction between the injected vortices and the counter-rotating vortices resulting from the flow separation. It also shows that the growth of these counter-rotating vortices are suppressed by the injected vortices. Fig. 6.12(e) shows that the secondary velocities between the vortices(A) are overestimated. This results from the small eddy viscosity in the flow separation region as mentioned in the

discussion of the flow without vortex generator.

Fig. 6.13 shows the total-pressure contours at the exit with different vortex strengths. The region of diminished total-pressure is significantly reduced with increasing the vortex strength.

A total-pressure recovery (\bar{C}_{p0}) is calculated using area weighted values from the computational mesh over the cross stream plane.

$$\bar{C}_{p0} = \frac{1}{A} \int C_{p0} dA \quad (6.3)$$

Using a similar method, the total-pressure recovery of a segment is determined by integrating the total-pressure coefficient over a segment of the cross stream plane of angular extent φ .

$$\bar{C}_{p0}(\varphi) = \frac{\int^{\varphi} C_{p0} dA}{\int^{\varphi} dA} \quad (6.4)$$

A distortion coefficient is useful to describe the efficiency of inlet duct or to compare the performance of several inlet ducts. There are many ways to define the distortion coefficient depending on the comparison purposes. Distortion coefficients measuring radial or circumferential distortion have been used. Early workers

simply defined the distortion coefficient in experiment to be the difference of the normalized maximum rake total-pressure and the normalized minimum rake total-pressure. In this study, the distortion coefficient $DC(\varphi)$ is defined using the cross stream plane segment that results in the lowest value of $\bar{C}_{po}(\varphi)$. In case of S-duct, the segment angle φ is defined to the azimuthal angle from the centerline in the lower energy region. The values of φ are chosen to 60° , 90° and 120° .

$$DC(\varphi) = \bar{C}_{po} - \bar{C}_{po}(\varphi) \quad (6.5)$$

Fig. 6.14 show the total-pressure recovery at the exit with various vortex strengths. Fig. 6.15 show the distortion coefficient at the exit. For the smallest vortex strength ($\Gamma/D_1 U_\infty = 0.005$), the total-pressure recovery is slightly reduced. This indicates that the small vortex strength acts as flow blockage at the location of the vortex generators. The vortex strength is quickly reduced in the first half bend. The resulting force is not enough to suppress the counter-rotating vortices resulting from the flow separation. Small vortex strength is seen to affect the flow in a detrimental way. This phenomenon with small vortex strength is shown in the experiment by Reichert and Wendt(1992). The total-pressure recovery and

distortion coefficient significantly improved with increasing vortex strength.

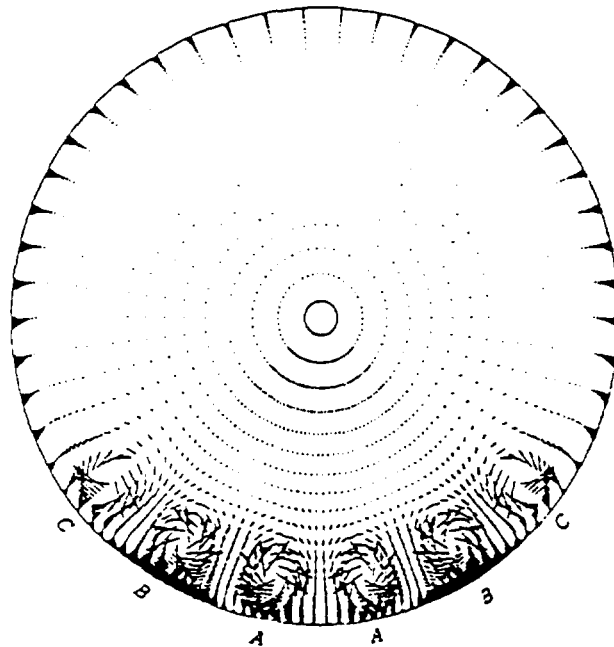


Fig. 6.1(a) Secondary flow structure from vortex generator model at $S/D_i = 0.17$

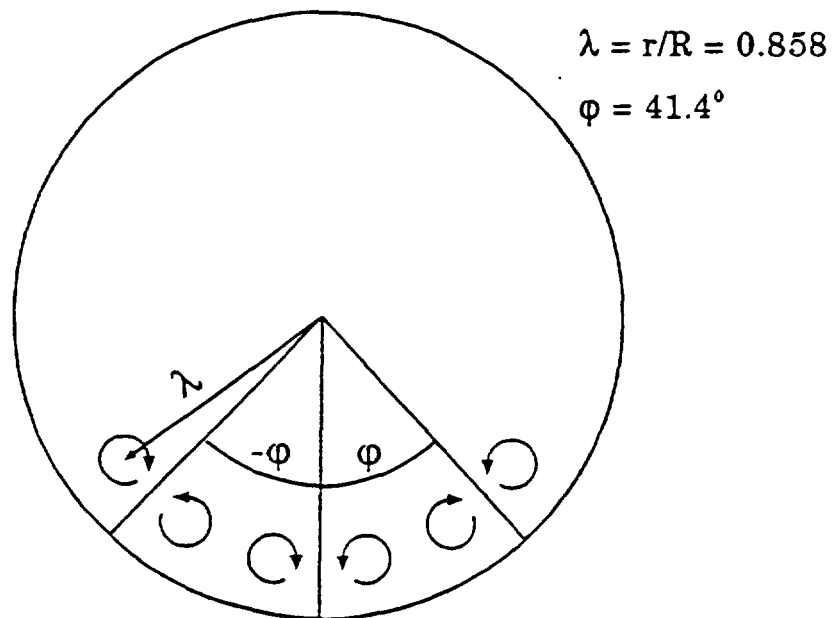


Fig. 6.1(b) Location of injected vortices at $S/D_i = 0.17$

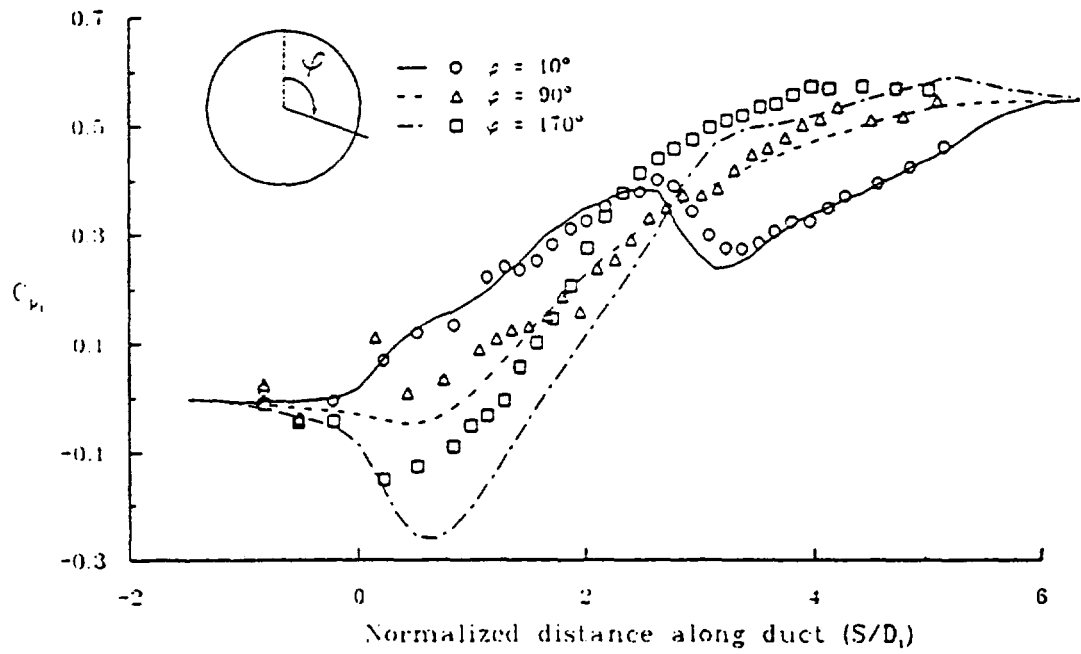


Fig. 6.2(a) Axial surface-static pressure coefficient.
 $C_{p1} = (p_{\text{local}} - p_{\text{ref}}) / q_{\text{ref}}$
 ($Ma = 0.6$, $Re_d = 1.76 \times 10^6$, $\Gamma/D_1 U_\infty = 0.020$)
 Exp. Vakili et al. (1986)

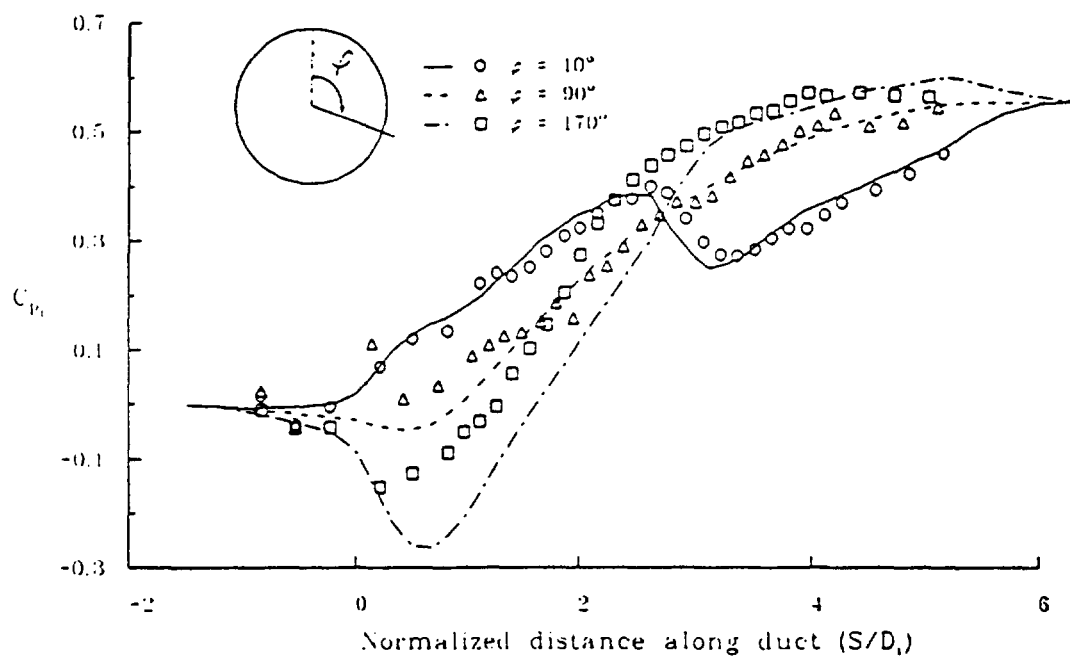


Fig. 6.2(b) Axial surface-static pressure coefficient.

$$C_{pi} = (p_{local} - p_{ref}) / q_{ref}$$

($Ma = 0.6$, $Re_d = 1.76 \times 10^6$, $\Gamma/D_i U_\infty = 0.025$)

Exp. Vakili et al. (1986)

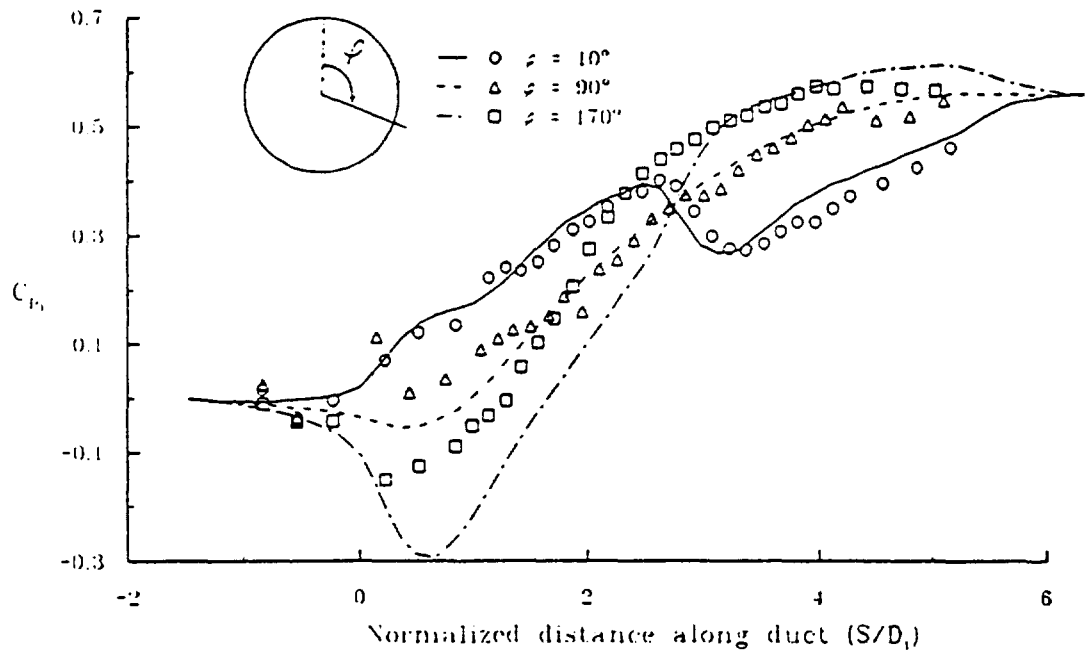


Fig. 6.2(c) Axial surface-static pressure coefficient.

$$C_{ps} = (p_{local} - p_{ref}) / q_{ref}$$

($Ma = 0.6$, $Re_d = 1.76 \times 10^6$, $\Gamma/D_1 U_\infty = 0.030$)

Exp. Vakili et al. (1986)

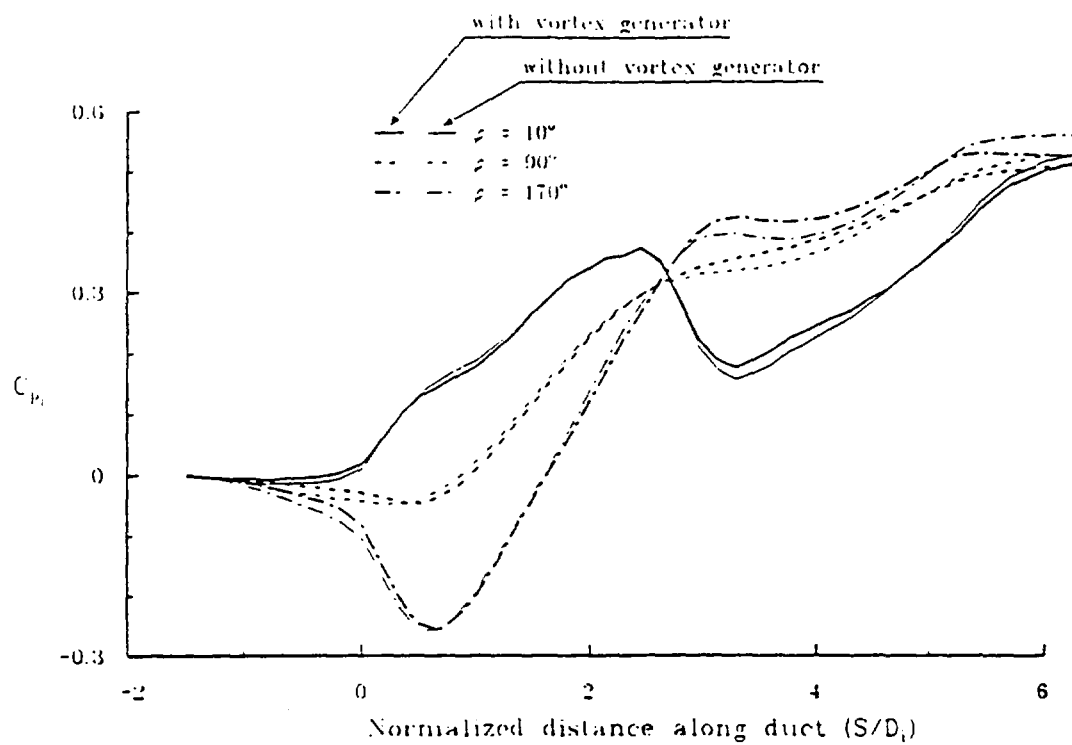


Fig. 6.3(a) Comparison of axial static-pressure coefficient with/without vortex generators.

$$C_{pi} = (P_{local} - P_{ref}) / q_{ref}$$

($Ma = 0.6$, $Re_d = 1.76 \times 10^6$, $\Gamma / D_t U_\infty = 0.005$)

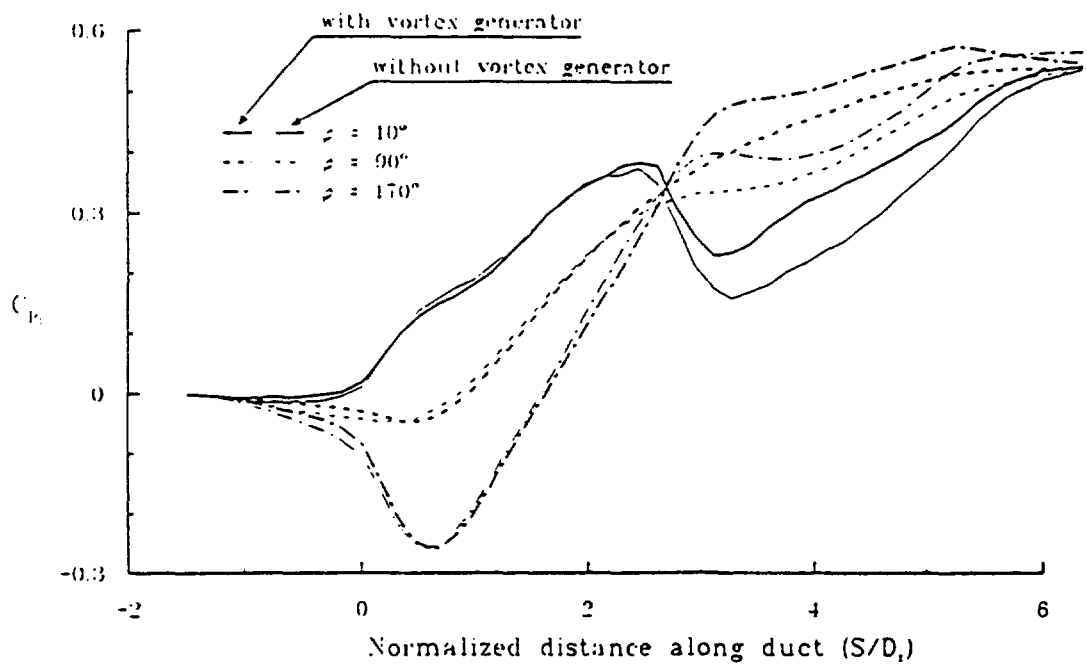


Fig. 6.3(b) Comparison of axial static-pressure coefficient with/without vortex generators.

$$C_{pi} = (p_{local} - p_{ref}) / q_{ref}$$

($Ma = 0.6$, $Re_d = 1.76 \times 10^6$, $\Gamma/D_i U_\infty = 0.015$)

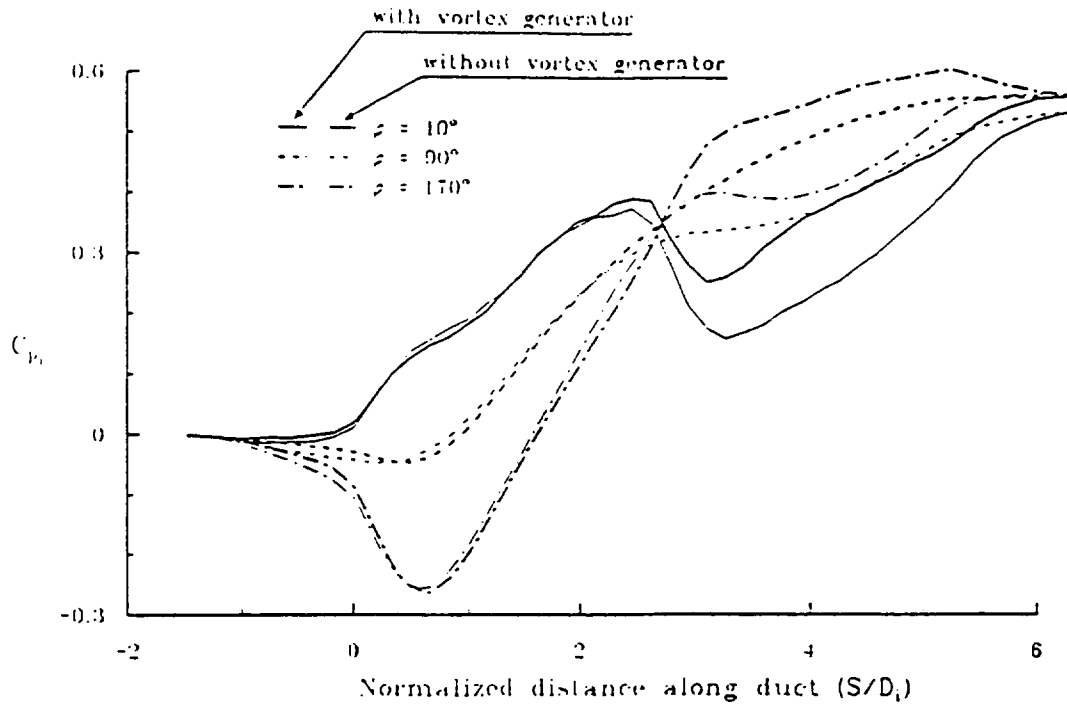
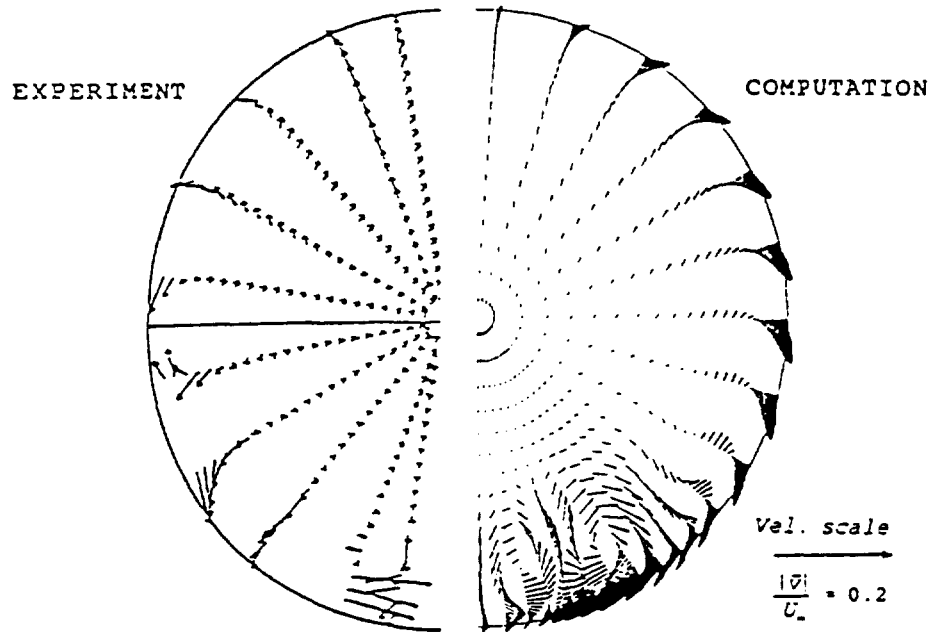
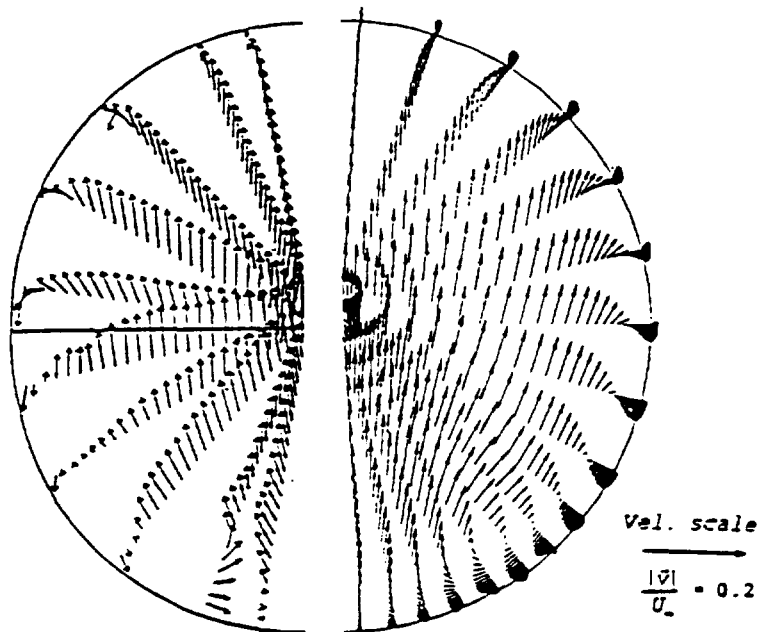


Fig. 6.3(c) Comparison of axial static-pressure coefficient with/without vortex generators.
 $C_{pi} = (p_{local} - p_{ref}) / q_{ref}$
 ($Ma = 0.6$, $Re_d = 1.76 \times 10^6$, $\Gamma/D_i U_\infty = 0.025$)

SECONDARY VELOCITY VECTORS
(Vortex strength, $\Gamma/D_i U_\infty = 0.025$)



(a) at $S/D_i = 1.31$

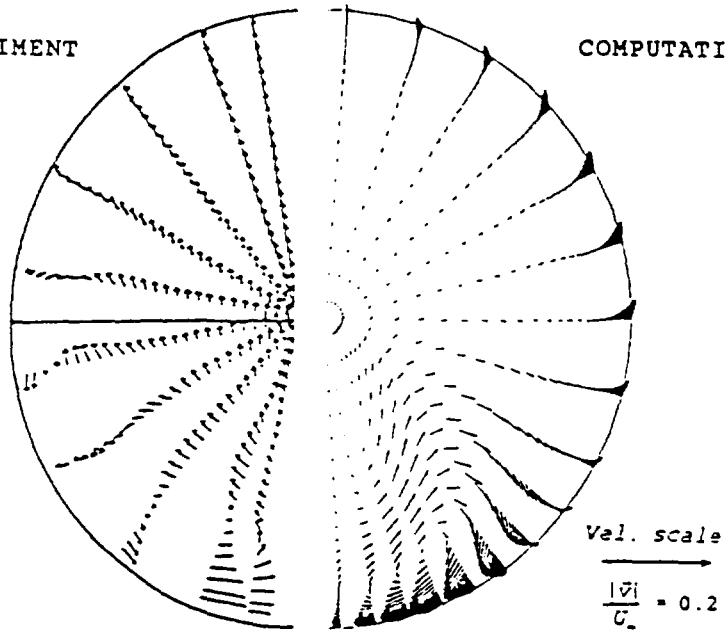
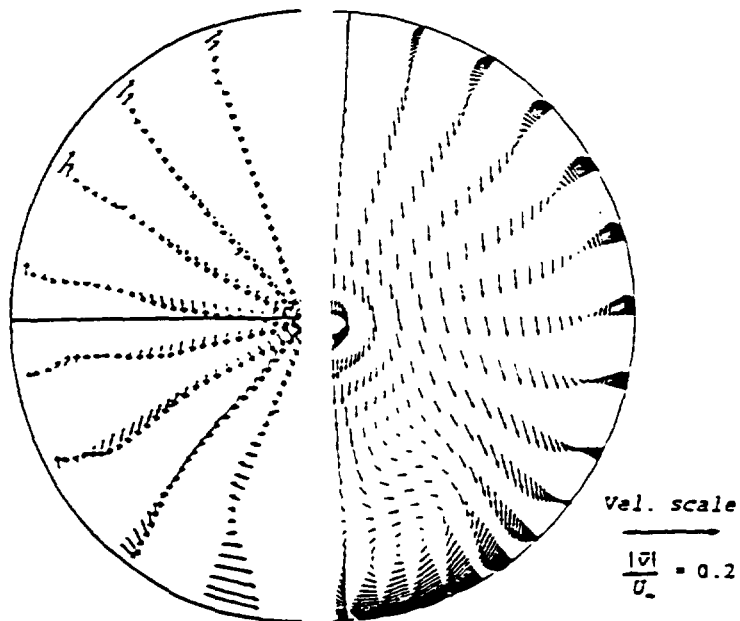


(b) at $S/D_i = 2.62$

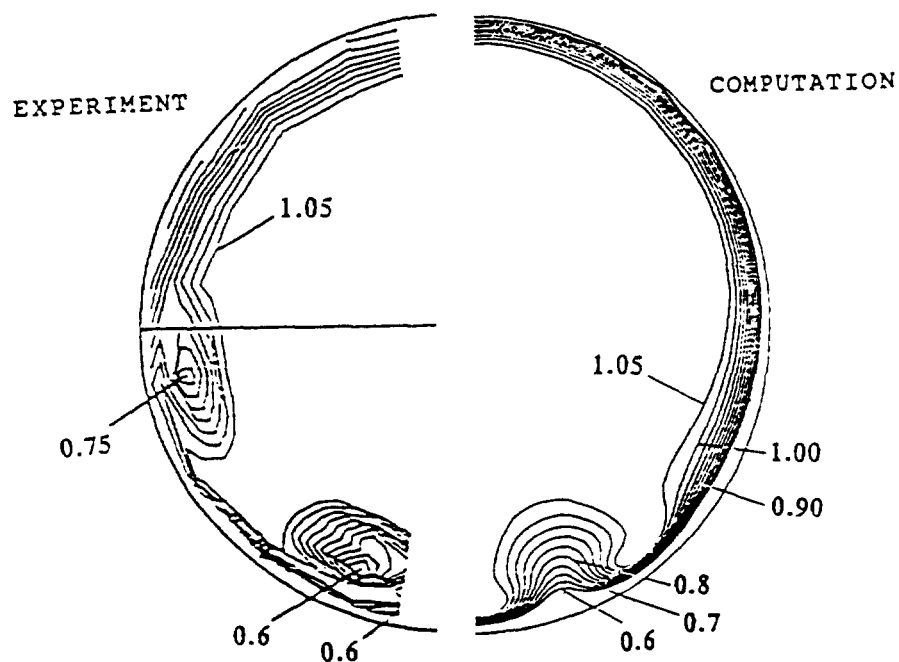
Fig. 6.4 Secondary velocity profiles with vortex generators.
($Ma = 0.6$, $Re_d = 1.76 \times 10^6$, $\Gamma/D_i U_\infty = 0.025$)
Exp. Vakili et al. (1986)

EXPERIMENT

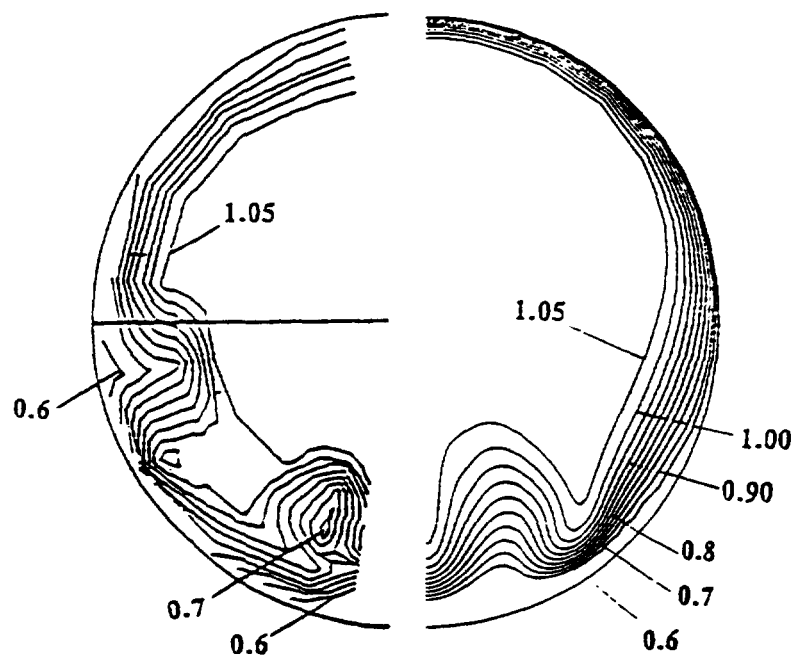
COMPUTATION

(c) at $S/D_1 = 3.93$ (d) at $S/D_1 = 5.24$

TOTAL PRESSURE COEFFICIENT CONTOURS
(Vortex strength, $\Gamma/D_i U_\infty = 0.025$)



(a) at $S/D_i = 1.31$

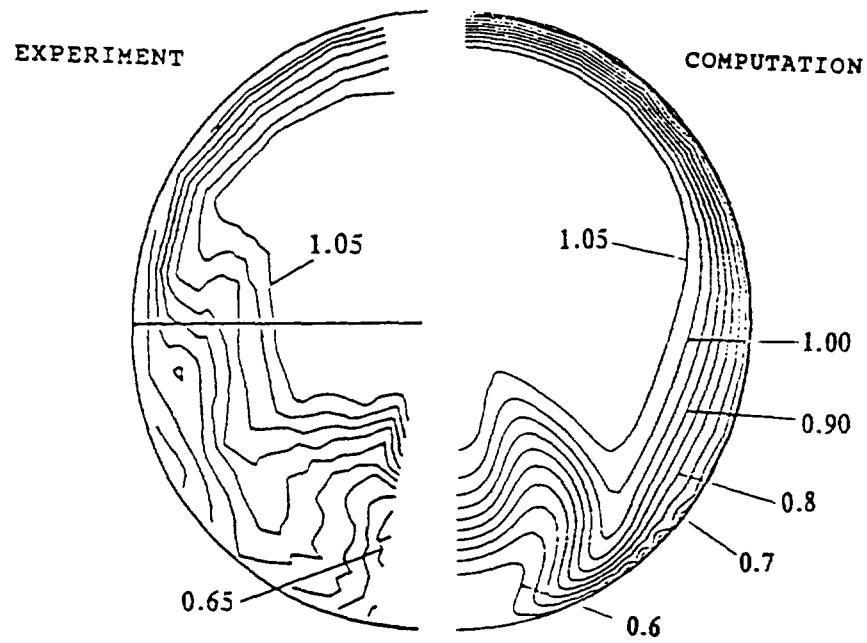
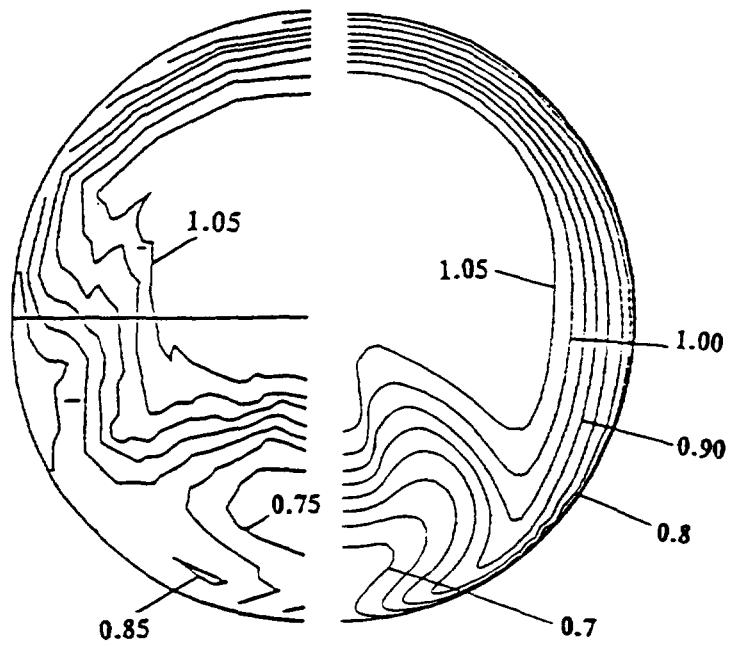


(b) at $S/D_i = 2.62$

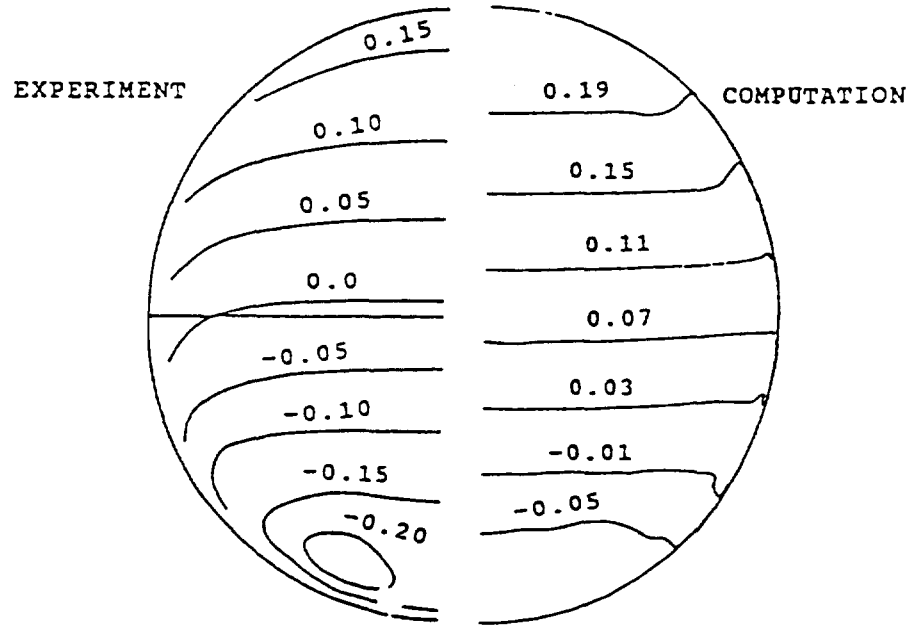
Fig. 6.5 Total-pressure coefficient contours with vortex generators.

($Ma = 0.6$, $Re_d = 1.76 \times 10^4$, $\Gamma/D_i U_\infty = 0.025$)

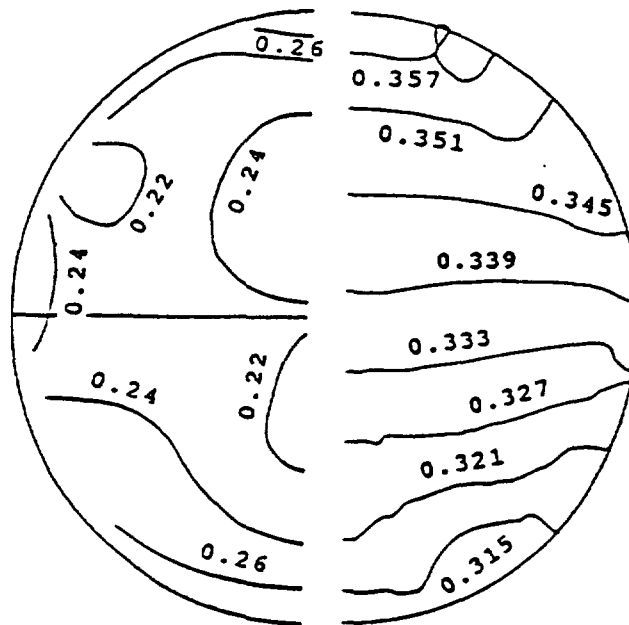
Exp. Vakili et al.(1986)

(c) at $S/D_i = 3.93$ (d) at $S/D_i = 5.24$

STATIC PRESSURE COEFFICIENT CONTOURS
(Vortex strength, $\Gamma/D_i U_\infty = 0.025$)

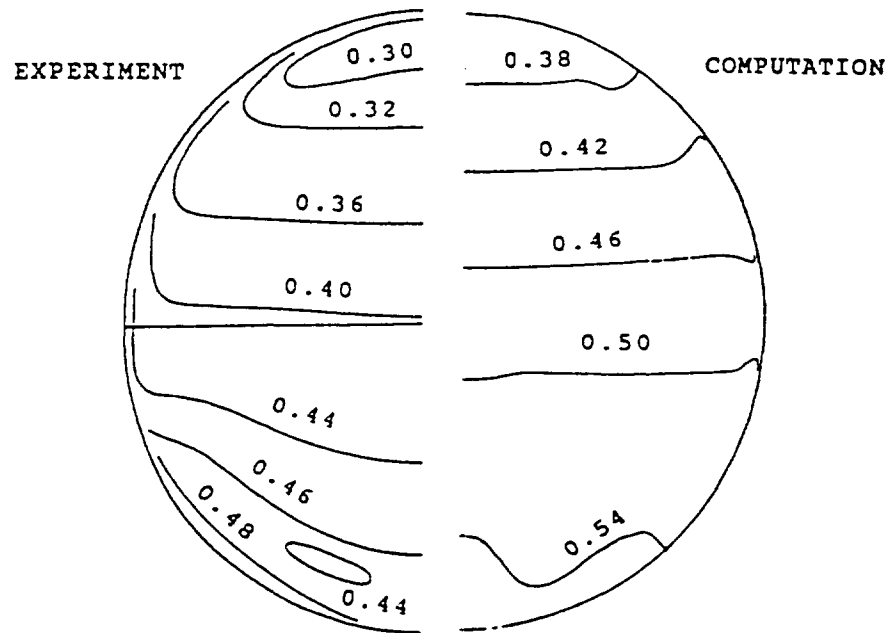
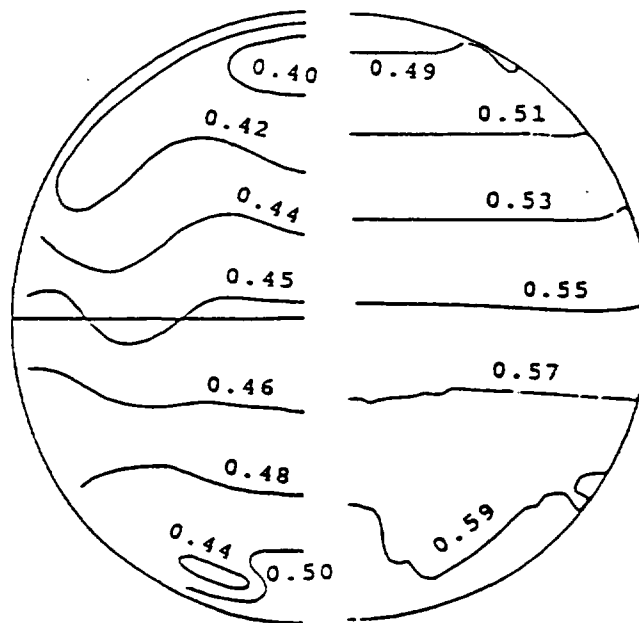


(a) at $S/D_i = 1.31$



(b) at $S/D_i = 2.62$

Fig. 6.6 Static-pressure coefficient contours with vortex generators.
($Ma = 0.6$, $Re_d = 1.76 \times 10^6$, $\Gamma/D_i U_\infty = 0.025$)
Exp. Vakili et al. (1986)

(c) at $S/D_i = 3.93$ (d) at $S/D_i = 5.24$

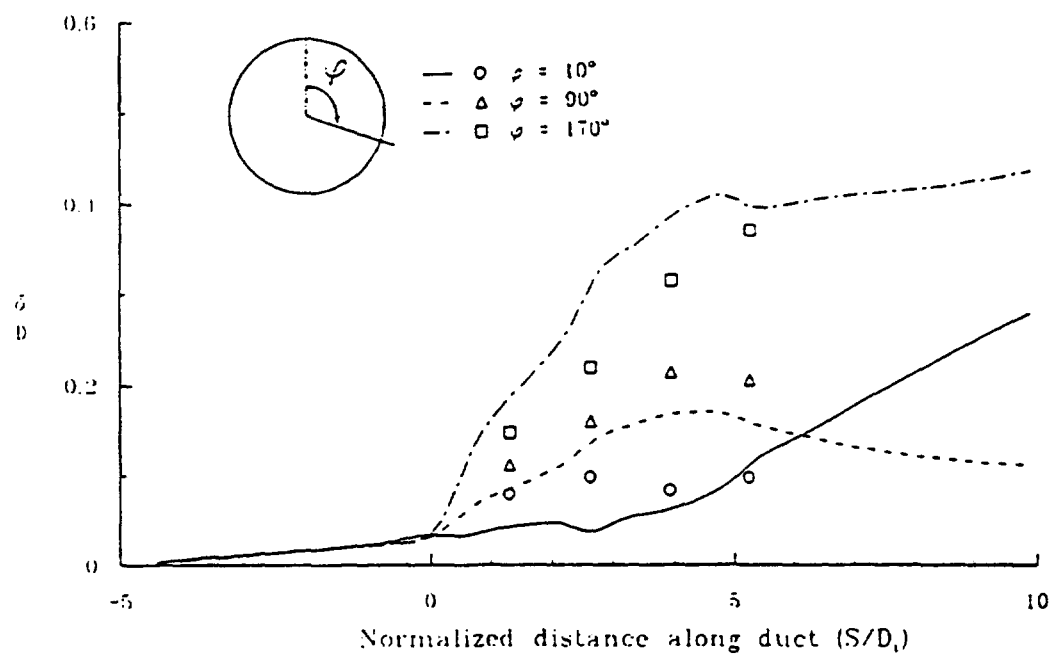


Fig. 6.7 Boundary layer thickness.
 ($Ma = 0.6$, $Re_d = 1.76 \times 10^6$, $\Gamma/D_1 U_\infty = 0.025$)
 Exp. Vakili et al. (1986)

TOTAL PRESSURE COEFFICIENT CONTOURS

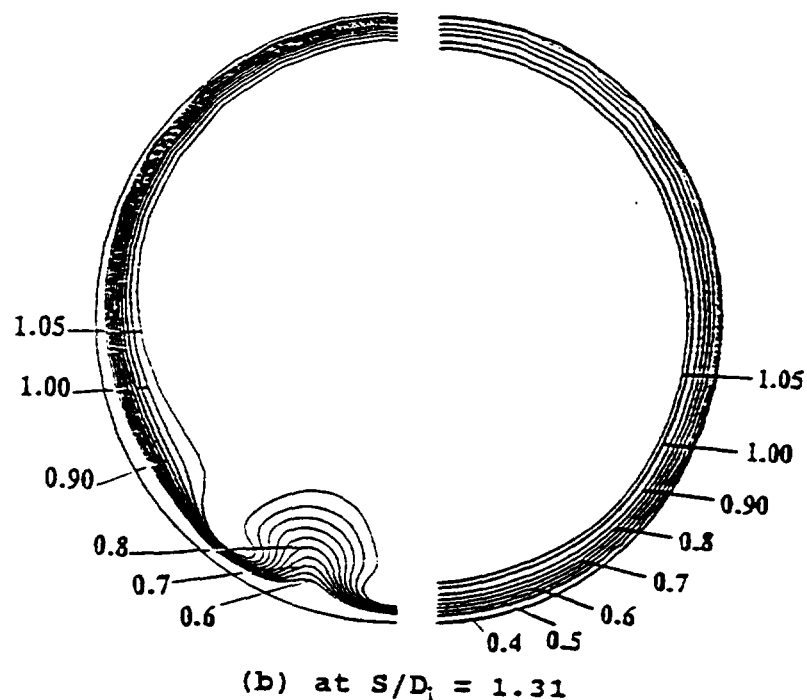
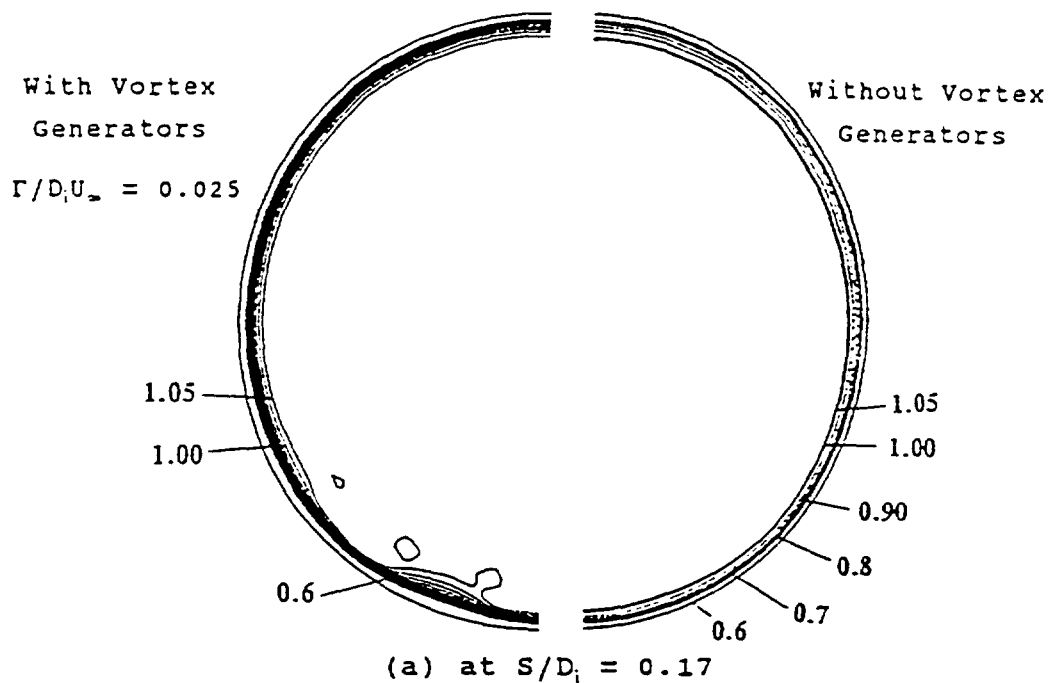
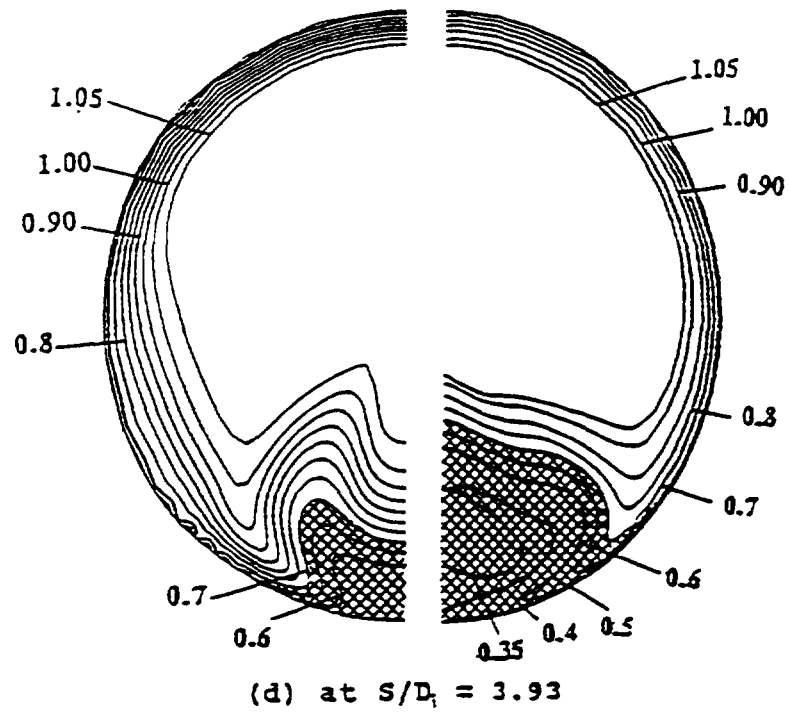
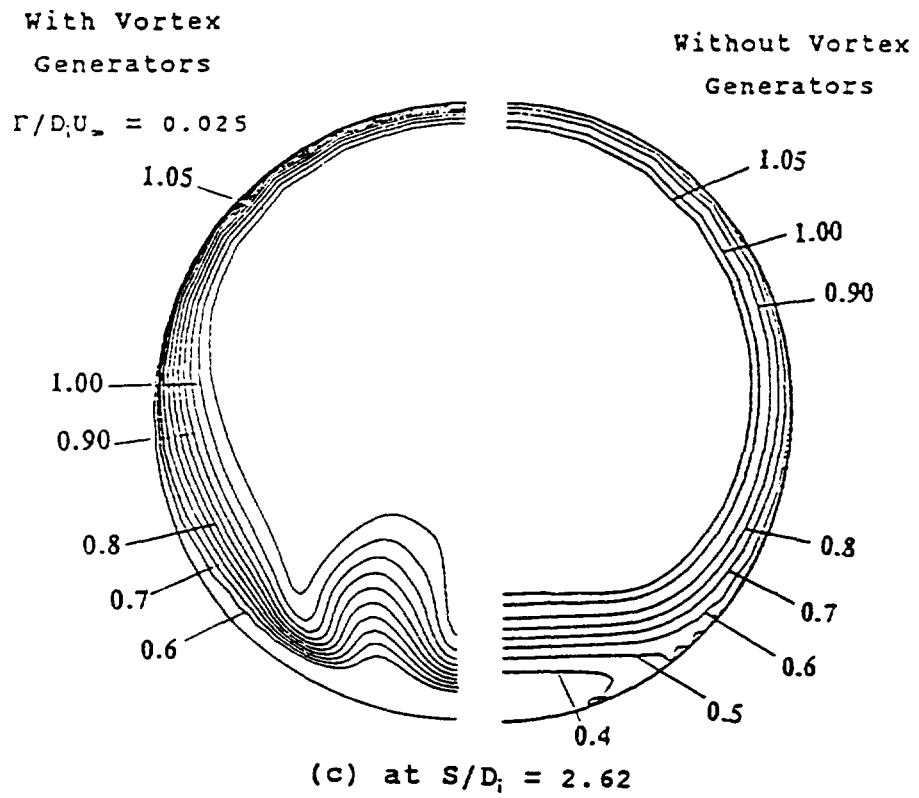


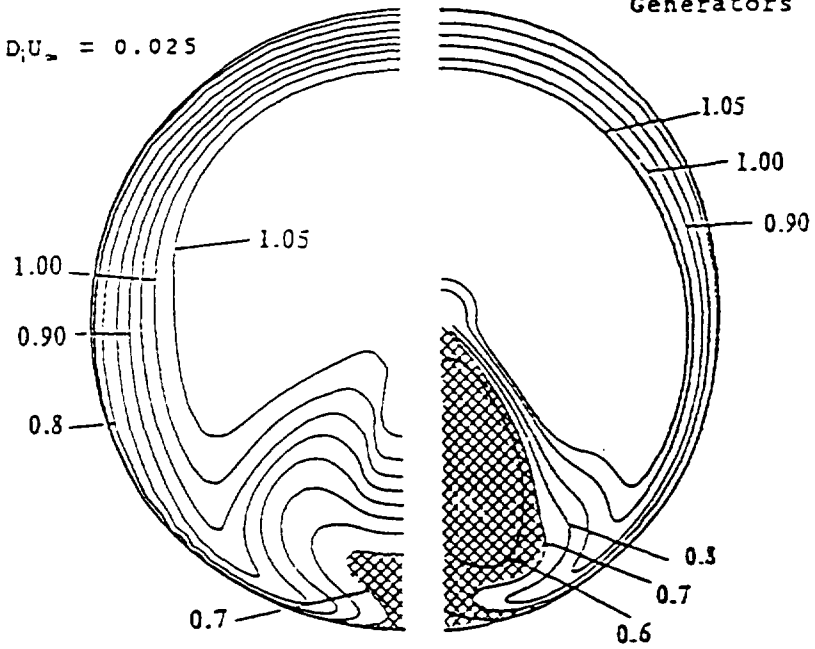
Fig. 6.8 Comparison of the total-pressure coefficient contours with/without vortex generators.
 ($Ma = 0.6$, $Re_d = 1.76 \times 10^6$, $\Gamma/D_1 U_\infty = 0.025$)
 Exp. Vakili et al. (1986)



With Vortex
Generators

$$\Gamma/D_1 U_\infty = 0.025$$

Without Vortex
Generators



(e) at $S/D_1 = 5.24$

SECONDARY VELOCITY VECTORS

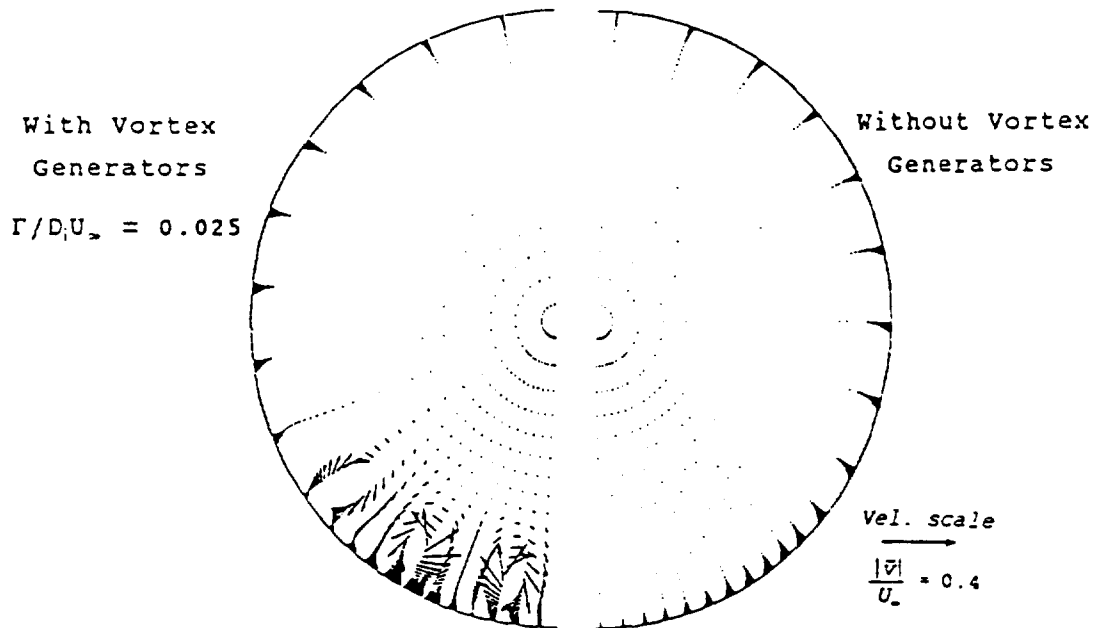
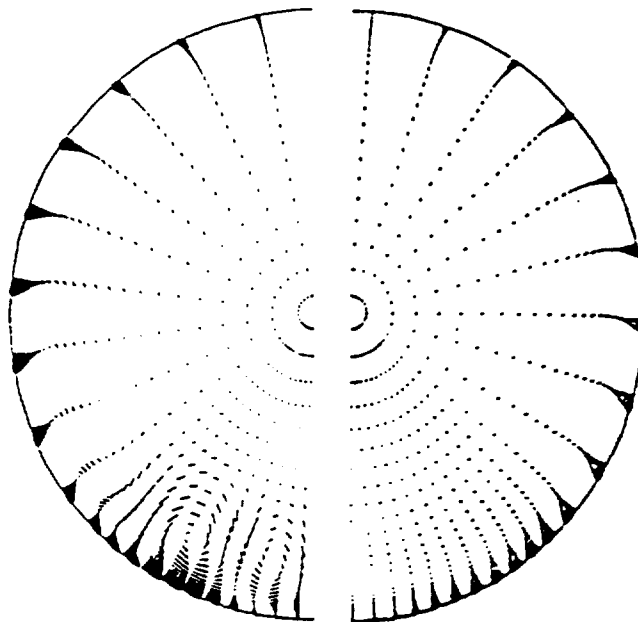
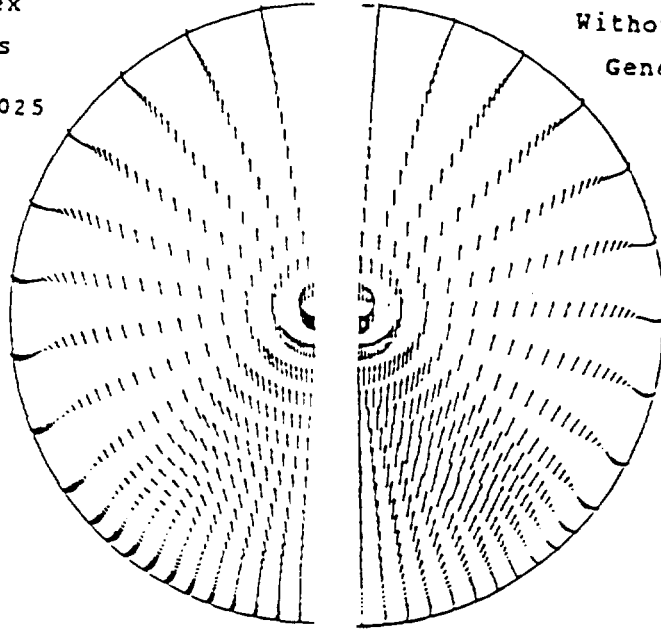
(a) at $S/D_i = 0.17$ (b) at $S/D_i = 1.31$

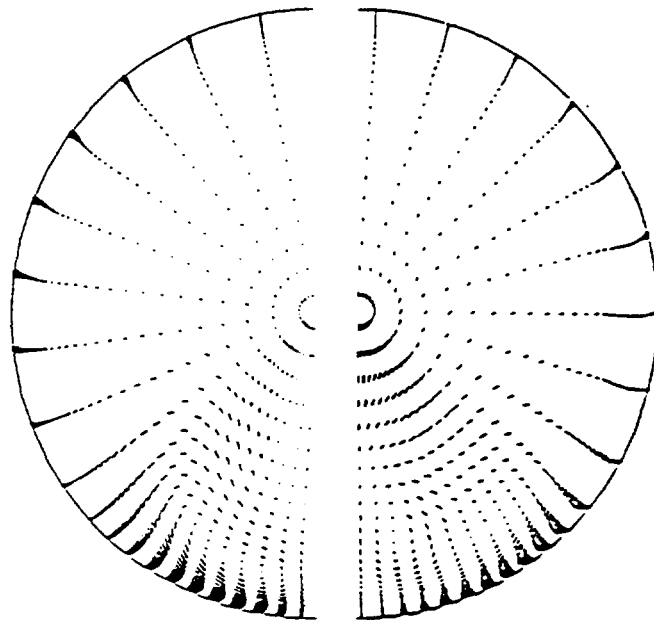
Fig. 6.9 Comparison of the secondary velocity profiles with/without vortex generators.
 ($Ma = 0.6$, $Re_d = 1.76 \times 10^6$, $\Gamma/D_i U_\infty = 0.025$)
 Exp. Vakili et al. (1986)

With Vortex
Generators
 $\Gamma/D_i U_\infty = 0.025$

Without Vortex
Generators



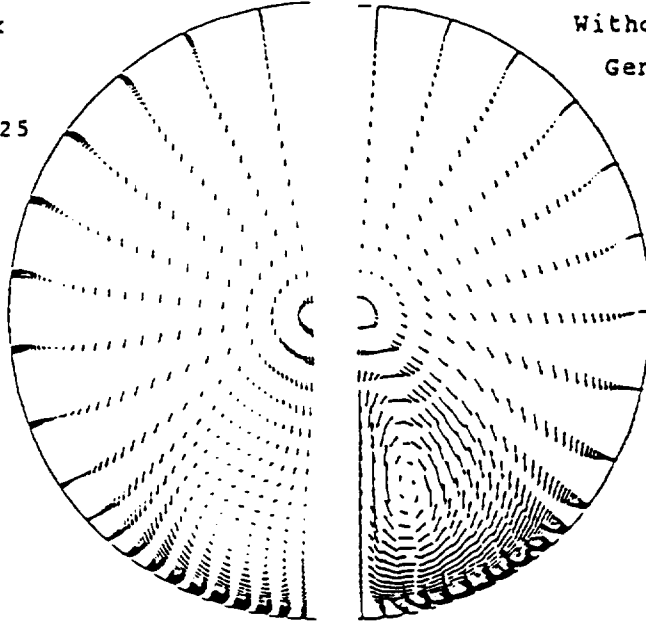
(c) at $S/D_i = 2.62$



(d) at $S/D_i = 3.93$

With Vortex
Generators
 $\Gamma/D_i U_\infty = 0.025$

Without Vortex
Generators



(e) at $S/D_i = 5.24$

STATIC PRESSURE COEFFICIENT CONTOURS

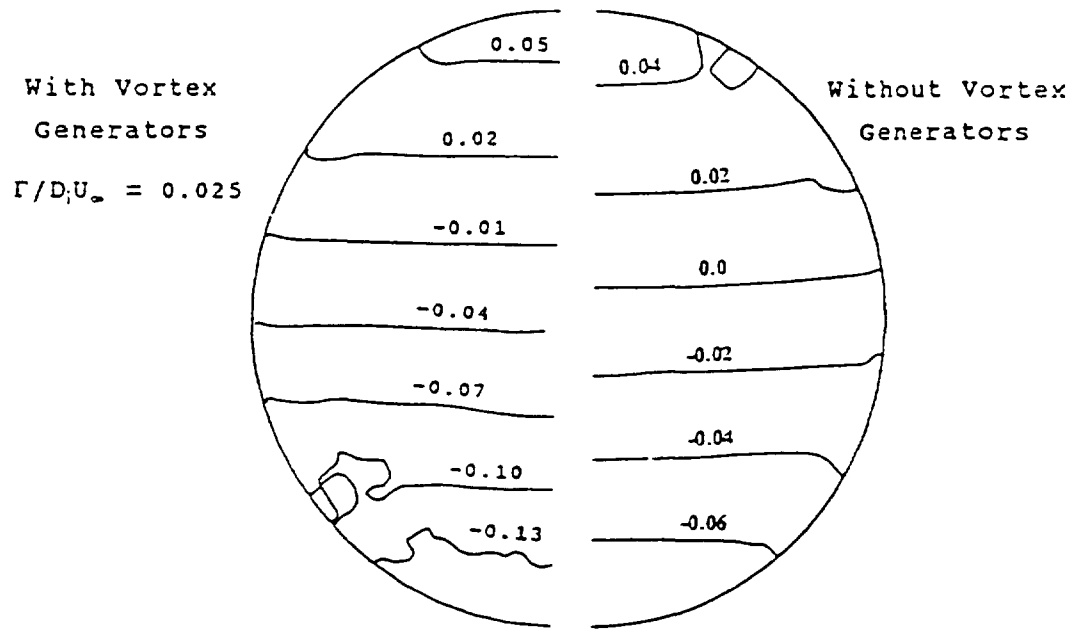
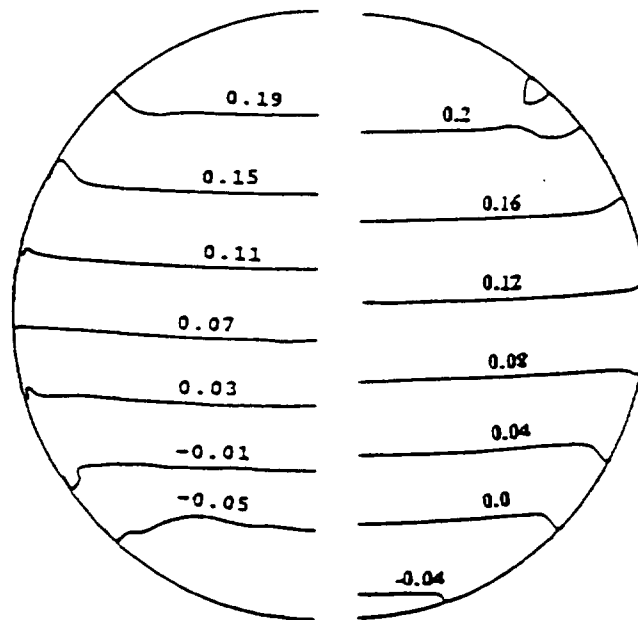
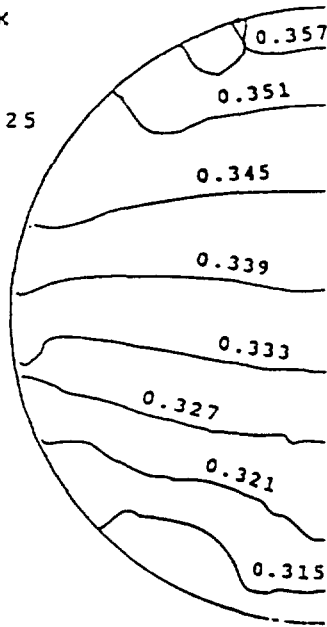
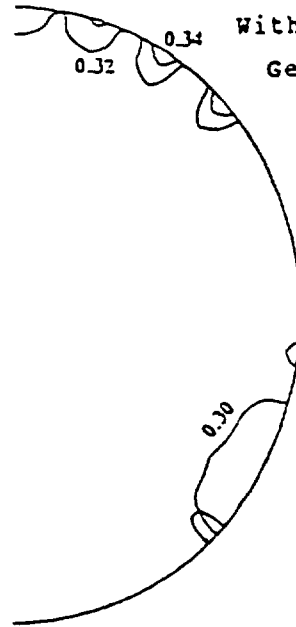
(a) at $S/D_i = 0.17$ (b) at $S/D_i = 1.31$

Fig. 6.10 Comparison of the static-pressure coefficient contours with/without vortex generators.
 ($Ma = 0.6$, $Re_d = 1.76 \times 10^6$, $\Gamma/D_i U_\infty = 0.025$)

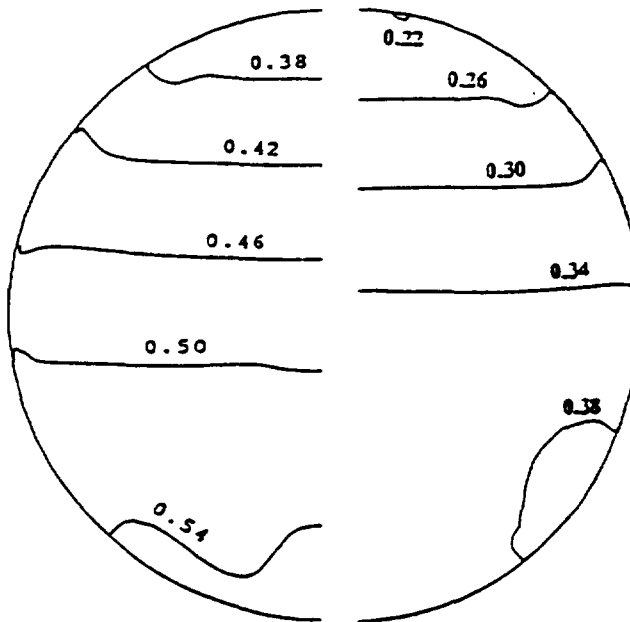
With Vortex
Generators
 $\Gamma/D_i U_\infty = 0.025$



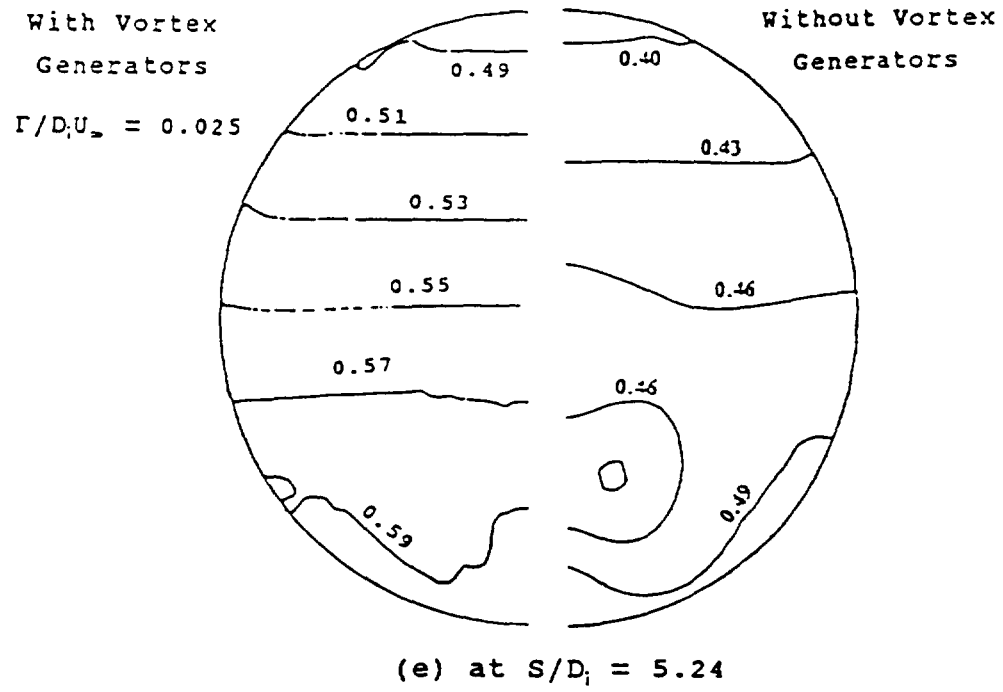
Without Vortex
Generators



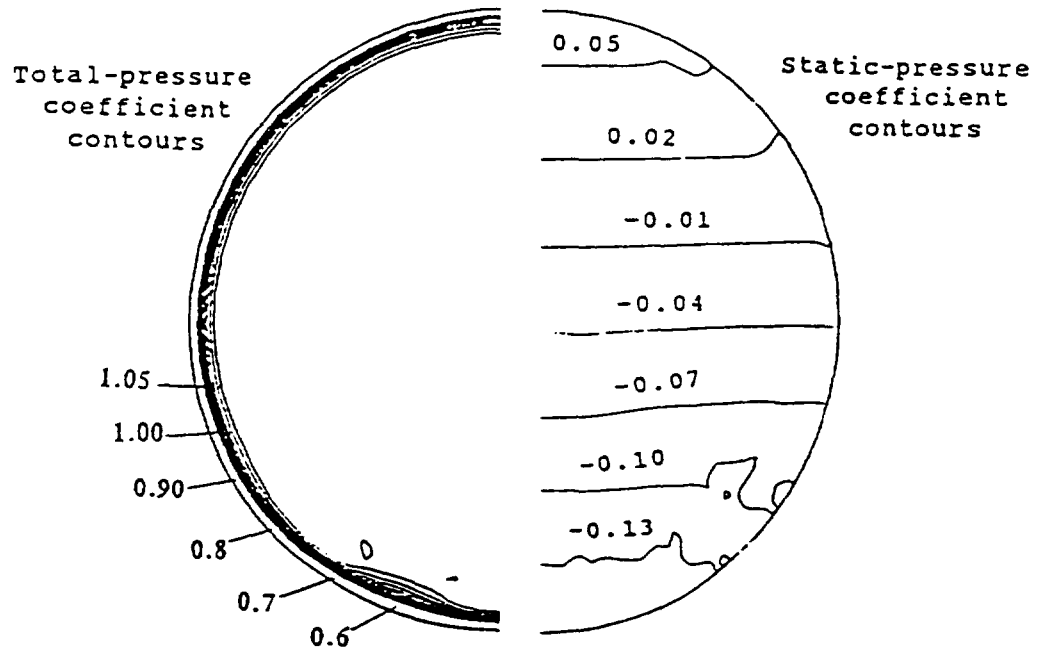
(c) at $S/D_i = 2.62$



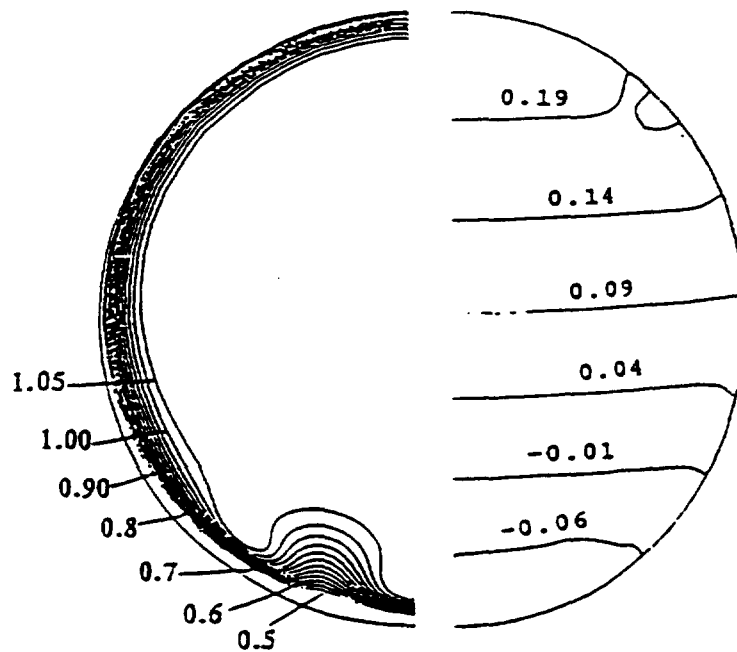
(d) at $S/D_i = 3.93$



TOTAL AND STATIC PRESSURE COEFFICIENT CONTOURS
(Vortex strength, $\Gamma/D_i U_\infty = 0.015$)



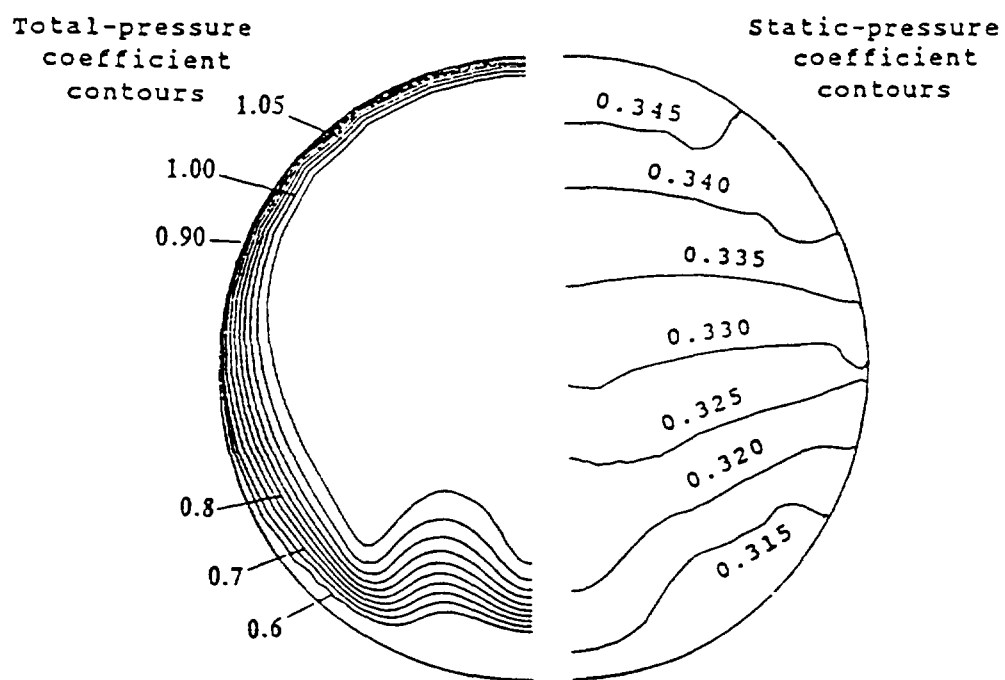
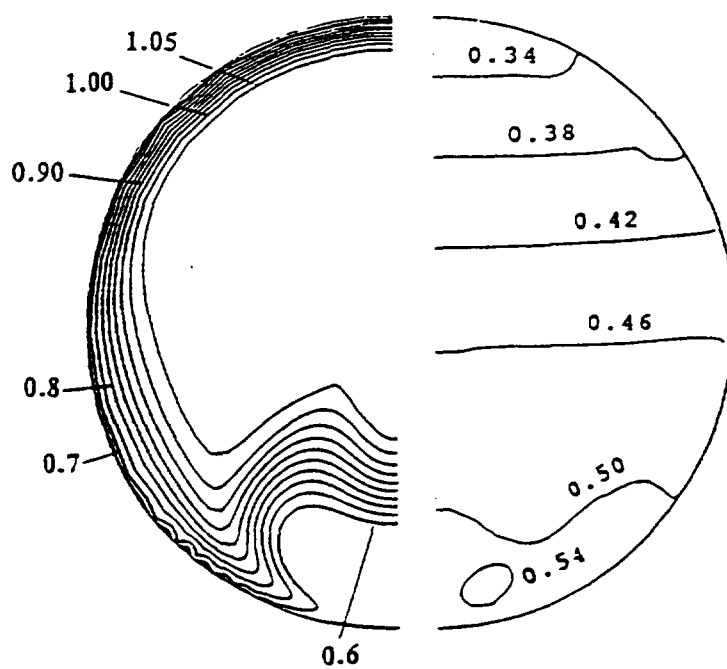
(a) at $S/D_i = 0.17$

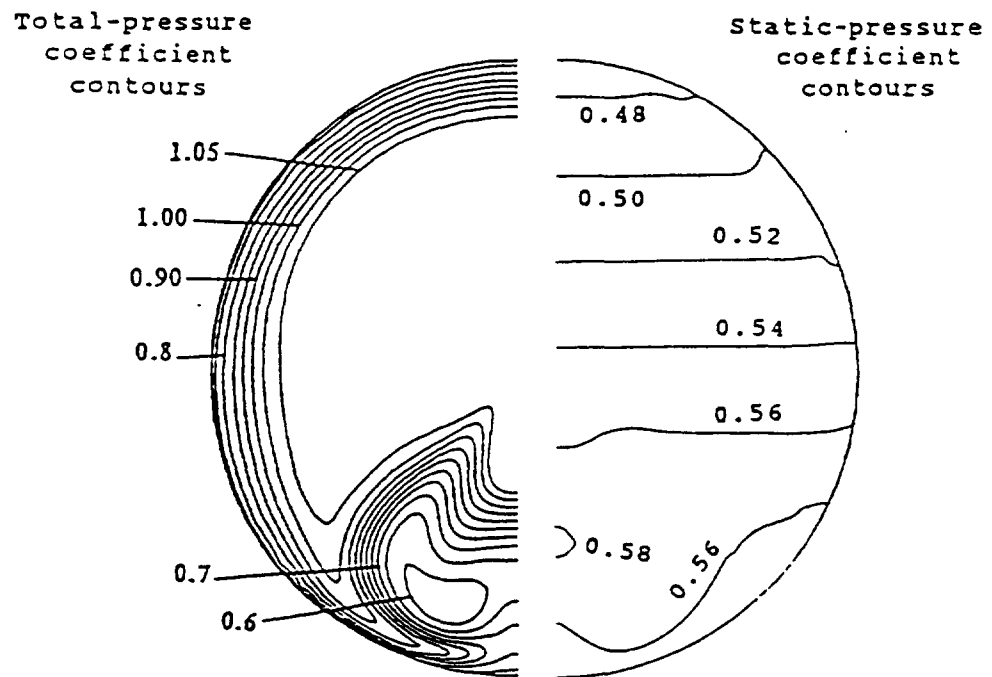


(b) at $S/D_i = 1.31$

Fig. 6.11 Total- and static-pressure coefficient contours with vortex generators.

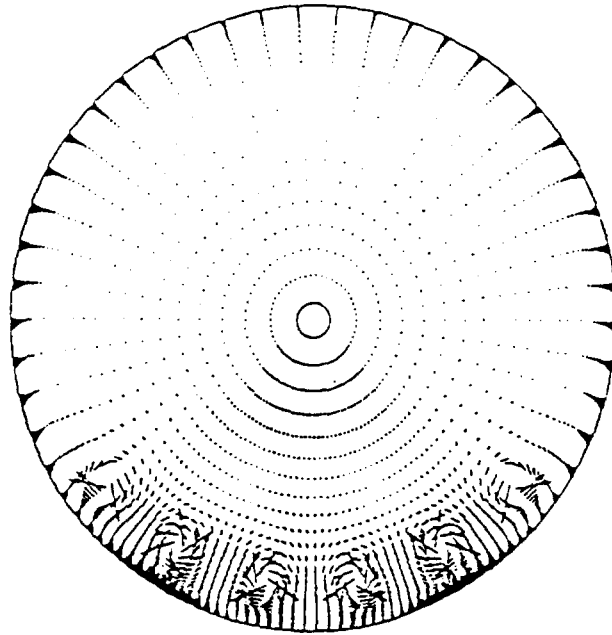
($Ma = 0.6$, $Re_d = 1.76 \times 10^6$, $\Gamma/D_i U_\infty = 0.015$)

(c) at $S/D_i = 2.62$ (d) at $S/D_i = 3.93$

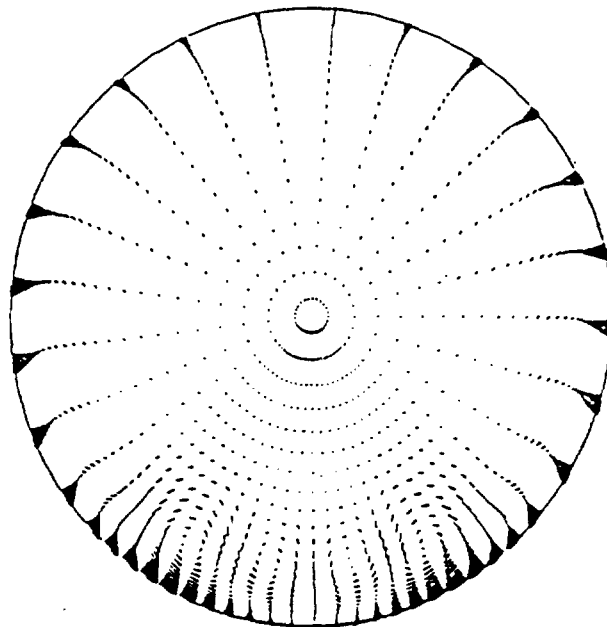


(e) at $S/D_i = 5.24$

SECONDARY VELOCITY VECTORS
 (Vortex strength, $\Gamma/D_i U_\infty = 0.015$)

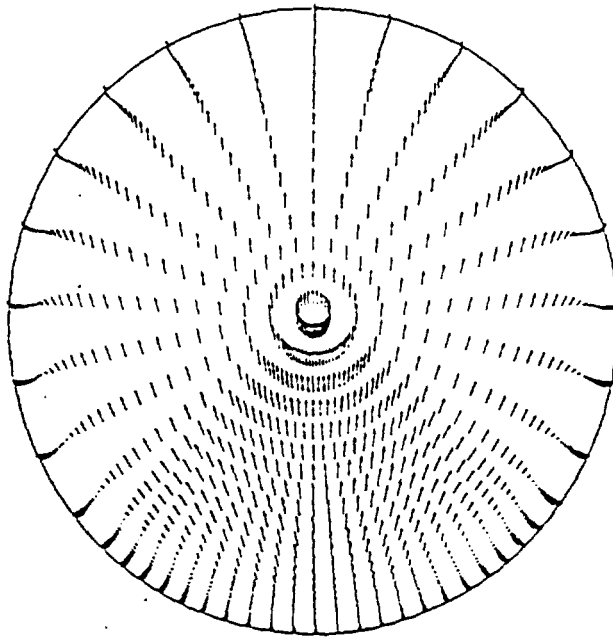


(a) at $S/D_i = 0.17$

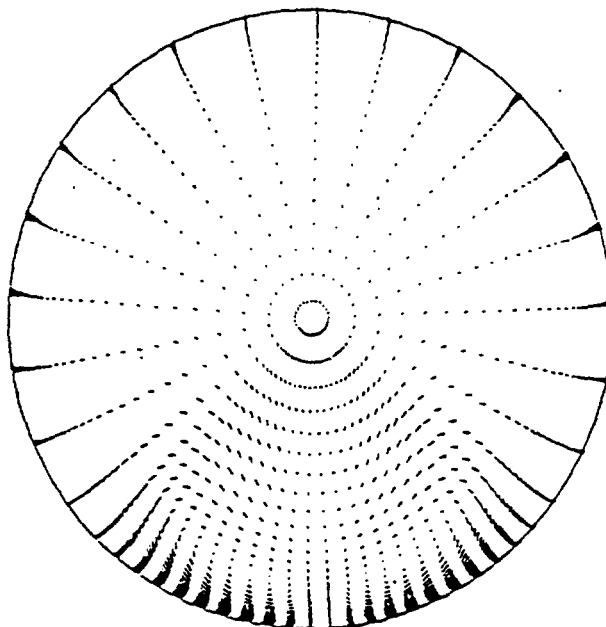


(b) at $S/D_i = 1.31$

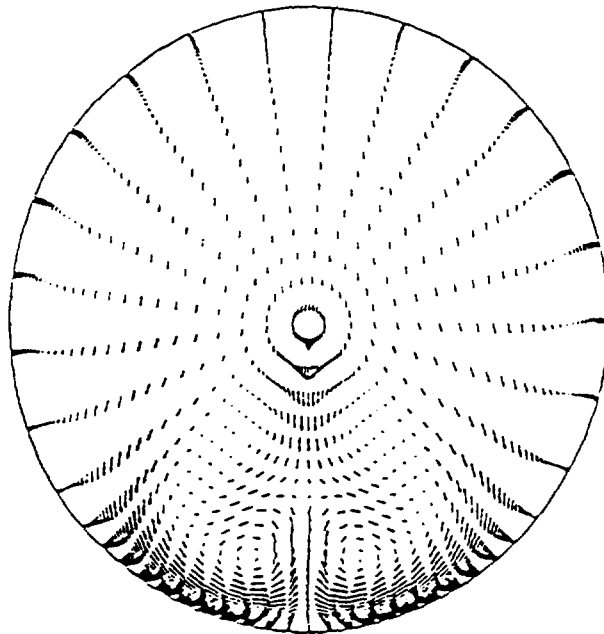
Fig. 6.12 Secondary velocity profiles with vortex generators.
 ($Ma = 0.6$, $Re_d = 1.76 \times 10^6$, $\Gamma/D_i U_\infty = 0.015$)



(c) at $S/D_i = 2.62$



(d) at $S/D_i = 3.93$



(e) at $S/D_i = 5.24$

TOTAL PRESSURE COEFFICIENT CONTOURS

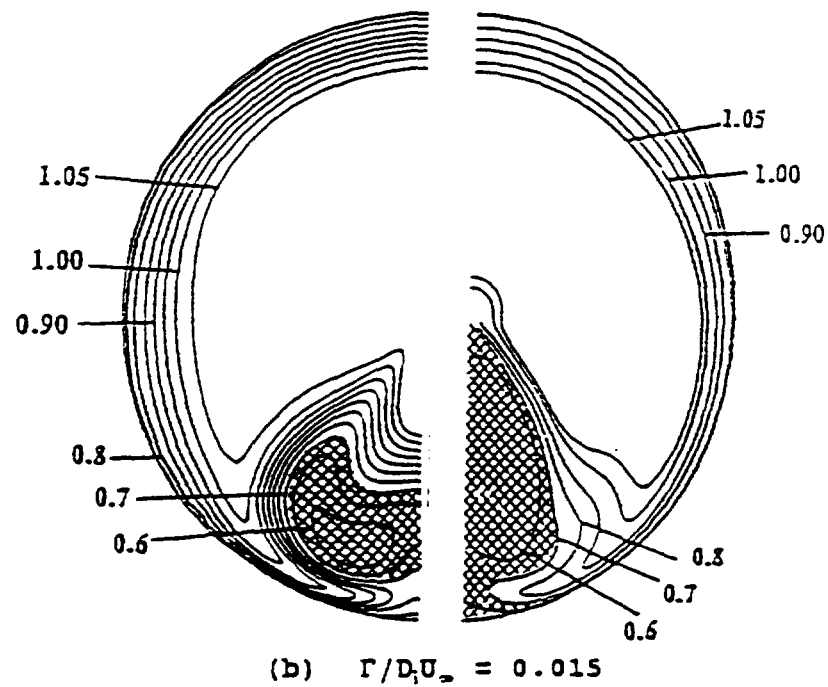
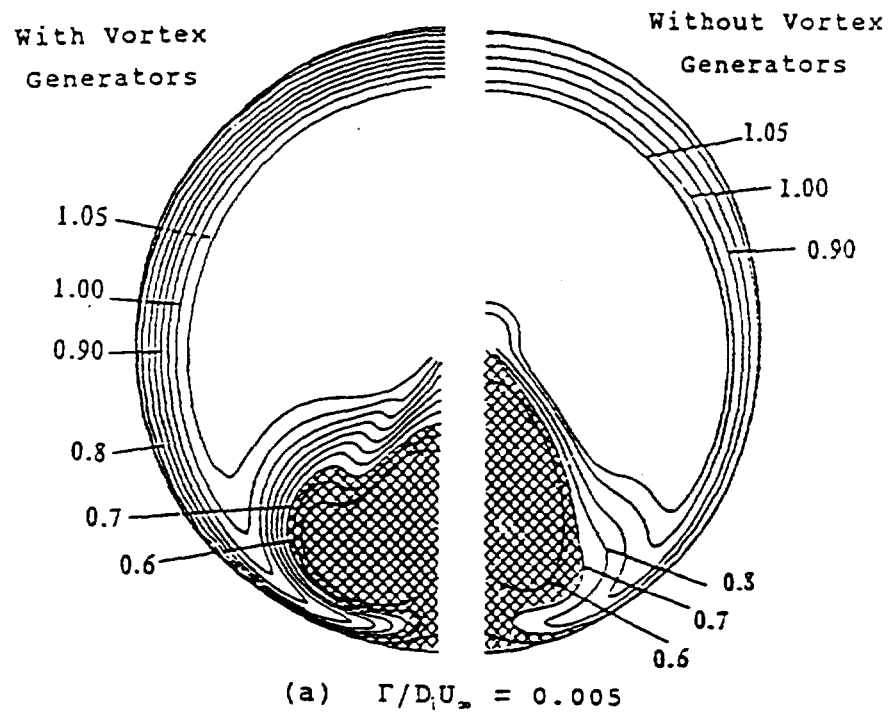
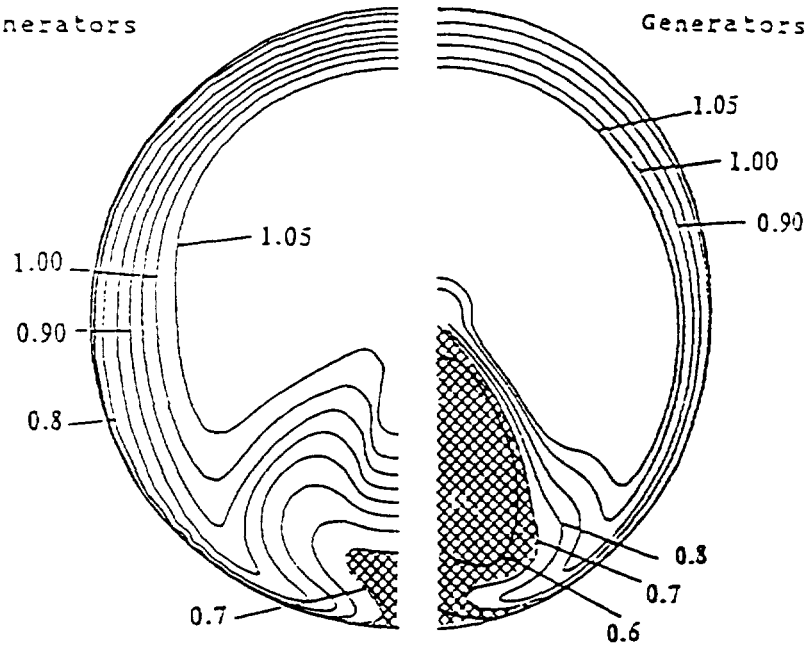


Fig. 6.13 Total-pressure coefficient contours at the exit ($S/D_1 = 5.24$) of S-duct for variation of vortex strength

With Vortex
Generators

Without Vortex
Generators



(c) $\Gamma/D_1 U_\infty = 0.025$

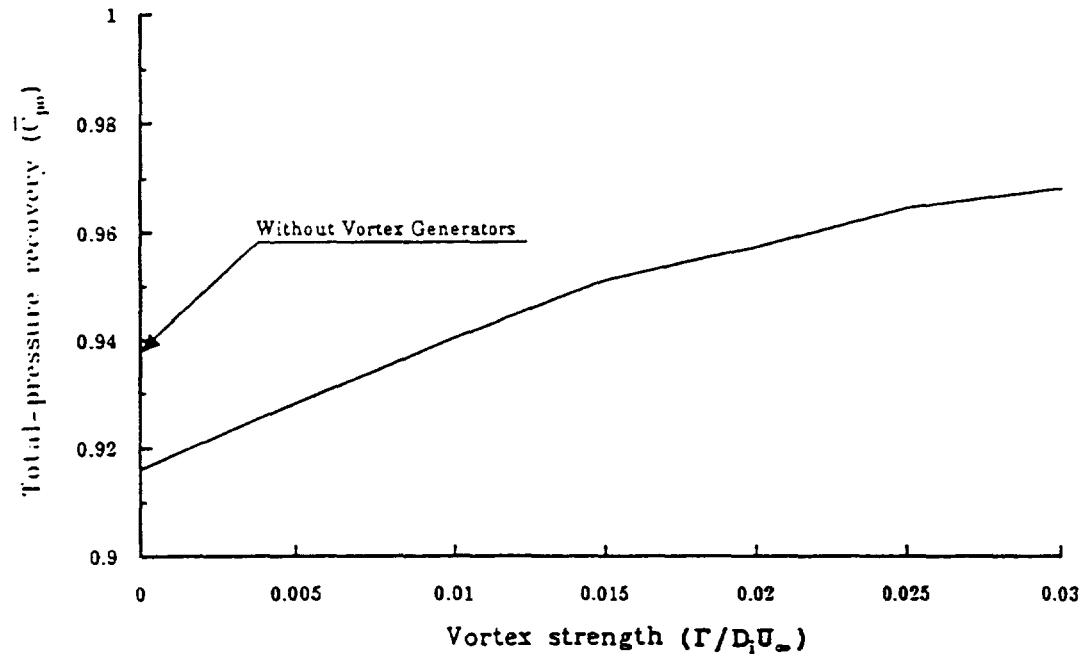


Fig. 6.14 Effect of vortex strength on the total-pressure recovery at the exit ($S/D_i = 5.24$) of S-duct.

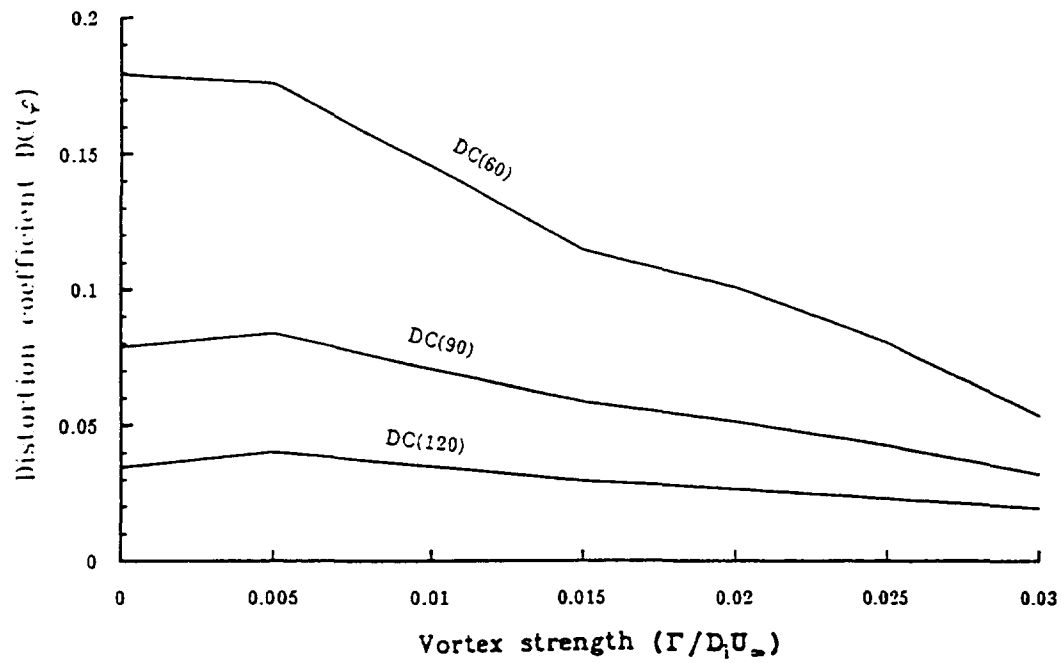


Fig. 6.15 Effect of vortex strength on the distortion coefficient at the exit ($S/D_1 = 5.24$) of S-duct.

CHAPTER 7

CONCLUSION AND RECOMMENDATION

The numerical results on a diffusing S-duct without vortex generators show the phenomena of three-dimensional flow separation. The computed results agree well with the experimental results except in the flow separation region. Downstream of flow separation, the strength of the streamwise velocity deficit ($U_{\infty} - u$) is overestimated at the region of the counter-rotating vortices resulting from the flow separation. This results from underestimating the eddy viscosity effect in the flow separation region by the turbulence model. However, the computed results are better than the previously published work obtained by Harloff et al.(1992b) with an alternative turbulence model. In order to obtain better solutions in the flow separation region, further efforts on three-dimensional turbulence modeling are necessary.

The computed results on a straight duct with vortex generators show how the injected vortices decay, move along the duct, and interact with the boundary layer in a simple geometry. For a short region (approximately three times diameter) downstream of the vortex generators, the vortex

core locations determined from the simplified model and by the full computations are in good agreement. Farther downstream, however, the simplified model is not able to predict the radially inward motion. In order to provide more accurate vortical structure for the vortex generator model, experiments with vortex generators in straight ducts would be useful.

The computed results on a diffusing S-duct with vortex generators show the interaction between the separated flow and the injected vortices. As the strength of the vortex generators increases, the extent of flow separation region is decreased. When the strength of the injected vortex is greater than $\Gamma/D_i U_\infty = 0.020$, reverse flow along the streamwise direction does not occur.

The computed results depict well the behavior of the injected vortices as they travel downstream except for the injected vortices that are introduced into the region with strong secondary velocity induced by the curvature of the duct. The behavior of the injected vortices along the streamwise direction depends on the induced secondary velocity and the injected location within the duct, even if the vortices are injected with the same strength. Experiments are needed to obtain the secondary velocity just downstream of the vortex generators in order to obtain

an accurate vortical structure for modeling the shed vortices in the curved duct.

The total-pressure recovery increases and the distortion coefficients decrease at the exit with increasing vortex strength, except for the smallest vortex strength ($\Gamma/D_0 U_\infty = 0.005$). This indicates that there exists an optimal vortex strength which will minimize the flow distortion at the exit. In order to obtain the optimum flow at the exit, additional numerical studies are necessary with various axial locations, lateral spacing, height, and number of vortex generators.

REFERENCES

- Allen, J.S and Cheng, S.I. (1970) "Numerical Solutions of the Compressible Navier-Stokes Equations for the Laminar Near Wake" *Physics Fluids* Vol.13 pp.37-52
- Anderson, B.H. (1991) "The Aerodynamic Characteristics of Vortex Ingestion for the F/A-18 inlet Duct" AIAA-91-26192
- Anderson, D.A., Tannehill, J.C. and Pletcher, R.M. (1984) "Computational Fluid Mechanics and Heat Transfer" Chap. 8 Hemisphere Publishing Copr.
- Baldwin, B.S. and Lomax, H. (1978) "Thin Layer Approximation and Algebraic Model for Separated Turbulent Flows" AIAA-78-257
- Bansod, P. and Bradshaw, P. (1972) "The Flow in S-shaped Ducts" *the Aeronautical Quarterly* Vol.23 pp.131-140
- Beam, R.M. and Warming, R.F. (1978) "An Implicit Factored Scheme for the Compressible Navier-Stokes Equations" AIAA J. Vol.16 pp.393-401
- Briley, W.R. and McDonald, H. (1973) "Solution of the Three-Dimensional Compressible Navier-Stokes Equations by an Implicit Technique" *Lecture Notes in Physics* Vol.35 pp.105-110
- Brown, A.C., Nawrocki, H.F. and Paley, P.N. (1968) "Subsonic Diffusers Designed Integrally with Vortex Generators" *J. Aircraft* Vol.5 pp.221-229
- Cebeci, T. and Smith, A.M.O. (1974) "Analysis of Turbulent Boundary Layers" Academic Press
- Degani, D. and Schiff, L.B. (1986) "Computation of Turbulent Supersonic Flows around Pointed Bodies having Crossflow Separation" *J. Computational Physics* Vol.66 pp.173-196
- Degani, D., Schiff, L.B. and Levy, Y. (1991) "Numerical Prediction of Subsonic Turbulent Flows over Slender Bodies at High Incident" AIAA J. Vol.29 pp.2054-2061

- Deiwert, G.S. (1975) "Numerical Simulation of High Reynolds Number Transonic Flows" AIAA J. Vol.13 pp.1354-1359
- Guo, R.W. and Seddon, J. (1982) "An Investigation of the Swirl in an S-Duct" the Aeronautical Quarterly Vol.33 pp.25-58
- Harloff, G.J., Bebonis, J.R., Smith, C.F. and Bruns, J.E. (1992a) "Three-Dimensional Compressible Turbulent Computations for a Nondiffusing S-Duct" NASA-CR-4391
- Harloff, G.J., Reichert, B.A. and Wellborn, S.R. (1992b) "Navier-Stokes Analysis and Experimental Data Comparison of Compressible Flow in a Diffusing S-Duct" AIAA-92-2699
- Horstman, C.C. (1987) "Prediction of Hypersonic Shock-Wave/Turbulent-Boundary-Layer Interaction Flows" AIAA-87-1367
- Jameson, A. (1983) "Transonic Flow Calculation for Aircraft" Lecture Notes in Math. 1127 *Numerical Methods in Fluid Dynamics* pp.156-242
- Jameson, A. and Turkel, E. (1981) "Implicit Schemes and LU Decompositions" Math. of Computation Vol.37 pp.385-397
- Jameson, A. and Yoon, S. (1987) "Lower-Upper Implicit Schemes with Multiple Grids for the Euler Equations" AIAA J. Vol.25 pp.929-935
- Jenkins, R.C. and Loeffler, A.L. (1992) "Modeling of Subsonic Flow Through a Compact Offset Inlet Diffuser" AIAA J. Vol.29 pp.401-408
- Kays, W.M. and Crawford, M.E. (1980) "Convective Heat and Mass Transfer" 2nd edition McGraw-Hill Inc.
- Kunik, W.G. (1986) "Application of a Computational Model for Vortex Generators in Subsonic Internal Flow" AIAA-86-1458
- Levy, R., McDonald, H., Briley, W.R. and Kreskovsky, J.P. (1980) "A Three-Dimensional Turbulent Compressible Subsonic Duct Flow Analysis for Use with Constructed Coordinated Systems" AIAA-80-1398

- Levy, R., Briley, W.R. and McDonald, H. (1983) "Viscous Primary/Secondary flow Analysis for Use with Nonorthogonal Coordinate Systems" AIAA-83-0556
- MacCormack, R.W. (1969) "The Effect of Viscosity in Hypervelocity Impact Cratering" AIAA-69-354
- MacCormack, R.W. (1971) "Numerical Solution of the Interaction of a Shock Wave with a Laminar Boundary Layer" Lecture Notes in Physics Vol.8 pp.151-163
- MacCormack, R.W. (1981) "A Numerical Method for Solving the Equations of Compressible Viscous Flow" AIAA-81-0110
- McDonald, H. and Briley, W.R. (1975) "Three-Dimensional Supersonic Flow of a Viscous or Inviscid Gas" J. Computational Physics Vol.19 pp.150-178
- McMillan, O.J. (1982) "Mean Flow Measurements of the Flow Field Diffusing Bend" NASA CR 3634
- Milne-Thomson, L.M. (1968) "Theoretical Hydrodynamics" fifth-edition Macmillan & Co Ltd.
- National Bureau of Standards Tables(1955) "Tables of Thermal Properties of Gases" U.S Dept. of Commerce National Bureau of Standards Circular
- Pauley, W.R. and Eaton, J.K. (1988) "The Fluid Dynamics and Heat Transfer Effects of Streamwise Vortices Embedded in a Turbulent Boundary Layer" Rept. MD-51, Thermosciences Div., Dept. Mech. Engr., Stanford Univ.
- Polezhaev, V.I. (1967) "Numerical Solution of the System of Two-Dimensional Unsteady Navier-Stokes Equations for a Compressible Gas in a Closed Region" Fluid Dynamics Vol.2 pp.70-74
- Pratap, V.S. and Spalding, D.B. (1975) "Numerical Computations of the Flow in Curved Ducts" the Aeronautical Quarterly Vol.26 pp.219-228
- Schubauer, G.B. and Spangenberg, W.G. (1960) "Forced Mixing in Boundary Layers" J. Fluid Mech. Vol.8 pp.10-31

- Squire, H.B. and Winter, K.G. (1951) "The Secondary Flow in a Cascade of Airfoils in a Nonuniform Stream" J. of Aeronautical Science Vol.18 No.4 pp.271-277
- Squire, H.B. (1965) "Growth of a Vortex in Turbulent Flow" the Aeronautical Quarterly Vol.16 Pt.3 pp.302-306
- Reichert, B.A. and Wendt, B.J. (1992) "An Experimental Investigation of S-Duct Flow Control Using Arrays of Low Profile Vortex Generators" to be published in 1993 AIAA paper
- Rowe, M. (1970) "Measurements and Computations of Flow in Pipe Bends" J. Fluid Mech. Vol.43 pp.771-783
- Tobak, M. and Peake, D.J. (1982) "Topology of Three-Dimensional Separation Flow" Ann. Review Fluid Mech. Vol.14 pp.61-85
- Towne, C.E. and Anderson, B.H. (1981) "Numerical Simulation of Flows in Curved Diffusers with Cross-Sectional Transitioning Using a Three-Dimensional Viscous Analysis" NASA TM 81672
- Vakili, A.D., Wu, J.M., Liver, P. and Bhat, M.K. (1983) "Measurements of Compressible Secondary Flow in a Circular S-Duct" AIAA-83-1739
- Vakili, A.D., Wu, J.M., Hingst, W.R. and Towne, C.E. (1984) "Comparison of Experimental and Computational Compressible Flow in a S-Duct" AIAA-84-0033
- Vakili, A.D., Wu, J.M., Liver, P.A. and Bhat, M.K. (1986) "Experimental Investigation of Secondary Flows in a Diffusing S-Duct with Vortex Generators" NASA NAG 3-233
- Vakili, A.D., Wu, J.M., Bhat, M.K. and Liver, P.A. (1987) "Compressible Flow in a Diffusing S-Duct with Flow Separation" in *Heat Transfer and Fluid Flow in Rotating Machinery* edited by Yang, W.J. Hemisphere publishing Corporation pp.201-211
- Warming, R.F., Beam, R.M. and Hyett, B.J. (1975) "Diagonalization and Simultaneous Symmetrization of the Gas-Dynamic Matrices" Math. of Computation Vol.29 pp.1037-1045

Wendt, B.J., Greber, I. and Hingst, W.R. (1992) "The Structure and Development of Streamwise Vortex Arrays Embedded in a Turbulent Boundary Layer" AIAA-92-0551

Wellborn, S.R., Reichert, B.A. and Okiishi, T.H. (1992) "An Experimental Investigation of the Flow in a Diffusing S-Duct" AIAA-92-3622

APPENDIX A

The Elements of Jacobian Matrices

$$\hat{A} = \frac{\partial \hat{E}}{\partial \hat{U}} = \begin{bmatrix} 0 & \frac{\partial \xi}{\partial x} & \frac{\partial \xi}{\partial y} & \frac{\partial \xi}{\partial z} & 0 \\ \hat{a}_{21} & \hat{a}_{22} & \hat{a}_{23} & \hat{a}_{24} & (\gamma-1) \frac{\partial \xi}{\partial x} \\ \hat{a}_{31} & \hat{a}_{32} & \hat{a}_{33} & \hat{a}_{34} & (\gamma-1) \frac{\partial \xi}{\partial y} \\ \hat{a}_{41} & \hat{a}_{42} & \hat{a}_{43} & \hat{a}_{44} & (\gamma-1) \frac{\partial \xi}{\partial z} \\ \hat{a}_{51} & \hat{a}_{52} & \hat{a}_{53} & \hat{a}_{54} & \hat{a}_{55} \end{bmatrix}$$

$$\hat{a}_{21} = -u \left(u \frac{\partial \xi}{\partial x} + v \frac{\partial \xi}{\partial y} + w \frac{\partial \xi}{\partial z} \right) + (\gamma-1) \bar{q} \frac{\partial \xi}{\partial x}$$

$$\hat{a}_{22} = \left(2 u \frac{\partial \xi}{\partial x} + v \frac{\partial \xi}{\partial y} + w \frac{\partial \xi}{\partial z} \right) - (\gamma-1) u \frac{\partial \xi}{\partial x}$$

$$\hat{a}_{23} = u \frac{\partial \xi}{\partial y} - (\gamma-1) v \frac{\partial \xi}{\partial x}$$

$$\hat{a}_{24} = u \frac{\partial \xi}{\partial z} - (\gamma-1) w \frac{\partial \xi}{\partial x}$$

$$\hat{a}_{31} = -v \left(u \frac{\partial \xi}{\partial x} + v \frac{\partial \xi}{\partial y} + w \frac{\partial \xi}{\partial z} \right) + (\gamma-1) \bar{q} \frac{\partial \xi}{\partial y}$$

$$\hat{a}_{32} = v \frac{\partial \xi}{\partial x} - (\gamma-1) u \frac{\partial \xi}{\partial y}$$

$$\hat{a}_{33} = \left(u \frac{\partial \xi}{\partial x} + 2 v \frac{\partial \xi}{\partial y} + w \frac{\partial \xi}{\partial z} \right) - (\gamma-1) v \frac{\partial \xi}{\partial y}$$

$$\hat{a}_{34} = v \frac{\partial \xi}{\partial z} - (\gamma - 1) w \frac{\partial \xi}{\partial y}$$

$$\hat{a}_{41} = -w \left(u \frac{\partial \xi}{\partial x} + v \frac{\partial \xi}{\partial y} + w \frac{\partial \xi}{\partial z} \right) + (\gamma - 1) \bar{q} \frac{\partial \xi}{\partial z}$$

$$\hat{a}_{42} = w \frac{\partial \xi}{\partial x} - (\gamma - 1) u \frac{\partial \xi}{\partial z}$$

$$\hat{a}_{43} = w \frac{\partial \xi}{\partial y} - (\gamma - 1) v \frac{\partial \xi}{\partial z}$$

$$\hat{a}_{44} = \left(u \frac{\partial \xi}{\partial x} + v \frac{\partial \xi}{\partial y} + 2 w \frac{\partial \xi}{\partial z} \right) - (\gamma - 1) w \frac{\partial \xi}{\partial z}$$

$$\hat{a}_{51} = - \left(u \frac{\partial \xi}{\partial x} + v \frac{\partial \xi}{\partial y} + w \frac{\partial \xi}{\partial z} \right) \left(e + \frac{p}{\rho} - (\gamma - 1) \bar{q} \right)$$

$$\hat{a}_{52} = -(\gamma - 1) u \left(u \frac{\partial \xi}{\partial x} + v \frac{\partial \xi}{\partial y} + w \frac{\partial \xi}{\partial z} \right) + \left(e + \frac{p}{\rho} \right) \frac{\partial \xi}{\partial x}$$

$$\hat{a}_{53} = -(\gamma - 1) v \left(u \frac{\partial \xi}{\partial x} + v \frac{\partial \xi}{\partial y} + w \frac{\partial \xi}{\partial z} \right) + \left(e + \frac{p}{\rho} \right) \frac{\partial \xi}{\partial y}$$

$$\hat{a}_{54} = -(\gamma - 1) w \left(u \frac{\partial \xi}{\partial x} + v \frac{\partial \xi}{\partial y} + w \frac{\partial \xi}{\partial z} \right) + \left(e + \frac{p}{\rho} \right) \frac{\partial \xi}{\partial z}$$

$$\hat{a}_{55} = \gamma \left(u \frac{\partial \xi}{\partial x} + v \frac{\partial \xi}{\partial y} + w \frac{\partial \xi}{\partial z} \right)$$

where $\bar{q} = (u^2 + v^2 + w^2)/2$

The elements of \hat{B} and \hat{C} are similar to those of \hat{A} , only ξ in the element of \hat{A} has to replace to η and ζ , respectively.

APPENDIX B

Vortex Trajectory In a Tube Using the Image Vortex System

In order to form a simple model which estimates the trajectory of a vortex in a tube, the two-dimensional problem of the motion of an infinite line vortex in a circular cylinder is considered, and then superpose an axial velocity to describe the motion of a traveling vortex in a circular cylinder.

Consider first the inviscid model. Fig. B.1 is a diagram of the vortex in a tube with an image vortex. $\lambda = r/R$ is the non-dimensional radial location of the vortex. Also note that the image flow must have a superposed circulation. This plays no role in the following discussion. The internal vortex moves with the velocity induced by the image vortex:

$$u_\theta = \frac{\Gamma}{2\pi R} \frac{\lambda}{1-\lambda^2} \quad (\text{B.1})$$

The angular velocity of the vortex motion is $u_\theta/\lambda R$. Thus:

$$\omega = \frac{\Gamma}{2\pi R^2} \frac{1}{1-\lambda^2} \quad (\text{B.2})$$

Now consider a decaying vortex. The analytic solution for a decaying vortex at the origin, with laminar flow is:

$$u_{\theta} = \frac{\Gamma}{2 \pi r} \left[1 - \exp \left(- \frac{U_{\infty} r^2}{4 \nu x} \right) \right] \quad (\text{B.3})$$

For the axially-moving vortex, the time is the particle travel time for axial motion:

$$t = \frac{x}{U_{\infty}} \quad (\text{B.4})$$

The azimuthal velocity is then given by:

$$u_{\theta} = \frac{\Gamma}{2 \pi r} \left[1 - \exp \left(- \frac{r^2}{4 \nu t} \right) \right] \quad (\text{B.5})$$

If identically decaying vortices are employed in the image system, the tube boundary is no longer a streamline. However, the image system remains valid using a simple approximation to the flow field described by Eq. (B.5). The decaying vortex has a finite velocity slope at $r = 0$, and behaves like an inviscid vortex as $r \rightarrow \infty$. It can therefore be approximated as an inviscid vortex with a solid body core. The radius of the core is the value where the solid body velocity and the vortex velocity are equal. The core radius for a vortex at the origin is:

$$r_c = 2 \sqrt{\nu t} = 2 \sqrt{\frac{\nu x}{U_{\infty}}} \quad (\text{B.6})$$

For a vortex whose center is at λR , the outer radial location of the solid body core is given by:

$$r_m = \lambda R + 2 \sqrt{\frac{\nu x}{U_\infty}} = R \left(\lambda + 2 \sqrt{\frac{x/R}{U_\infty R/\nu}} \right) \quad (\text{B.7})$$

The core reaches the wall of the tube where $r_m = R$. This occurs at an axial location given by:

$$\left(\frac{x}{R} \right)_\alpha = \frac{1}{4} \frac{U_\infty R}{\nu} (1 - \lambda_\alpha)^2 \quad (\text{B.8})$$

For $x/R \leq (x/R)_\alpha$, the azimuthal velocity and angular velocity of the vortex are given by the first factors in Eq. (B.5):

$$u_\theta = \frac{\Gamma}{2\pi R} \frac{\lambda}{(1 - \lambda^2)} \quad (\text{B.9})$$

$$\omega = \frac{\Gamma}{2\pi R^2} \frac{1}{(1 - \lambda^2)} \quad (\text{B.10})$$

To this point the model gives no information about the radial migration of the vortex. We now use the growth of the solid body core to obtain an estimate, albeit weak, of the migration of the vortex center toward the tube center. If we think of the core as a solid body, then continued growth of the core beyond $x = x_\alpha$ forces migration of the vortex toward the tube center. Then Eq. (B.8) gives the

radial location of the center of the vortex for any $x > x_\alpha$, and Eqs. (B.9) and (B.10) give the corresponding azimuthal and angular velocities. A convenient measure is the angle of travel of the vortex:

$$\theta = \int \omega \, d\tau = \frac{\Gamma}{2 \pi R^2 U_\infty} \left(\int_0^{x_\alpha} \frac{dx}{1 - \lambda_\alpha^2} + \int_{x_\alpha}^x \frac{dx}{1 - \lambda^2} \right) \quad (\text{B.11})$$

$$\theta = \frac{\Gamma}{2 \pi R^2 U_\infty} \left(\frac{x_\alpha}{1 - \lambda_\alpha^2} + \int_{x_\alpha}^x \frac{dx}{1 - \lambda^2} \right) \quad (\text{B.12})$$

In the integral in Eq. (B.12), if Eq. (B.8) holds without the subscript " α ", one then obtains:

$$1 - \lambda = \sqrt{\frac{4 x / R}{U_\infty R / v}} \equiv \sqrt{\sigma} \quad (\text{B.13})$$

Eq. (B.12) then becomes

$$\theta = \frac{\Gamma}{2 \pi R^2 U_\infty} \left(\frac{x_\alpha}{1 - \lambda_\alpha^2} + \frac{1}{4} \frac{U_\infty R^2}{v} \int_{\sigma_\alpha}^\sigma \frac{d\sigma}{\sqrt{\sigma} (2 - \sqrt{\sigma})} \right) \quad (\text{B.14})$$

Performing the integration yields:

$$\theta = \frac{\Gamma}{2 \pi R^2 U_\infty} \left[\frac{x_\alpha}{1 - \lambda_\alpha^2} + \frac{1}{2} \frac{U_\infty R^2}{v} \ln \left(\frac{1 - \frac{1}{2} \sqrt{\sigma_\alpha}}{1 - \frac{1}{2} \sqrt{\sigma}} \right) \right] \quad (\text{B.15})$$

But

$$\sqrt{\sigma_a} = 1 - \lambda_a \quad (\text{B.16})$$

and

$$x_a = \frac{1}{4} \frac{U_a R^2}{v} (1 - \lambda_a)^2 \quad (\text{B.17})$$

Therefore:

$$\theta = \frac{\Gamma}{8 \pi v} \left[\frac{1 - \lambda_a}{1 + \lambda_a} - 2 \ln \left(\frac{2 - \sqrt{\sigma}}{1 + \lambda_a} \right) \right] \quad (\text{B.18})$$

$$\lambda = 1 - \sqrt{\sigma} \quad (\text{B.13a})$$

$$\sqrt{\sigma} \equiv 2 \sqrt{\frac{x/R}{U_a R/v}} \quad (\text{B.13b})$$

Eqs. (B.18), (B.13a) and (B.13b) hold in the range:

$$(1 - \lambda_a)^2 \leq \sigma \leq 1 \quad (\text{B.19})$$

For $\sigma < (1 - \lambda_a)^2$, $\lambda = \lambda_a$ and the azimuthal angular travel is given by:

$$\theta = \frac{\Gamma x}{2 \pi R^2 U_a (1 - \lambda^2)} \quad (\text{B.20})$$

An alternative measure of the azimuthal travel is the tangent of the helix angle. This is obtained by merely re-writing Eqs. (B.18) and (B.20):

$$\frac{\theta R}{x} = \frac{\Gamma}{2 \pi R U_{\infty}} \frac{1}{\sigma} \left[\frac{1 - \lambda_a}{1 + \lambda_a} - 2 \ln \left(\frac{2 - \sqrt{\sigma}}{1 + \lambda_a} \right) \right] \quad (\text{B.21})$$

$$\frac{\theta R}{x} = \frac{\Gamma}{2 \pi R U_{\infty} (1 - \lambda^2)} \quad (\text{B.22})$$

where Eqs. (B.21) and (B.22) are valid in the large σ and small σ ranges, respectively.

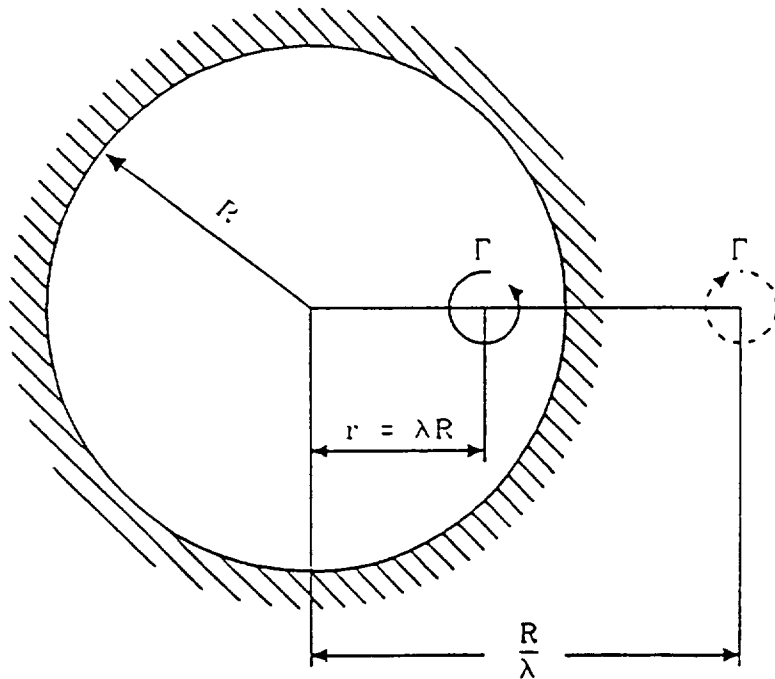


Fig. B.1 When a single vortex of strength Γ is located inside the circular cylinder, image vortex is located on the line connecting the center of a circular cylinder and a single vortex.

APPENDIX C

Vortex Trajectory In a Tube Using the Vortex Interaction Model

Circulation decay of vortex in the turbulent flow is faster than in the laminar flow because of a large eddy viscosity. Circulation decay on the previous model is very slow because only kinematic viscosity is used. In this model, the wall effects and proximity effects are considered to predict circulation decay of the vortex in the tube. At first, circulation decay by the wall effects is considered. Fig. C.1 is a diagram when a vortex is embedded at some crossplane location x . The secondary flows produced by the injected vortex give rise to a corresponding circumferential component of the wall shear stress ($\tau_{r\theta}$). In turn, this stress results in a torque opposing the rotation of the vortex. The moment M_i opposing the rotation of vortex i can be obtained by integrating the magnitude of the elemental torque:

$$M_i = \frac{dH_i}{dt} = \int_0^{2\pi} \langle \tau_{r\theta} | \vec{r} | d\theta dx, \vec{r} \rangle \quad (C.1)$$

where $|\vec{r}|$ is the distance from the center of vortex to the

wall, and H_i is the angular momentum of vortex i of elemental thickness dx .

Assuming proportionality between the vortex angular momentum and its circulation, we obtain the streamwise circulation gradient:

$$\frac{d\Gamma}{dx} = \frac{1}{C_{wf} \rho U_\infty} \int_0^{2\pi} \langle \tau_{r\theta} | \bar{r} | d\theta, \bar{r} \rangle \quad (C.2)$$

where C_{wf} is the unknown constant of proportionality with units of m^2 .

$\tau_{r\theta}$ is a function of wall coordinates, i.e., $\tau_{r\theta} = \tau_{r\theta}(r, \theta)$ and it is proportional to the circumferential component of the secondary velocity at the wall. To simplify this expression, the correlation suggested by Pauley and Eaton(1988) is adopted.

$$\tau_{r\theta} = C_r \tau_{2D} u_\theta(\theta, r = |\bar{r}|) \quad (C.3)$$

where $u_\theta(\theta, r = |\bar{r}|)$ is the circumferential velocity with image vortex at the wall. $\tau_{r\theta}$ is the wall shear stress of the corresponding two dimensional boundary layers and C_r is a scaling factor with units of sec/m ;

$$\tau_{2D} = \frac{\rho_\infty U_\infty^2}{2} C_f = \frac{\rho_\infty U_\infty^2}{2} (0.3164 Re_d^{-\frac{1}{4}}) \quad (C.4)$$

Re_d is a Reynolds number based on the duct diameter.

Substitute Eqs. (C.3) and (C.4) into (C.2), and then we obtain the circulation gradient along the streamwise direction by the wall effects;

$$\frac{d\Gamma}{dx} \Big|_{wf} = \frac{C_{\tau} U_{\infty}}{C_{wf}} (0.1582 Re_d^{-\frac{1}{4}}) \int_0^{2\pi} |\vec{r}|^2 \cos(\beta) d\theta \quad (C.5)$$

where β is an intersectional angle between the r -direction and the θ -direction.

When the multiple vortices are embedded in a crossplane, the vortices interact both because of their induced field and through diffusion. Fig. C.2 is a diagram of two counter-rotating vortex cores in close proximity. The circulation decay by proximity effect can be expressed:

$$\frac{d\Gamma}{dx} \Big|_{prox} = C_{prox} \frac{\Gamma}{|\Gamma|} \Big| \frac{d\omega}{dR} \Big|_{x=x_0} \quad (C.6)$$

where C_{prox} is the unknown constant of proportionality with units of m^2 , and the sign of C_{prox} depends on the rotation direction of the neighboring vortex.

Total circulation decay is written:

$$\frac{d\Gamma}{dx} = \frac{d\Gamma}{dx} \Big|_{wf} + \frac{d\Gamma}{dx} \Big|_{prox} \quad (C.7)$$

With this gradient and an assumption that the embedded vortices move axially at the free streamwise velocity, we

can track the streamwise displacement of the embedded vortex step by step

$$r(x + \Delta x) = r(x) + \Delta x \left(\frac{\partial r(x)}{\partial x} \right) \quad (\text{C.8})$$

$$\theta(x + \Delta x) = \theta(x) + \Delta x \left(\frac{\partial \theta(x)}{\partial x} \right) \quad (\text{C.9})$$

$$\Gamma(x + \Delta x) = \Gamma(x) + \Delta x \left(\frac{\partial \Gamma(x)}{\partial x} \right) \quad (\text{C.10})$$

As noted early, the same constants C_{wf} ($1.40 \times 10^{-6} \text{ m}^2$), C_{prax} ($1.40 \times 10^{-4} \text{ m}^2$) and C_r (0.046 sec/m), which were derived from the experimental result on the flat plate, are adopted to predict the circulation decay in the internal flow.

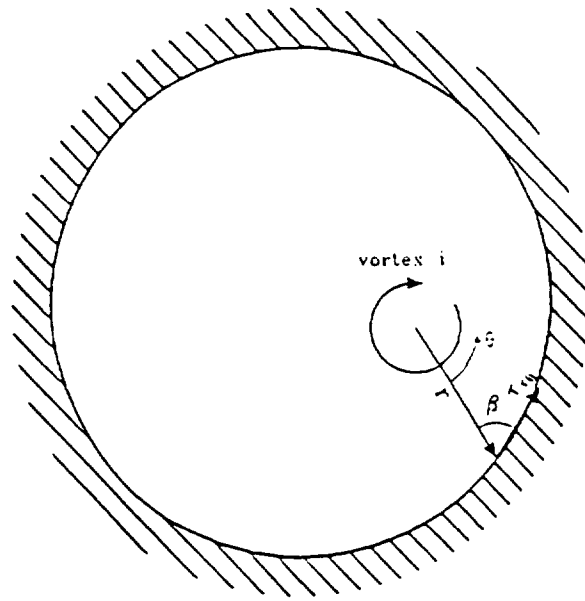


Fig. C.1 The secondary flow field generated by vortex i gives rise to a local circumferential component of wall shear stress τ_w , which opposes the rotation of vortex i.

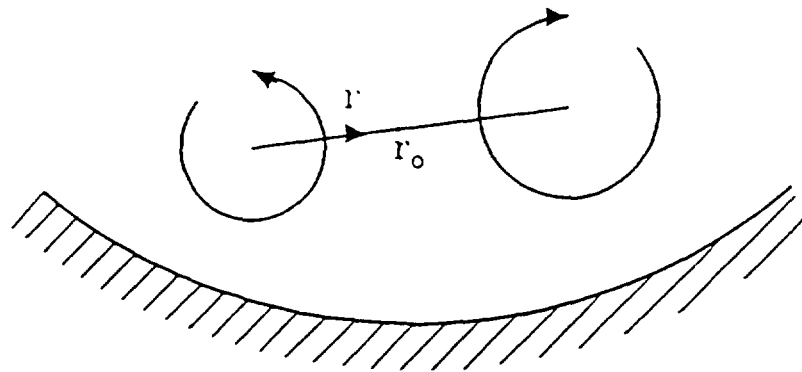


Fig. C.2 Two neighbor vortices in a circular duct for evaluating proximity circulation losses. The r represents the coordinate axis along the line connecting adjacent cores, and r_0 is the location on r where the vorticity changes sign in the model.

REPORT DOCUMENTATION PAGE			Form Approved OMB No. 0704-0188	
Public reporting burden for this collection of information is estimated to average 1 hour per response, including the time for reviewing instructions, searching existing data sources, gathering and maintaining the data needed, and completing and reviewing the collection of information. Send comments regarding this burden estimate or any other aspect of this collection of information, including suggestions for reducing this burden, to Washington Headquarters Services, Directorate for Information Operations and Reports, 1215 Jefferson Davis Highway, Suite 1204, Arlington, VA 22202-4302, and to the Office of Management and Budget, Paperwork Reduction Project (0704-0188), Washington, DC 20503.				
1. AGENCY USE ONLY (Leave blank)	2. REPORT DATE December 1994	3. REPORT TYPE AND DATES COVERED Final Contractor Report		
4. TITLE AND SUBTITLE Three Dimensional Compressible Turbulent Flow Computations for a Diffusing S-Duct With/Without Vortex Generators		5. FUNDING NUMBERS WU-505-62-52 NCC3-181		
6. AUTHOR(S) Soo-Yong Cho and Isaac Greber				
7. PERFORMING ORGANIZATION NAME(S) AND ADDRESS(ES) Case Western Reserve University Department of Mechanical and Aerospace Engineering Cleveland, Ohio 44106		8. PERFORMING ORGANIZATION REPORT NUMBER E-9160		
9. SPONSORING/MONITORING AGENCY NAME(S) AND ADDRESS(ES) National Aeronautics and Space Administration Lewis Research Center Cleveland, Ohio 44135-3191		10. SPONSORING/MONITORING AGENCY REPORT NUMBER NASA CR-195390		
11. SUPPLEMENTARY NOTES Project Manager, Bernhard H. Anderson, Internal Fluid Mechanics Division, NASA Lewis Research Center, organization code 2600, (216) 433-5822.				
12a. DISTRIBUTION/AVAILABILITY STATEMENT Unclassified - Unlimited Subject Category 07		12b. DISTRIBUTION CODE		
13. ABSTRACT (Maximum 200 words) Numerical investigations on a diffusing S-duct with/without vortex generators and a straight duct with vortex generators are presented. The investigation consists of solving the full three-dimensional unsteady compressible mass averaged Navier-Stokes equations. An implicit finite volume lower-upper time marching code (RPLUS3D) has been employed and modified. A three-dimensional Baldwin-Lomax turbulence model has been modified in conjunction with the flow physics. A model for the analysis of vortex generators in a fully viscous subsonic internal flow is evaluated. A vortical structure for modelling the shed vortex is used as a source term in the computation domain. The injected vortex paths in the straight duct are compared with the analysis by two kinds of prediction models. The flow structure by the vortex generators are investigated along the duct. Computed results of the flow in a circular diffusing S-duct provide an understanding of the flow structure within a typical engine inlet system. These are compared with the experimental wall static-pressure, static- and total-pressure field, and secondary velocity profiles. Additionally, boundary layer thickness, skin friction values, and velocity profiles in wall coordinates are presented. In order to investigate the effect of vortex generators, various vortex strengths are examined in this study. The total-pressure recovery and distortion coefficients are obtained at the exit of the S-duct. The numerical results clearly depict the interaction between the low velocity flow by the flow separation and the injected vortices.				
14. SUBJECT TERMS Computational fluid dynamics; Internal flow; Inlets; Nozzles; Diffusers		15. NUMBER OF PAGES 216		
		16. PRICE CODE A10		
17. SECURITY CLASSIFICATION OF REPORT Unclassified	18. SECURITY CLASSIFICATION OF THIS PAGE Unclassified	19. SECURITY CLASSIFICATION OF ABSTRACT Unclassified	20. LIMITATION OF ABSTRACT	